AUTARQUIA ASSOCIADA À UNIVERSIDADE DE SÃO PAULO

Synthesis of fluorine-18-labeled losartan analogs as novel positron emission tomography tracers for cancer imaging

MARTHA SAHYLÍ ORTEGA PIJEIRA

Tese apresentada como parte dos requisitos para obtenção do Grau de Doutor em Ciências na Área de Tecnologia Nuclear - Aplicações

Orientador:
Prof. Dr. Emerson Soares Bernardes

São Paulo
2019

INSTITUTO DE PESQUISAS ENERGÉTICAS E NUCLEARES
Autarquia associada à Universidade de São Paulo

Synthesis of fluorine-18-labeled losartan analogs as novel positron emission tomography tracers for cancer imaging

MARTHA SAHYLÍ ORTEGA PIJEIRA

Tese apresentada como parte dos requisitos para obtenção do Grau de Doutor em Ciências na Área de Tecnologia Nuclear - Aplicações

Orientador:
Prof. Dr. Emerson Soares Bernardes

Versão Corrigida
Versão Original disponível no IPEN

São Paulo
2019

Fonte de Financiamento: Coordenação de Aperfeiçoamento de Pessoal de Nível Superior - Brasil (CAPES) - Código de Financiamento 001

Como citar:

ORTEGA PIJEIRA, M. S. ***Synthesis of fluorine-18-labeled losartan analogs as novel positron emission tomography tracers for cancer imaging***. 2019. 144 p. Tese (Doutorado em Tecnologia Nuclear), Instituto de Pesquisas Energéticas e Nucleares, IPEN-CNEN/SP, São Paulo. Disponível em: <www.teses.usp.br> (data de consulta no formato: dd/mm/aaaa)

Ficha catalográfica elaborada pelo Sistema de geração automática da Biblioteca IPEN/USP, com os dados fornecidos pelo(a) autor(a)

Ortega Pijeira, Martha Sahylí
Synthesis of fluorine-18-labeled losartan analogs as novel positron emission tomography tracers for cancer imaging / Martha Sahylí Ortega Pijeira; orientador Emerson Soares Bernardes. -- São Paulo, 2019.
144 p.

Tese (Doutorado) - Programa de Pós-Graduação em Tecnologia Nuclear (Aplicações) -- Instituto de Pesquisas Energéticas e Nucleares, São Paulo, 2019.

1. [19/18F]fluoroethyl-losartan. 2. [19/18F]ammoniomethyltrifluoroborate-losartan. 3. synthesis. 4. biological evaluation. 5. PET imaging of AT1R-positive tumors. I. Soares Bernardes, Emerson , orient. II. Título.

APPROVAL SHEET

Author: Martha Sahylí Ortega Pijeira

Title: Synthesis of fluorine-18-labeled losartan analogs as novel positron emission tomography tracers for cancer imaging

Thesis presented to the Postgraduate Program in Nuclear Technology of the University of São Paulo for obtaining the title of Doctor of Sciences

Date:

Examining Committee

Prof. Dr. _____

Institution: _____ Judgement:_____

Prof. Dr. _____

Institution: _____ Judgement:_____

Prof. Dr. _____

Institution: _____ Judgement:_____

Prof. Dr. _____

Institution: _____ Judgement:_____

Prof. Dr. _____

Institution: _____ Judgement:_____

To my dear mom Marta Pijeira

and grandparents

Narcisa Sánchez and Rafael Pijeira

ACKNOWLEDGMENTS

A sincere “thank you” to my mentor Dr. Emerson Soares Bernardes, for allowing me to join this interesting and challenging project. For his great help, valuable support and contribution in order to improve my formation as a radiochemist. For its excellent supervision, and patience during these challenging four years of PhD program.

I am also thankful to my colleague Dr. Sofia Nascimento dos Santos for her help in several experiments and her valuable contribution to the analysis and discussion of results.

A great thank you to my colleagues BSc. Arian Perez Nario, Dra. Angélica Barbezan, BSc. Yasniel Babí Araujo and MSc. Fábio Fernando Alves da Silva for their help in several experiments at IPEN, SP, Brazil.

Thank you so much, Dr. Paulo Sérgio Gonçalves Nunes for your great help with the cold organic synthesis and all spectroscopic data analysis.

I am also greatful to Dra. Ivone Carvalho from the School of Pharmaceutical Sciences of Ribeirão Preto, University of São Paulo, Brazil for allowing me to perform the cold organic synthesis in her lab, to support and supervise the results and to kindly discuss the data with me every time I needed. I would like also to thank the lab staff, especially Luís Otávio Zamoner.

Thanks to the Coordination for the Improvement of Higher Education Personnel (CAPES) - Finance Code 001, to finance my scholarship in Brazil.

Thanks to the São Paulo Research Foundation (FAPESP) and the Radiopharmacy Center of the Nuclear and Energy Research Institute (IPEN/CNEN), in Brazil, for their valuable financial support in this research.

Thanks to the Radiopharmacy Center staff, especially to Wagner Nieto, Rosana Herrerias, Wilson Bruzinga, Edivaldo Caetano Da Silva, MSc. Jair Mengatti, MSc. Efrain Perini, Dr. Luis Alberto Pereira Dias, Dr. Lorena Pozzo and Dr. Regina Carneiro. Also to the quality control department (MSc. Natanael Gomes Da Silva and Carlos Farias Felgueiras), the radiological protection department, and administrative assistants.

Thanks to the Cyclotron Accelerators Center staff at IPEN, especially to Décio Borges de Souza, Enocles Melo de Oliveira, Dr. André Luis Lapolli, and Dr. Henrique Barcellos De Oliveira.

Thanks to the Animal Resource Centre staff at IPEN.

Thanks, Dr. Walter Miguel Turato from the School of Pharmaceutical Sciences of the University of São Paulo, Brazil, for helping with the PET imaging studies.

Many thanks to Dr. Philip Elsinga from the Department of Nuclear Medicine and Molecular Imaging, University of Groningen, Netherlands, for your valuable contribution to this PhD project and for sharing your expertise.

Many thanks to Dr. Carlos Buchpiguel and Dr. Roger Chammas from the Department of Radiology and Oncology of the Faculty of Medicine, University of São Paulo, Brazil, for your valuable contributions to this PhD project.

I am grateful to Dr. Ulises Jáuregui and Dr. Zalua Rodríguez from the Higher Institute of Technologies and Applied Sciences (InSTEC) in Cuba.

Many thanks, Dr. Kuo-Shyan Lin and Dr. François Bénard from the Department of Molecular Oncology at BC Cancer Agency, Vancouver, British Columbia, Canada, along with the Canadian Government (ELAP - Emerging Leaders in the Americas Program 2016-2017), for supporting my five-month research stay at your lab and for sharing your expertise.

Many thanks, to Dr. Lin and Bénard´s lab for your great help: Dr. Zhengxing Zhang, Dra. Julie Rousseau, Dr. Chengcheng Zhang, Dra. Hsiou-Ting Kuo, Dra. Gemma Dias, MSc. Iulia Dude, Dr. Joseph Lau, Jutta Zeisler, Dra. Milena Čolović, Helen Merkens, Nadine Colpo, Dr. Carlos Uribe, Dr. Freidrich Kreuz-Fisch, Dr. Etienne Rousseau, MSc. Marin Simunic, and Dr. Jinhe Pan.

Thanks to the BC Cancer Research Centre staff in Vancouver, Canada.

A special “thank you” to my family, in particular to my mother Marta Pijeira, for her valuable support, optimism, and confidence in me; and thank you to my stepfather Rubén Quesada and aunt Baby Quesada.

Thank you very much to all friends from all over the world for their support, especially Arian Pérez Nario, Ivón Oramas Polo, María Adelfa Abreu Zamora, Javier Mantecón, Juan Alejandro García Alvarez and Ernesto Martínez Baez.

Thanks to all examiners for their critical opinions and suggestions, which improved my research and made me a better researcher.

Thanks to all who helped me in different ways, and I did not mention above.

Finally, my most special acknowledgment to God for being my spiritual support and guide and, for sure, allowing me to meet all of you who helped me a lot.

MANY THANKS

"One never notices what has been done; one can only see what remains to be done."

– Marie Curie

ABSTRACT

ORTEGA PIJEIRA, M. S. ***Synthesis of fluorine-18-labeled losartan analogs as novel positron emission tomography tracers for cancer imaging***. 2019. 144 p. Tese (Doutorado em Tecnologia Nuclear) – Instituto de Pesquisas Energéticas e Nucleares – IPEN-CNEN/SP. São Paulo.

Losartan is a selective antagonist of the angiotensin II type 1 receptor (AT_1R). Several reports have highlighted the AT_1R expression in several cancers enhancing tumor development and cancer progression. The aim of this thesis is the synthesis and evaluation of [^{18}F]fluoroethyl-losartan ([^{18}F]FEtLos) and [^{18}F]ammoniomethyltrifluoroborate-losartan ([^{18}F]AMBF$_3$Los) as two novel losartan analogs to image AT_1R-positive tumors using the positron emission tomography (PET). Initially, the cold compounds FEtLos and AMBF$_3$Los were synthetized by alkylation and click chemistry reactions respectively, and characterized by spectroscopic techniques. Then, radiosynthesis of 2-[^{18}F]fluoroethyl-tosylate was optimized from a radiation safety point of view. Next, [^{18}F]FEtLos was manually synthetized by [^{18}F]fluoroethylation of losartan with low molar activity and greater than 99% radiochemical purity. [^{18}F]AMBF$_3$Los was easily synthetized with greater than 97% radiochemical purity by one step ^{18}F-^{19}F isotopic exchange approach using low and high activities of [^{18}F]fluoride that afforded molar activities ranging from 2 to 139 GBq/μmol. *In vitro* competition binding assays showed that FEtLos and AMBF$_3$Los have low and high binding affinity to human AT_1R, respectively. AT_1R expression was confirmed in breast, ovarian and gastric derived-tumors implanted on Nude mice. In spite of the low affinity, [^{18}F]FEtLos was specific for renal AT_1R. However, [^{18}F]FEtLos did not showed specificity for tumor AT_1R binding. μPET imaging, autoradiography and *ex vivo* biodistribution studies showed the specificity of [^{18}F]AMBF$_3$Los for both kidney and tumor AT_1R binding. However, [^{18}F]AMBF$_3$Los was not able to reach the tumor site once injected intravenously probably because of its rapid metabolism and very fast clearance. Nonetheless our results demonstrate that ^{18}F-Angiotensin II Receptor Blockers (ARBs) derivatives could be suitable tracers to cancer imaging AT_1R-expressing tumor microenvironment, however, radiolabeled ARBs that possess better pharmacokinetics profile may be required.

Key words: [$^{19/18}$F]fluoroethyl-losartan; [$^{19/18}$F]ammoniomethyltrifluoroborate-losartan; synthesis; biological evaluation; PET imaging of AT_1R-positive tumors.

RESUMO

ORTEGA PIJEIRA, M. S. ***Síntese de análogos do losartan marcados com Flúor-18 como novos traçadores para imagem do câncer utilizando Tomografia por Emissão de Pósitrons***. 2019. 144 p. Tese (Doutorado em Tecnologia Nuclear) – Instituto de Pesquisas Energéticas e Nucleares – IPEN-CNEN/SP. São Paulo.

O losartan é um antagonista seletivo do receptor tipo 1 de angiotensina II (AT_1R). Vários reportes têm destacado a expressão do AT_1R em vários cânceres favorecendo o desenvolvimento tumoral e progressão do câncer. O objetivo desta tese é a síntese e avaliação do [^{18}F]fluoroetil-losartan ([^{18}F]FEtLos) e [^{18}F]amoniometiltrifluoroborato-losartan ([^{18}F]AMBF_3Los) como dois novos análogos do losartan para imagem de tumores AT_1R-positivos usando a tomografia por emissão de pósitrons (PET). Inicialmente, os compostos padrões FEtLos e AMBF_3Los foram sintetizados por reações de alquilação e química *click* respetivamente, e caraterizados por técnicas espectroscópicas. A seguir, a radiosíntese do 2-[^{18}F]fluoroetil-tosilato foi otimizada do ponto de vista de seguridade radiológica. O [^{18}F]FEtLos foi depois sintetizado por alquilação do losartan utilizando o grupo prostético 2-[^{18}F]fluoroetil-tosilato, com baixa atividade molar, e pureza radioquímica maior do 99%. [^{18}F]AMBF_3Los foi facilmente sintetizado com pureza radioquímica maior do 97% por troca isotópica ^{18}F-^{19}F usando baixas e altas atividades de [^{18}F]fluoreto o que providenciou atividades molares entre 2 e 139 GBq/μmol. Ensaios de ligação por competição *in vitro* mostraram que FEtLos e AMBF_3Los têm baixa e alta afinidade de ligação ao AT_1R humano respetivamente. A expressão do AT_1R foi confirmada em tumores de mama, ovário e gástrico, implantados em camundongos Nude. A pesar da baixa afinidade, o [^{18}F]FEtLos foi específico pelo AT_1R renal. Não entanto, [^{18}F]FEtLos não mostrou especificidade pela ligação ao AT_1R no tumor. A imagem μPET, autoradiografia, e os estudos de biodistribuição *ex vivo* mostraram a especificidade do [^{18}F]AMBF_3Los pela ligação ao AT_1R nos rins e no tumor. O radiotraçador [^{18}F]AMBF_3Los não foi capaz de ligar no tumor quando injetado intravenosamente, provavelmente devido ao seu rápido metabolismo e rápida depuração sanguínea. Apesar disso, nossos dados demonstram que os derivados de Bloqueadores do Receptor de Angiotensina II (ARBs) radiomarcados com ^{18}F podem ser potenciais radiofármacos para o imageamento do microambiente

tumoral positivo para AT_1R, no entanto o perfil farmacocinético dos ARBs radiomarcados ainda precisa ser melhorado.

Palavras-chave: [$^{19/18}$F]fluoroetil-losartan; [$^{19/18}$F]amoniometiltrifluoroborato-losartan; síntese; avaliação biológica; imagem PET de tumores AT_1R-positivos

LIST OF ABBREVIATIONS

%ID/µL	percentage of Injected Dose per volume of blood
%ID/g	percentage of Injected Dose per Gram of tissue
[^{18}F]AMBF$_3$Los	[^{18}F]ammoniomethyltrifluoroborate-losartan
[^{18}F]FAZA	[^{18}F]fluoroazomycin arabinoside
[^{18}F]FDG	2-[^{18}F]fluoro-2-deoxyglucose
[^{18}F]FEtLos	[^{18}F]fluoroethyl-losartan
[^{18}F]FEtOTs	2-[^{18}F]fluoroethyl-tosylate
[^{18}F]FPyKYNE	2- [^{18}F]fluoro-3-pent-4-yn-1-yloxypyridine
[^{18}F]FSP5	^{18}F-labeled Side-Product at ~5 min
[^{18}F]FV45	[^{18}F]F-Valsartan
ACE	Angiotensin Converting Enzyme
ACE2	Angiotensin Converting Enzyme two
AMBF$_3$	ammoniomethyltrifluoroborate
ANG 1-7	Angiotensin 1-7
ANG I	Angiotensin I
ANG II	Angiotensin II
AP A	Aminopeptidase A
AP N	Aminopeptidase N
AR	Androgen Receptor
ARBs	Angiotensin II Receptor Blockers
AT$_1$R	Angiotensin II Type 1 Receptor

AT_2R	Angiotensin II Type 2 Receptor
bFGF	basic Fibroblast Growth Factor
BSA	Bovine Serum Albumin
CAGE	Chymostatin-sensitive Angiotensin II-Generating Enzyme
CCN2/CTGF	Connective Tissue Growth Factor
CD31	Cluster of Differentiation 31
COSY	COrrelation SpectroscopY
CPM	Counts Per Minute
CT	Computed Tomography
DMEM	high glucose Dulbecco's Modification of Eagle Medium
EMT	Epithelial-Mesenchymal Transition
ERK	Extracellular signal-Regulated Kinase
ESCC	Esophageal Squamous Cell Carcinoma
ET-1	Endothelin-1
FBS	Fetal Bovine Serum
FOV	Field Of View
HMBC	Heteronuclear Multiple-Bond Correlation
HMQC	Heteronuclear Multiple-Quantum Correlation
HPLC	High-Performance Liquid Chromatography
IL 6	Interleukin 6
JAK-II	Janus Kinase 2
Ki	Inhibition constant

LLC	Lewis Lung Carcinoma
log $D_{7.4}$	Distribution coefficient at pH 7.4
MAS-R	MAS receptors
MCP-1	Monocyte Chemoattractant Protein-1
MS	Mass Spectroscopy
NF-κB	Nuclear Factor kappa light chain enhancer of activated B cells
NMR	Nuclear Magnetic Resonance
PBS	Phosphate-Buffered Saline
PCNA	Proliferating-Cell Nuclear Antigen
PDGF	Platelet-Derived Growth Factor
PET	Positron Emission Tomography
p.i.	post injection
PI3K / Akt	Phosphatidylinositol 3-Kinases / protein kinase B
PSA	Prostate Specific Antigen
QMA	Quaternary Methyl Ammonium
RAS	Renin-Angiotensin System
RCCD	Rotatable Central Composite Design
Rf	Retention factor
RPMI	Roswell Park Memorial Institute medium
RT-PCR	Real-Time Polymerase Chain Reaction
SD	Standard Deviation
SN2	Substitution Nucleophilic two

SPE	Solid-Phase Extraction
SPECT	Single Photon Emission Computed Tomography
STAT3	Signal Transducer and Activator of Transcription 3
TAC	Time-Activity Curves
TGF-β1	Transforming Growth Factor beta 1
TLC	Thin Layer Chromatography
TNFα	Tumor Necrosis Factor α
VEGF	Vascular Endothelial Growth Factor

TABLE OF CONTENTS

1 INTRODUCTION

Cancer is the second leading cause of death globally (WHO, 2018). Therefore, the early detection and accurate diagnosis are key actions to decrease the number of deaths associated with this pathology.

Molecular imaging has become the most efficient tool for cancer diagnosis and therapy follow up. In particular, Positron Emission Tomography (PET) has been considered a valuable modality for cancer imaging because of its high sensitivity to detect cellular and molecular changes *in vivo*. In addition, the fusion of PET with Computed Tomography (CT) has been widely used in oncology since PET/CT imaging combines metabolic and morphological information (Treglia *et al.*, 2014). Among the positron emitter radionuclides with a short half-life, fluorine-18 (^{18}F) is the preferred one by many physicians because of its favorable nuclear and physical properties. This radionuclide has a high branching ratio for positron decay, a convenient short half-life of 110 minutes, and a low maximum energy of the emitted positron, which favors spatial resolution of PET imaging (Jacobson *et al.*, 2015; Conti e Eriksson, 2016). [^{18}F]fluorodeoxyglucose ([^{18}F]FDG) is the PET tracer most commonly used for cancer imaging worldwide. However, [^{18}F]FDG uptake can also occur in benign conditions such as inflammation and infection (Vaidyanathan *et al.*, 2015). Such disadvantages have driven the search for more specific radiotracers.

During the last two decades, several different studies have demonstrated the role of the renin-angiotensin system (RAS) in the development and progression of cancer. Angiotensin II (ANG II) is the effector peptide that exerts most of the physiological functions of RAS, mainly through the angiotensin II type 1 receptor (AT_1R). In cancer, activation of AT_1R by ANG II triggers different mechanisms such as stimulation of vascular endothelial growth factor (VEGF) expression. AT_1R protein expression has been found significantly upregulated in human cells and tumor tissues of breast, prostate, gastric, bladder, pancreatic, ovarian and endometrial-derived cancers compared to non-cancerous tissues

(Watanabe *et al.*, 2003; Suganuma *et al.*, 2005; Uemura *et al.*, 2006; Tanaka *et al.*, 2010; Du *et al.*, 2012; Huang *et al.*, 2014; Ishiguro *et al.*, 2015). The antihypertension drug losartan, an inexpensive drug and selective AT_1R antagonist, has been shown to inhibit breast (Coulson *et al.*, 2017), gastric (Huang *et al.*, 2014) and ovarian (Zhao *et al.*, 2019) cancer development and metastasis suggesting that AT_1R could be a potential therapeutic target to complement current cancer treatment. Hence, ^{18}F-labeled losartan analogs may constitute promising radiotracers for PET imaging of AT_1R-expressing tumors. Although a small number of AT_1R radioligands have already been developed, no imaging studies aimed at identifying AT_1R-positive tumors have been reported so far.

A few analogs of losartan radiolabeled with carbon-11 (^{11}C) and ^{18}F have been used to quantify renal AT_1R in non-cancerous conditions using PET. 2-[^{18}F]fluoro-3-pent-4-yn-1-yloxypyridine ([^{18}F]FPyKYNE)-losartan was the first and only ^{18}F-labeled losartan analog reported to date, to the best of our knowledge, synthetized by click chemistry. This radioligand showed high binding selectivity to renal AT_1R in both rats and (Arksey *et al.*, 2014; Hachem *et al.*, 2016).

Therefore, the aim of the work described in this thesis was to synthesize and evaluate two novel ^{18}F-labeled losartan analogs, [^{18}F]FEtLos and [^{18}F]AMBF$_3$Los, for PET imaging of AT_1R-positive tumors. To accomplish this, less bulky and more hydrophilic ^{18}F-linkers were used. In particular, the one-step ^{18}F-radiolabeling of the alkylammoniomethyltrifluoroborate (AMBF$_3$) motif proved to be a very convenient approach for synthesizing PET tracers. For the first time, AT_1R PET radioligands were evaluated *in vivo* using AT_1R-positive cancer models. PET imaging of AT_1R-positive tumors may allow the selection of patients who will benefit from the combined chemotherapy with ARBs.

2 OBJECTIVES

2.1 General objective

Synthesize and evaluate two novel AT_1R radioligands [^{18}F]FEtLos and [^{18}F]$AMBF_3$Los for PET imaging of AT_1R-positive tumors.

2.2 Specific objectives

1 Synthesize and characterize by Mass Spectrometry (EM) and Nuclear Magnetic Resonance (NMR) the cold compounds FEtLos and $AMBF_3$Los

2 Perform the ^{18}F-radiolabeling and quality control of the hot compounds [^{18}F]FEtLos and [^{18}F]$AMBF_3$Los

3 Assess the AT_1R binding affinity and specificity of [$^{19/18}$F]FEtLos and [$^{19/18}$F]$AMBF_3$Los

4 Evaluate the tumor uptake and biodistribution pathways of [^{18}F]FEtLos and [^{18}F]$AMBF_3$Los in AT_1R-positive tumor-bearing mice

3 BIBLIOGRAPHIC REVIEW

3.1 Cancer

Cancer refers to a group of diseases characterized by an abnormal and uncontrolled cell growth in which cells may acquire the potential to invade other tissues (Saito *et al.*, 2015). Tumors are considered benign if they lack the ability to invade neighboring tissue and grow locally, while malignant tumors have the ability to invade and metastasize (Saito *et al.*, 2015). Metastasis is a multi-step process comprising local tumor invasion, entry into the vasculature and colonization of primary tumor cells to distant organs. This process involves an interplay between tumor cells and the surrounding microenvironment in order to sustain tumor survival in the new organs (Saito *et al.*, 2015).

Hanahan and Weinberg (2000; 2011) highlighted all the features that allow a normal cell to acquire tumorigenic properties and called them the “hallmarks of cancer”. The hallmarks of cancer comprise eight biological capabilities acquired during the multistep development of tumors. Their acquisition is made possible by two enabling characteristics (genome instability and mutation, and tumor-promoting inflammation), that are not hallmarks, but enable the hallmarks to happen.

The hallmarks include: sustaining proliferative signaling; evading growth suppressors; avoiding immune destruction; enabling replicative immortality; activating invasion and metastasis; inducing angiogenesis; resisting cell death; and deregulating cellular energetics (Hanahan and Weinberg, 2011). The RAS has been associated with proliferative signaling, evasion to growth suppressors, induction of angiogenesis and resistance to cell death (Wegman-Ostrosky *et al.*, 2015). In fact, the use of RAS blockers has been suggested as chemo-prophylactic agents for cancer prevention and coadjuvant drugs in cancer treatment (Wegman-Ostrosky *et al.*, 2015; Zhao *et al.*, 2019).

According to the World Health Organization, cancer is the second leading cause of death globally, and was responsible for 9.6 million deaths in 2018. Cancers of the lung, colorectal, stomach, liver and female breast are ranked within the top five in terms of mortality (WHO, 2018; IARC, 2018). The increased cancer burden is due to many factors such as population growth, aging, and social and economic development (IARC, 2018). The International Agency for Research on Cancer showed that one in 6 women and one in 5 men worldwide are expected to develop cancer during their lifetime, while one in 11 women and one in 8 men die from the disease (IARC, 2018). Unfortunately, patients with cancer are frequently diagnosed at a late phase when treatment is ineffective. Therefore, there is an urgent need to develop efficient strategies for the early and accurate diagnosis of cancer. Several radiolabeled compounds have been designed, synthesized and evaluated as imaging tools for refined diagnostic applications such as cancer diagnosis and staging. The most widely used radiotracer for cancer diagnosis is [^{18}F]FDG, which targets tumor metabolism. However, [^{18}F]FDG accumulation is not specific of tumor cells and can be found in non-cancerous conditions like inflammation or infection. These limitations have led researchers from all over the world to look for more specific cancer biomarkers.

3.2 Renin-Angiotensin System

3.2.1 Physiology

The Renin-Angiotensin System is a master regulator of blood pressure and fluid homeostasis (Crowley and Coffman, 2012), acting through different enzymes, peptides and receptors such as the AT_1R (Figure 1).

Figure 1 – Schematic representation of the renin angiotensin system. The classical circulating RAS comprising the angiotensin II, formed by an ACE-dependent pathway, is represented by blue arrows. Red arrows represent the formation of other angiotensin peptides and the MAS receptor as part of the contemporary RAS. Black arrows indicate formation of ANG II by an ACE-independent pathway.

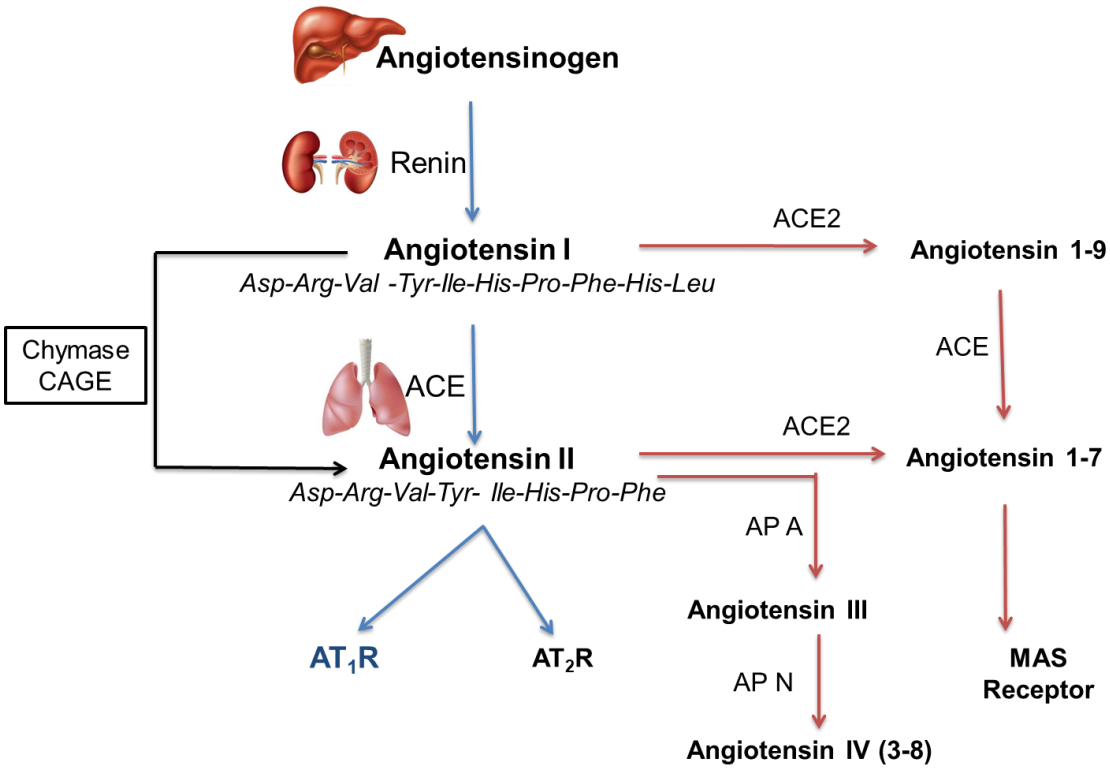

Source: Modified from Paul *et al.* (2006); George *et al.* (2010); Crowley and Coffman (2012); Uehara *et al.* (2013); Rodrigues-Ferreira and Nahmias (2015); Xie *et al.* (2017).

Angiotensinogen, the precursor of angiotensin, is an α-glycoprotein released from the liver to the systemic circulation (Paul *et al.*, 2006), where it is cleaved by renin and converted to the decapeptide angiotensin I (ANG I). Renin is an enzyme secreted by the juxtaglomerular apparatus of the kidney in response to a decrease in arterial blood pressure or plasma sodium (Paul *et al.*, 2006; George *et al.*, 2010). ANG I is then converted to the octapeptide ANG II by the angiotensin converting enzyme (ACE), a membrane-bound metalloproteinase expressed in the luminal side of lung endothelial cells (Paul *et al.*, 2006; George *et al.*, 2010). ANG II binds with high affinity to two G-protein coupled receptors: Angiotensin II type 1 (AT_1R) and type 2 (AT_2R) receptors, which leads to vasoconstriction, retention of water and sodium, thirst and salt-appetite sensations, and increases plasma aldosterone (George *et al.*, 2010). AT_1R activates growth-promoting pathways and mediates different actions such as vasoconstriction, stimulation of renal tubular

sodium reabsorption, release of aldosterone from the adrenal glomerulosa, cardiac contractility and stimulation of hypothalamic thirst sensors (Dasgupta and Zhang, 2011; Crowley and Coffman, 2012). On the other hand, AT_2R has opposite functions including vasodilatation, anti-proliferation, anti-fibrosis, hypotension, and anti-hypertrophic effects (Dasgupta and Zhang, 2011; Lau and Leung, 2011). AT_1R can be found in many adult tissues such as kidney, liver, adrenal cortex, vasculature, heart, lung and brain, while AT_2R expression is mostly found during fetal development, but can be present in adrenal medulla, uterus, ovarian follicles, kidney and brain (Ager *et al.*, 2008; Dasgupta and Zhang, 2011; Crowley and Coffman, 2012). ANG II binds to AT_1R through several interactions: Feng *et al*. (1995) reported that histidine^{183} and aspartate ^{281}, both located in the extracellular domain of the AT_1R, bind to the NH_2-terminal aspartate^{1} and arginine^{2} residues of ANG II, respectively. Lysine^{199}, present in the transmembrane-helix-5 of the AT_1R, binds to the COOH-terminal alpha-carboxyl group of ANG II (Feng *et al.*, 1995; Noda, Saad, Kinoshita*, et al.*, 1995). Additional interactions were also reported, one between phenylalanine^{8} of ANG II with lysine^{199} and histidine^{256} of AT_1R, and the other between tyrosine^{4} of ANG II and asparagine^{111} (Noda, Saad e Karnik, 1995; Miura *et al.*, 2011).

Additional components of the system such as angiotensin converting enzyme two (ACE2), aminopeptidase A (AP A), aminopeptidase N (AP N), other angiotensin peptides (angiotensin 1-9, 1-7, III, IV) and MAS receptors (MAS-R) have been identified, representing the contemporary RAS (George *et al.*, 2010; Rodrigues-Ferreira and Nahmias, 2015). Angiotensin 1-7 (ANG 1-7) is another important effector peptide that binds to the MAS-R, a G-protein coupled receptor. ANG 1-7 acts as a vasodilator (Ager *et al.*, 2008). The MAS-R leads to vasodilatation, and has anti-proliferation, anti-hypertrophy and anti-fibrosis effects (Lau and Leung, 2011). Expression of the MAS-R was reported in kidneys, heart and eyes (Dias-Peixoto *et al.*, 2012; Pinheiro and Simões E Silva, 2012; Vaajanen *et al.*, 2015).

ANG II may also be generated by an ACE-independent pathway, for instance, via chymase and chymostatin-sensitive angiotensin II-generating enzyme (CAGE)-dependent mechanisms (George *et al.*, 2010; Uehara *et al.*, 2013).

Besides the circulating RAS, many organs have a local tissue RAS such as heart, ovary, brain, digestive organs and eyes (Paul *et al.*, 2006; George *et al.*, 2010; Ino *et al.*, 2011; Giese and Speth, 2014).

As RAS exerts fundamental control over sodium and water handling in the kidney, its dysregulation leads to blood pressure elevation with resulting in renal and cardiovascular damage (Crowley and Coffman, 2012). Atherosclerosis, ischemic disease, hypertension, heart failure, and other pathologies have been associated to the dysregulation of RAS (Rodrigues-Ferreira and Nahmias, 2015). Accordingly, several ACE inhibitors and AT_1R blockers (for instance, losartan) are commercially available drugs that antagonize RAS in order to treat these pathologies.

3.2.2 Role in cancer

RAS components have been identified in several human cancers being the AT_1R expression the most highlighted as mediator of the pro-tumor role of ANG II. AT_1R is composed of 359 amino acids, with seven-transmembrane domains (Dasgupta and Zhang, 2011; Miura *et al.*, 2011) and is encoded by one gene in humans (AGTR1), and two highly homologous isoforms ($AGTR1_A$ and $AGTR1_B$) in rodents (George *et al.*, 2010).

AT_1R expression was reported in human breast cancer cells (Du *et al.*, 2012; Chen *et al.*, 2013), prostate (Uemura *et al.*, 2003; Uemura *et al.*, 2006; Kosaka *et al.*, 2010), bladder (Kosugi *et al.*, 2007; Tanaka *et al.*, 2010), gastric (Carl-Mcgrath *et al.*, 2007; Huang *et al.*, 2008; Huang *et al.*, 2014), glioblastoma (Juillerat-Jeanneret *et al.*, 2004), pancreas (Gong *et al.*, 2010; Lau and Leung, 2011), ovarian (Suganuma *et al.*, 2005), and endometrial (Watanabe *et al.*, 2003). AT_1R expression was also detected in tumor tissues from patients with breast cancer (Du *et al.*, 2012; Chen *et al.*, 2013; Coulson *et al.*, 2017), prostate cancer (Uemura *et al.*, 2003; Uemura *et al.*, 2006; Guimond *et al.*, 2013), pancreatic cancer (Arafat *et al.*, 2007; Ishiguro *et al.*, 2015), bladder cancer (Kosugi *et al.*, 2007; Tanaka *et al.*, 2010), gastric cancer (Röcken *et al.*, 2007; Huang *et al.*, 2014), ovarian carcinoma (Suganuma *et al.*, 2005), endometrial carcinoma (Watanabe *et al.*, 2003), colorectal carcinoma (Zhou *et al.*, 2014), renal clear-cell carcinoma (Dolley-Hitze *et al.*, 2010), and oral cancer (Chen, 2016), where it's expression was significantly higher than in healthy tissues. Indeed, AT_1R was

found to be weakly expressed in 14% of benign cystadenomas and overexpressed in 22% of the borderline of malignant tumors, and in 55% of invasive ovarian adenocarcinomas (Suganuma *et al.*, 2005). In human colorectal tumor tissues, AT_1R expression was positively correlated with cancer progression, liver metastasis and pathological stage (Zhou *et al.*, 2014). These findings suggested that AT_1R expression increases with the grade of malignancy.

The biological actions and signaling mechanisms by which AT_1R-pathway contribute to tumor biology have been intensively studied. AT_1R mediates the anti-apoptotic role of ANG II in breast cancer cells through activation of phosphatidylinositol 3-kinases / protein kinase B (PI3K/Akt) signaling, and subsequent suppression of caspase-9 activation (Zhao *et al.*, 2008). The activation of the ANG II/AT_1R axis in breast cancer cells led to cell growth, increased levels of proliferating-cell nuclear antigen (PCNA) and cyclin D1 protein and decreased levels of the tumor suppressor p53 (Du *et al.*, 2012). AT_1R also mediated cell migration in breast cancer cells through PI3K/Akt and NF-kB (nuclear factor kappa light chain enhancer of activated B cells) pathways, and increasing the enzymatic activities of the matrix metalloproteinases MMP-2 and MMP-9 (Zhao *et al.*, 2014). MMP-2 and -9 play a significant role in cancer invasion and metastasis by degrading the extracellular matrix and destroying the basement membranes (Zhao *et al.*, 2014). Furthermore, AT_1R overexpression promoted angiogenesis *in vivo*, and induced the epithelial-mesenchymal transition (EMT) by reducing E-cadherin expression and increasing EMT-related transcription factors such as phospho-Smad3, Smad4 and Snail (Oh *et al.*, 2016). EMT, characterized by the loss of cell polarity and cell-cell adhesion, is considered a critical step in cancer progression because it enhances cell migration and invasion (Oh *et al.*, 2016). AT_1R-expressing breast tumors presented a high number of Ki-67-positive cells (a marker of cell proliferation), exhibited low levels of E-cadherin and upregulated MMP-9 (Oh *et al.*, 2016) that conferred tumor cells an increased ability to migrate, invade and induce angiogenesis, thus promoting breast tumor growth. Mammary tumor progression was also enhanced by AT_1R-dependent cytokine production (Coulson *et al.*, 2017).

It was also found that ANG II/AT_1R signaling upregulated the expression of the transcriptional control gene PAX2 (paired box gene 2) in prostate cancer cells through phosphorylation of ERK1/2, JAK-II (Janus kinase 2),

and STAT3 (signal transducer and activator of transcription 3), increasing the proliferation of cancer cells (Bose *et al.*, 2009). ANG II/AT_1R signaling was also found to increase the protein levels of the androgen receptor (AR), the prostate specific antigen (PSA), NF-kB and c-myc. Knocking down of AT_1R reduced the transcriptional level of AR, NF-kB and c-myc, resulting in a significant inhibition of cell growth (Hoshino *et al.*, 2011). Additionally, AT_1R was reported to induce the expression of the inflammatory cytokine MCP-1 (monocyte chemoattractant protein-1) via PI3K/Akt signaling pathway in prostate cancer cells, which led to macrophage infiltration and tumor cell proliferation (Shirotake *et al.*, 2012).

ANG II/AT_1R signaling significantly stimulated VEGF expression in endometrial, ovarian, pancreatic, prostate, bladder and breast cancer, inducing angiogenesis and cell proliferation (Watanabe *et al.*, 2003; Suganuma *et al.*, 2005; Anandanadesan *et al.*, 2008; Kosaka *et al.*, 2010; Tanaka *et al.*, 2010; Tanaka *et al.*, 2011; Chen *et al.*, 2013). In pancreatic cancer, VEGF production was found to be stimulated via AT_1R - ERK1/2 -dependent mechanism (Anandanadesan *et al.*, 2008).

In summary, AT_1R is frequently expressed in human tumor cells and plays a significant role in proliferation, migration, invasion, angiogenesis and tumor survival through the activation of several downstream effectors such as kinases, transcription factors, matrix metalloproteinases, growth factors, and the suppression of caspases and p53. These findings suggest AT_1R as potential cancer therapeutic target and a useful marker for the detection of tumors. Hence, the development of new radiotracers for the detection of AT_1R-positive tumors may constitute a promising strategy for monitoring cancer treatment.

3.3 Losartan

The antihypertension drug losartan is a selective AT_1R antagonist and inexpensive pharmaceutical widely used in the treatment of hypertension (Kim *et al.*, 2014). Losartan is the commercial name of the compound 2-butyl-4-chloro-5-hydroxymethyl-1-[(2´-(1*H*-tetrazol-5-yl)biphenyl-4-yl)methyl]-1*H*-imidazole (Figure 2), which was initially known as “DuP 753”. The affinity of losartan for the AT_1R is 3000-fold higher than for the AT_2R (Mathews e Szabo, 2010).

Figure 2 – Chemical structure of losartan

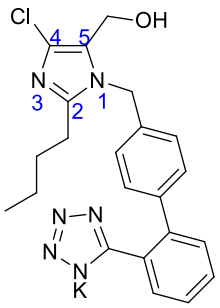

Source: thesis author.

When losartan was discovered as an antihypertensive molecule, several structure-activity studies uncovered that the tetrazole-containing group displayed the highest affinity for AT_1R (Carini *et al.*, 1991). Besides the tetrazole group, the imidazole ring was also described as an important site for AT_1R binding and could be modified as following: (1) with an alkyl chain of 3-4 carbon atoms in length at the 2-position; (2) with a large, electronegative and lipophilic substituent in the 4-position; (3) with a hydrogen-bonding substituents in 5-position, but could also tolerate a wide range of groups (Carini *et al.*, 1991). Further refinement with docking studies suggested that the salt bridge formed between the tetrazole moiety and the arginine residue of the AT_1R is the key interaction site of losartan (Zhang *et al.*, 2015). Therefore, a key feature of the binding of losartan to AT_1R is the presence of a tetrazole moiety with mobile hydrogen.

Losartan is the most commonly used AT_1R blocker to study the role of AT_1R in tumor growth and cancer progression. Several studies have demonstrated that losartan inhibits the tumor growth, angiogenesis, proliferation, migration, invasion and survival of tumor cells through blocking of AT_1R (concentration of losartan ranging from 10 to 100 µM, for *in vitro* studies; and from 70 to 90 mg/kg *in vivo* studies in rodents) (Rivera *et al.*, 2001; Arrieta *et al.*, 2005; Anandanadesan *et al.*, 2008; Zhao *et al.*, 2008; Bose *et al.*, 2009; Zhao *et al.*, 2010; Chen *et al.*, 2013; Huang *et al.*, 2014; Zhao *et al.*, 2014; Oh *et al.*, 2016; Coulson *et al.*, 2017). Rivera *et al.* (2001) reported that the oral administration of losartan (80 mg/kg/d) to glioma C6-bearing rats, reduced up to 79% the tumor size with a significant decrease in the vascular density, mitotic index and cell proliferation. Using the same tumor model, Arrieta *et al.* (2005) further reported that treatment of rats with losartan (80 mg/kg/d) increased the apoptotic rate *in vivo* and decreased the

synthesis of VEGF, basic fibroblast growth factor (bFGF) and platelet-derived growth factor (PDGF).

In breast cancer, *in vitro* studies have shown that losartan completely suppressed the anti-apoptotic effect of ANG II and significantly inhibited the cell-cycle (S-phase) progression induced by ANG II (Zhao *et al.*, 2008; Zhao *et al.*, 2010). Losartan also downregulated the expression of VEGF in MCF7 cells, and abolished MMP-2 and MMP-9 enzyme activity in MDA-MB-231 cells treated with ANG II (Chen *et al.*, 2013; Zhao *et al.*, 2014). *In vivo* studies showed that the administration of losartan (90 mg/kg) every other day to Balb/c female nude mice inoculated with AT_1R-overexpressing MCF7 tumors, led to upregulation E-cadherin, downregulation of vimentin and CD31-positive microvessels in both the peritumoral and intratumoral areas (Oh *et al.*, 2016). Coulson *et al.* (2017) reported that the therapeutic inhibition of AT_1R with losartan (70 mg/kg/d) *in vivo* inhibited mammary tumor progression from ductal carcinoma *in situ* to invasive cancer by significantly reducing tumor cytokine levels such as tumor necrosis factor α (TNFα) and interleukin 6 (IL 6) (Coulson *et al.*, 2017).

In addition, losartan blocked PAX2 phosphorylation stimulated by ANG II in prostate cancer cells (Bose *et al.*, 2009) and induced the apoptosis of human pancreatic cancer cells while increasing the expression of cyclin-dependent kinase inhibitors (p21 and p27), p53 and Bax, caspase-3 activation and down-regulating Bcl-2 expression (Gong *et al.*, 2010).

Several authors have also mentioned synergistic effects of losartan and chemotherapeutic drugs, such as gemcitabine, against cancer. For instance, Kim *et al.* (2014) reported that pancreatic cancer cell proliferation was significantly reduced in cells treated with gemcitabine plus losartan than in cells only treated with each drug independently. Also, Zhao *et al*. (2019) reported that losartan treatment enhances the efficacy of paclitaxel in an experimental model of ovarian cancer and ovary cancer patients receiving angiotensin system inhibitors together with standard chemotherapy exhibited 30 months longer overall survival compared with patients on other antihypertensives.

It has also been demonstrated that losartan exerts an antifibrotic role in tumors, enhancing drug and oxygen delivery to tumors. Chauhan *et al.* (2013) demonstrated that losartan decompressed the tumor blood vasculature by reducing stromal collagen and hyaluronan production via a decreased expression

of profibrotic signals such as TGF-β1 (transforming growth factor beta 1), CCN2/CTGF (connective tissue growth factor) and ET-1 (endothelin-1).

These data suggest that losartan could be used to treat AT_1R-positive tumors to improve chemotherapy outcomes. Therefore, the detection and quantification of AT_1R on tumors using imaging modalities could guide cancer therapy in a non-invasive and more efficient way.

3.4 Positron Emission Tomography/ Computed Tomography in Oncology

The hybrid Positron Emission Tomography/Computed Tomography (PET/CT) system is an imaging modality widely used in nuclear medicine for diagnosing, staging and monitoring therapy in cancer patients. PET scan is a valuable method of cancer detection that provides a noninvasive metabolic and functional characterization of the tumor. CT scan, on the other hand, complements the PET scan by providing detailed information on the morphology, size and location of the tumor (Treglia *et al.*, 2014). While PET scanners detects the coincidental photons produced by positron annihilation of radioisotopes, CT scanners use a rotating X-ray machine to image thin slices of the body to diagnose a wide variety of injuries (Weissleder and Pittet, 2008).

PET is a molecular imaging technique which uses radiopharmaceuticals labeled with positron emitting radioisotopes (for example, ^{18}F). PET allows the visualizing, characterizing and measurement of biological processes at the molecular and cellular levels in a living system through quantitative tomographic images (Vallabhajosula, 2007; Fukuda *et al.*, 2013). The basis of PET imaging is the simultaneous detection of two 511-keV photons produced by positron annihilation (Chatziioannou, 2005). The emitted positrons travel a short distance inside the tissue and lose energy by excitation, ionization and radiation; they subsequently thermalize and are annihilated with nearby electrons emitting two 511-keV photons in opposite directions (Figure 3). Because of the thermal vibrations in the tissues, these photons have an additional deviation of 180^o from one another (Chatziioannou, 2005).

Figure 3 – Representative scheme of the basis of PET imaging: simultaneous detection of two 511-keV photons produced by positron annihilation. Positron range is the distance traveled by the emitted positron, on average, in the surrounding medium before reaching thermal energy in order to be annihilated.

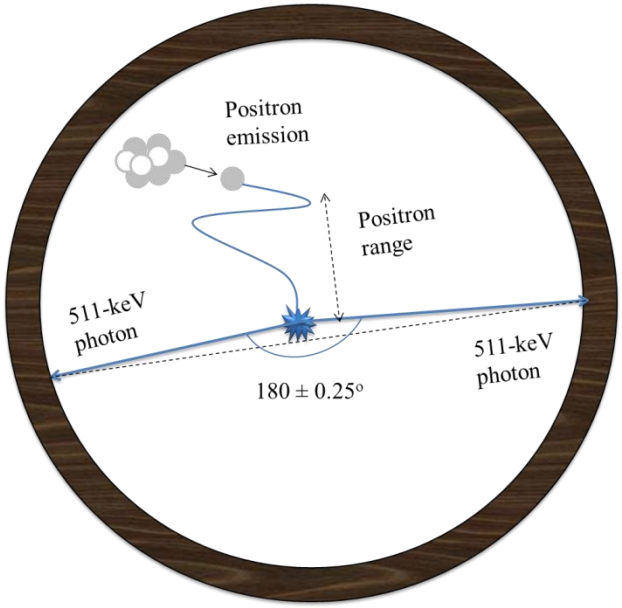

Source: Rahmim and Zaidi (2008).

PET is a highly sensitive imaging system because of its ability to detect and record a higher percentage of emitted events compared to SPECT (single photon emission computed tomography) (Rahmim and Zaidi, 2008). PET sensitivity implies an improved image quality, the possibility to perform shorter scans and multiple scans of a patient at different fields of view in a reasonable time and, an improved ability to study dynamic biological processes (Rahmim and Zaidi, 2008).

PET/CT fusion has notably improved imaging outcomes and is nowadays widely used in oncology: (1) to identify the site(s) of the primary tumor and metastasis; (2) for cancer staging; (3) to identify any residual disease after treatment; (4) to detect recurrences; (5) to measure tumor response to therapy and, (6) guide radiation therapy (Vallabhajosula, 2007). Therefore, PET/CT imaging is a powerful system to detect tumors and monitor anticancer therapy.

3.5 Positron emitters

Positron emission results from the radioactive decay of a proton-rich nuclides. It is known as a beta-plus (β^+) decay where a proton (p) is converted into a neutron (n), a positron (e^+) and a neutrino (ν) within the nucleus (Figure 4A). The

daughter nucleus has the mass number of the mother nucleus, and the atomic number minus one unit (Figure 4B). Beta-plus decay can occur only if the mass of the mother nuclide is at least two electron masses higher than the mass of the daughter nuclide (Lieser, 2001).

Figure 4 – Beta-plus decay. General scheme of decay (A). Example scheme: β^+ decay of ^{18}F-fluorine (B).

$$p \rightarrow n + e^+ + \nu \qquad \text{(A)}$$

$$^{18}_{9}F \rightarrow {}^{18}_{8}O + {}^{0}_{+1}e + \nu \qquad \text{(B)}$$

Source: thesis author.

The characteristics of pure positron emitters are represented in Table 1. They are considered pure PET radioisotopes for lacking relevant contribution of gamma emissions in coincidence with the annihilation radiation (Conti and Eriksson, 2016).

Table 1 – Positron-emitting radioisotopes

Radioisotope	Half-life	Branching (β^+)	E_{max} (MEV) - β^+	R_{max} (mm) - β^+
^{15}O (oxygen-15)	2 min	99.9%	1.732	8.4
^{13}N (nitrogen-13)	10 min	99.8%	1.199	5.5
^{11}C	20.4 min	99.8%	0.960	4.2
^{18}F	110 min	96.9%	0.634	2.4
^{64}Cu (copper-64)	12.7 h	17.5%	0.653	2.5
^{89}Zr (zirconium-89)	78.4 h	22.7%	0.902	3.8

Source: Modified from Conti and Eriksson (2016).

In particular, ^{18}F has been recognized as the positron emitter with the most favorable properties for PET imaging. ^{18}F has a high branching ratio for β^+ decay (96.9%) and a convenient short half-life for longer PET scans and radiosynthesis compared with ^{15}O, ^{13}N and ^{11}C. In contrast with those radionuclides, the half-life of ^{18}F allows performing PET studies without having an on-site cyclotron. ^{18}F displays a low maximum energy of the emitted positron (E_{max}) and subsequently, a short maximum range in water (R_{max}), which favors spatial resolution of PET images (Cole *et al.*, 2014; Jacobson *et al.*, 2015; Conti e

Eriksson, 2016). The low positron energy also reduces the radiation dose to patients (Dollé, 2007).

3.6 Production of fluorine-18

The fluorine element belongs to the halogen family, represented by the group 17 in the periodic table, and possesses an atomic number of 9 and an atomic weight of 19. It has a small van der Waals radius (1.47 A^o) and it is the most electronegative element (3.98 Pauling scale) (Shah e Westwell, 2007). Fluorine-19 (^{19}F) is the unique stable isotope of the fluorine element with a natural abundance of 100%. In contrast, ^{18}F is radioactive and decays by positron emission into ^{18}O. ^{19}F and ^{18}F are the most known isotopes of the fluorine element.

In medicinal chemistry, the role of fluorine has been highlighted because it can reduce drug metabolism and influence membrane permeability by modulating the lipophilicity of compounds (Gillis *et al.*, 2015). At the same time, the favorable properties of ^{18}F for PET imaging are well-recognized in nuclear medicine.

^{18}F is readily available from cyclotrons and can be obtained in different chemical forms. Several nuclear reactions have been reported for the production of ^{18}F (Lasne *et al.*, 2002; Coenen, 2007) and are summarized in Table 2.

Table 2 – Methods for ^{18}F production.

Entry	Nuclear reaction	Target	Product	Specific Activity GBq/μmol
1	$^{18}O(p,n)^{18}F$	$H_2{}^{18}O$	$[^{18}F]F^-$	10–7000
2	$^{18}O(p,n)^{18}F$	$^{18}O_2$, Kr (50 μmol F_2)	$[^{18}F]F_2$	0.6
3	$^{16}O(^3He,p)^{18}F$	H_2O	$[^{18}F]F^-$	50
4	$^{20}Ne(d,\alpha)^{18}F$	0.1% F_2 / Ne	$[^{18}F]F_2$	0.030–0.370
5	$^{20}Ne(d,\alpha)^{18}F$	15% H_2 / Ne	$[^{18}F]HF$	100–1000

Source: Modified from Lasne *et al.* (2002); Coenen (2007).

Proton irradiation of oxygen-18 (^{18}O) (entry 1, Table 2), and helium-3 (^3He) irradiation of oxygen-16 (^{16}O) (entry 3, Table 2) can produce aqueous [^{18}F]fluoride ($[^{18}F]F^-$) for nucleophilic labeling methods. Deuterium (d) irradiation of neon-20 (^{20}Ne) using 15% H_2/Ne (entry 5, Table 2) as target can produce

[^{18}F]hydrogen fluoride ([^{18}F]HF), another nucleophilic specie; however, the use of the Ne/H_2 target for [^{18}F]HF production is still a complicated process (Lasne *et al.*, 2002). Although the proton irradiation of ^{18}O increases the cost of ^{18}F production due to the ^{18}O enrichment of water, ^{18}O(p,n)^{18}F with the $H_2{}^{18}O$ (^{18}O-enriched water) is the most used method to produce ^{18}F to date because it yields no-carrier-added ^{18}F with a high specific activity.

[^{18}F]F_2, on the other hand, can be obtained by proton irradiation of ^{18}O (entry 2, Table 2) or deuterons irradiation of ^{20}Ne (entry 4, Table 2), both gas as target materials. The produced [^{18}F]F_2 gas is adsorbed to the target walls (Coenen, 2007) and requires the addition of a carrier to extract ^{18}F. Consequently, [^{18}F]F_2 gas is produced with low specific activity because ^{19}F gas is used as a carrier in the process (Coenen, 2007 ; Jacobson *et al.*, 2015).

The specific activity of ^{18}F in the irradiated target material is very important to obtain radiopharmaceuticals with an appropriate molar activity for *in vivo* use. The molar activity is defined as the measured radioactivity per mole of compound, expressed in Bq/mol or GBq/µmol. Taking into account the relatively low concentration of receptors (in target tissues about 10 pmol/mg tissue), the molar activity should be as high as possible to avoid saturation and to ensure maximal binding of the radioligand to the receptor (Elsinga, 2002). The addition of a carrier increases the mass of the final radiopharmaceutical, which may saturate the target receptor with non-radioactive ligand, thus reducing the PET signal (Cai *et al.*, 2008 ; Jacobson *et al.*, 2015). Furthermore, radiopharmaceuticals with high molar activity enable their administration to patients without toxic or pharmacological effects (Cai *et al.*, 2008). Therefore, most of the reported ^{18}F-tracers have been synthetized using nucleophilic [^{18}F]F^- produced by the proton irradiation of $H_2{}^{18}O$ (entry 1, Table 2).

3.7 Radiolabeling with fluorine-18

^{18}F-labeled compounds are prepared using several methods, which may involve direct nucleophilic or electrophilic substitutions, indirect fluorination using prosthetic groups, click chemistry and ^{18}F-^{19}F isotope exchange reactions.

3.7.1 Nucleophilic [^{18}F]fluorination

Nucleophilic fluorination with [^{18}F]F^- usually provides ^{18}F-tracers with high molar activity. However, [^{18}F]F^- is a poor nucleophile in water (Lasne *et al.*, 2002; Cole *et al.*, 2014).

[^{18}F]F^- is strongly hydrated because of the high charge density of anions (hydration enthalpy = 506 kJ/mol), which renders [^{18}F]F^- non reactive for nucleophilic reactions (Coenen, 2007). To overcome this, the aqueous solution of no-carrier-added [^{18}F]F^- is loaded onto anion exchange resins cartridges, eluted with a small volume of aqueous solution, and then dried by the successive additions of acetonitrile (MeCN) followed by azeotropic distillations. The quaternary methyl ammonium (QMA) anion exchange column is commonly used to concentrate the [^{18}F]F^- and consequently, recover the $H_2{}^{18}O$. The [^{18}F]F^- trapped on the anion exchange column is usually eluted with MeCN / water mixture containing potassium carbonate (K_2CO_3) and kryptofix 222. Kryptofix 222 (K_{222}) is a phase transfer catalyst that complexes potassium while [^{18}F]F^- is eluted with a high nucleophilicity and solubility in organic solvents (Jacobson *et al.*, 2015). Once the [^{18}F]F^- is dehydrated, the nucleophilic [^{18}F]fluorination takes place in aliphatic or aromatic positions.

3.7.1.1 ^{18}F-Nucleophilic aliphatic substitution

The aliphatic nucleophilic substitution with [^{18}F]F^- requires precursors containing an appropriated leaving group and occurs through a nucleophilic bimolecular (SN2) reaction in polar aprotic solvents (Coenen, 2007 ; Jacobson *et al.*, 2015). The SN2 mechanism involves the attack of a nucleophile to the carbon atom and, simultaneously, a leaving group is displaced; it is also characterized by the inversion of configuration at the carbon atom under attack (Clayden, J. *et al.*, 2012). The rate of SN2 reaction is higher for less substituted compounds, and depends both on the nucleophile and on the carbon skeleton, along with the leaving group, the temperature and the solvent (Clayden, J. *et al.*, 2012). Sulfonate esters (triflate, mesylate, tosylate) and halogens (chlorine, bromine and iodine) are examples of widely used leaving groups (Coenen, 2007 ; Jacobson *et al.*, 2015). Methyl and primary alkyl groups reacts faster by the SN2 mechanism (Clayden, J. *et al.*, 2012).

^{18}F-labeling conditions, through SN2 reactions, involve temperature ranging from 80 ^{o}C to 160 ^{o}C for 10 to 30 min (Elsinga, 2002). Although dimethyl sulfoxide (DMSO) and N,N- dimethylformamide (DMF) may be used as solvents, MeCN is the most commonly used because it can be easily removed by evaporation facilitating the purification of labeled compounds by High-Performance Liquid Chromatography (HPLC) (Elsinga, 2002). DMSO and DMF are preferably used in radiofluorinations performed at temperatures higher than 100 ^{o}C. In addition, elimination reactions can compete with nucleophilic substitution because: (1) fluoride is a strong base in polar aprotic solvents; (2) the reaction mixture is basic, and (3) in general the reaction is set at high temperature (Coenen, 2007; Clayden, Jonathan *et al.*, 2012).

3.7.1.2 ^{18}F-Nucleophilic aromatic substitution

Nucleophilic aromatic substitution takes place in activated aromatics by the electron withdrawing inductive effect of substituents in *ortho* or *para* position to the leaving group on the phenyl ring (Lasne *et al.*, 2002; Coenen, 2007 ; Jacobson *et al.*, 2015). The activating aryl substituents may be nitro, ciano, trifluoromethyl and carbonyl groups (Lasne *et al.*, 2002; Coenen, 2007 ; Jacobson *et al.*, 2015). Nitro groups and trimethylammonium salts are considered good leaving groups and can enhance the fluorination yields (Lasne *et al.*, 2002; Coenen, 2007). Aromatic fluorination on trimethylammonium groups usually requires temperatures between 100 and 110 ^{o}C, while higher temperatures (120 – 180 ^{o}C) are needed for substitution of the nitro group (Jacobson *et al.*, 2015). No-carrier-added nucleophilic aromatic substitutions also call for polar aprotic solvents such as MeCN, DMF or DMSO (Jacobson *et al.*, 2015). A major advantage of the ^{18}F-tracers prepared by aromatic [^{18}F]fluorination is the generally good metabolic stability (Coenen, 2007).

3.7.2 Electrophilic [^{18}F]fluorination

On the other hand, electrophilic ^{18}F-substitution may be another synthetic method to develop ^{18}F-tracers whose precursors are unavailable to no-carried-added nucleophilic ^{18}F-substitution, for instance, radiolabeling of electron-rich aromatic rings and alkenes (Coenen, 2007 ; Jacobson *et al.*, 2015). Electrophilic [^{18}F]fluorinations are performed with the carrier-added [^{18}F]F_2 gas, which is produced with low specific activity (Coenen, 2007 ; Jacobson *et al.*,

2015). So, it is expected that the resulting ^{18}F-tracers will have low molar activities, which is undesirable for ligand-receptor binding studies.

[^{18}F]F_2 gas is highly reactive and can be used for the electrophilic [^{18}F]fluorination directly from the target (Coenen, 2007). However, the high reactivity of [^{18}F]F_2 gas leads to low selectivity and reduced radiochemical yields (Cole *et al.*, 2014). In order to increase the yield and selectivity, [^{18}F]F_2 must be converted into a less reactive species such as [^{18}F]acetylhypofluorite ([^{18}F]CH_3COOF) and [^{18}F]xenon difluoride ([^{18}F]XeF_2), which are then used as intermediate electrophilic fluorination reagents (Coenen, 2007 ; Cole *et al.*, 2014; Jacobson *et al.*, 2015). The electrophilic derivatives of [^{18}F]F_2 also drive to low regioselectivity and undesired radical side reactions (Coenen, 2007 ; Jacobson *et al.*, 2015).

In addition, electrophilic ^{18}F-substitution reactions have a theoretical maximum radiochemical yield of 50% (Coenen, 2007 ; Cole *et al.*, 2014; Jacobson *et al.*, 2015). This 50% radiochemical yield is due to the carrier ^{19}F gas, and consequently, every [^{18}F]F_2 molecule carries only one ^{18}F atom (Coenen, 2007). Besides, the purification of the desired labeled product is a challenge due to the resulted mixture of fluoro isomers (Coenen, 2007 ; Cole *et al.*, 2014; Jacobson *et al.*, 2015), and the electrophilic synthesis of [^{18}F]FDG is an example of purification complexity (Yu, 2006).

3.7.3 [^{18}F]Fluorination using prosthetic groups

Although direct [^{18}F]fluorination is attractive for the development of PET tracers because it is faster and the final target molecule is obtained with lower degree of chemical modifications, most of the time it is not feasible. Direct fluorination usually requires high temperatures and non-physiological pH that can be harsh to precursors such as peptides, proteins and oligonucleotides (Jacobson *et al.*, 2015). In most cases, the chemical structure of the target precursor for ^{18}F-radiolabeling needs to be modified, for instance, converted to a hydroxyl moiety into a tosyl group, and other moieties need to be protected in order to be able to react with ^{18}F without the formation of undesirable labeled compounds. Hence, radiochemists often perform ^{18}F-radiolabeling using prosthetic groups (indirect fluorination).

An indirect fluorination implies the ^{18}F-radiolabeling of a small compound (also called prosthetic group) and then, a reaction with the target precursor. The ^{18}F-labeled prosthetic group is usually prepared through nucleophilic or electrophilic reactions, and purified before the following reaction by HPLC or solid-phase extraction (SPE) techniques. Almost every molecule containing protic functional groups such as an amino or hydroxyl group can be radiolabeled via prosthetic groups (Coenen, 2007). Examples of indirect fluorination widely used are the fluoroalkylation and click chemistry reactions.

3.7.3.1 2-[^{18}F]Fluoroethyl-tosylate as a fluoroalkylating agent

2-[^{18}F]Fluoroethyl-tosylate ([^{18}F]FEtOTs) is usually used to prepare PET tracers (Kniess *et al.*, 2015) since it is easy to prepare, presents low volatility, is stable and has a good balance between reactivity of the tosylate leaving group, chemo-selectivity and hydrolytic stability (Schoultz *et al.*, 2013; Kniess *et al.*, 2015). Moreover, [^{18}F]fluoroethyl and [^{11}C]methyl groups may be coupled to the same functional group, and therefore, the same precursor may be radiolabeled with ^{18}F or ^{11}C (Kniess *et al.*, 2015).

3.7.3.2 Click chemistry: Copper (I)-catalyzed azide-alkyne cycloaddition

Click chemistry has become a very attractive strategy in the design and synthesis of PET imaging radiotracers. Wang *et al.* (2012) reported that the high yields reached with this type of synthesis and the high stability of the products for *in vivo* imaging have stimulated its use in the field of molecular imaging. Click reactions occur in mild conditions and the final products are obtained with high yield, stereospecificity and are easily purified by non-chromatographic methods (Pretze *et al.*, 2013).

In particular, the copper (I)-catalyzed Huisgen 1,3-dipolar cycloaddition of azides with terminal alkynes is the most commonly used click reaction (Schirrmacher, 2007; Glaser and Robins, 2009; Wang *et al.*, 2012; Jacobson *et al.*, 2015). The copper (I)-catalyzed azide−alkyne cycloaddition yields 1,4-disubstituted 1,2,3-triazoles which are metabolically stable under physiological conditions (Glaser and Robins, 2009; Pretze *et al.*, 2013). The reaction shows an outstanding efficiency, regiospecificity and fast formation of the 1,4-disubstituted 1,2,3- triazoles at room temperature (Kettenbach *et al.*, 2014). In contrast, at high temperatures and without copper (I) catalyst, organic azides react with alkynes in

the Huisgen cycloaddition and produce both 1,4- and 1,5-disubstituted 1,2,3-triazoles regioisomers (Pretze *et al.*, 2013). The *in situ* reduction of copper (II)-salts by sodium ascorbate has been considered as the better pathway to prepare the copper (I) catalyst (Rostovtsev *et al.*, 2002). The reaction mechanism proposed by Worrell *et al.* (2013) involves two copper atoms: (1) formation of the copper-Π-complex, (2) copper-acetylide-Π-complex, (3) azide addition, (4) triazol copper derivative and (4) protolysis (Pretze *et al.*, 2013).

Although click reaction does not require a protecting group (Pretze *et al.*, 2013), azide and alkyne functional groups are not usually present in biomolecules; thus, their introduction into the target precursor involve additional synthetic steps before performing click reactions. The prosthetic group containing azide or alkyne functional group is ^{18}F-labeled and then, the radio-click reaction takes place. Finally, it is crucial the total removal of the copper from the final formulation containing the radiotracer because of its *in vivo* cytotoxicity (Kettenbach *et al.*, 2014).

3.7.4 ^{18}F-^{19}F isotope exchange using organotrifluoroborates approach

New PET tracers have been synthetized by the formation of B-^{18}F instead of the C-^{18}F linking. In particular, the one-step ^{18}F-labeling of organotrifluoroborates using the $AMBF_3$ motif is a very attractive approach recently developed by Perrin´s group to design and synthesize ^{18}F-tracers (Liu, Pourghiasian, Radtke*, et al.*, 2014). The $AMBF_3$ motif may be coupled to the biomolecule by a copper (I)-catalyzed alkyne-azide cycloaddition (click-reaction) and then the radiolabeling step is performed (Liu, Pourghiasian, Radtke*, et al.*, 2014; Liu, Z. *et al.*, 2015). The radiolabeling is conducted with no-carrier-added [^{18}F]F^- by a ^{18}F-^{19}F isotope exchange reaction in acidic aqueous media yielding ^{18}F-labeled products with *in vivo* stability, high molar activity and high radiochemical purity without requiring further HPLC purification (Liu, Pourghiasian, Radtke*, et al.*, 2014; Liu, Radtke*, et al.*, 2014; Liu, Z. *et al.*, 2015; Pourghiasian *et al.*, 2015). The overall synthesis takes around 30-40 minutes and the labeled product can be purified by SPE techniques.

In brief, the selected method for developing ^{18}F-tracers should produce target-specific and stable radiotracers using synthetic procedures that can be automatized for daily clinical routine.

3.8 AT_1R PET radioligands

Several AT_1R PET ligands have been radiolabeled with ^{11}C and ^{18}F (Figure 5), and evaluated in animals (mice, rats, dogs, baboon, pigs, rhesus macaques) and humans (Szabo *et al.*, 1998; Mathews *et al.*, 2004; Zober *et al.*, 2006; Hadizad *et al.*, 2009; Mathews e Szabo, 2010; Iimori *et al.*, 2011; Chopra, 2012; Noda *et al.*, 2012; Gulaldi *et al.*, 2013; Lortie *et al.*, 2013; Arksey *et al.*, 2014; Ismail *et al.*, 2015; Hachem *et al.*, 2016; Chen *et al.*, 2018).

Figure 5 – Reported AT_1R PET radioligands

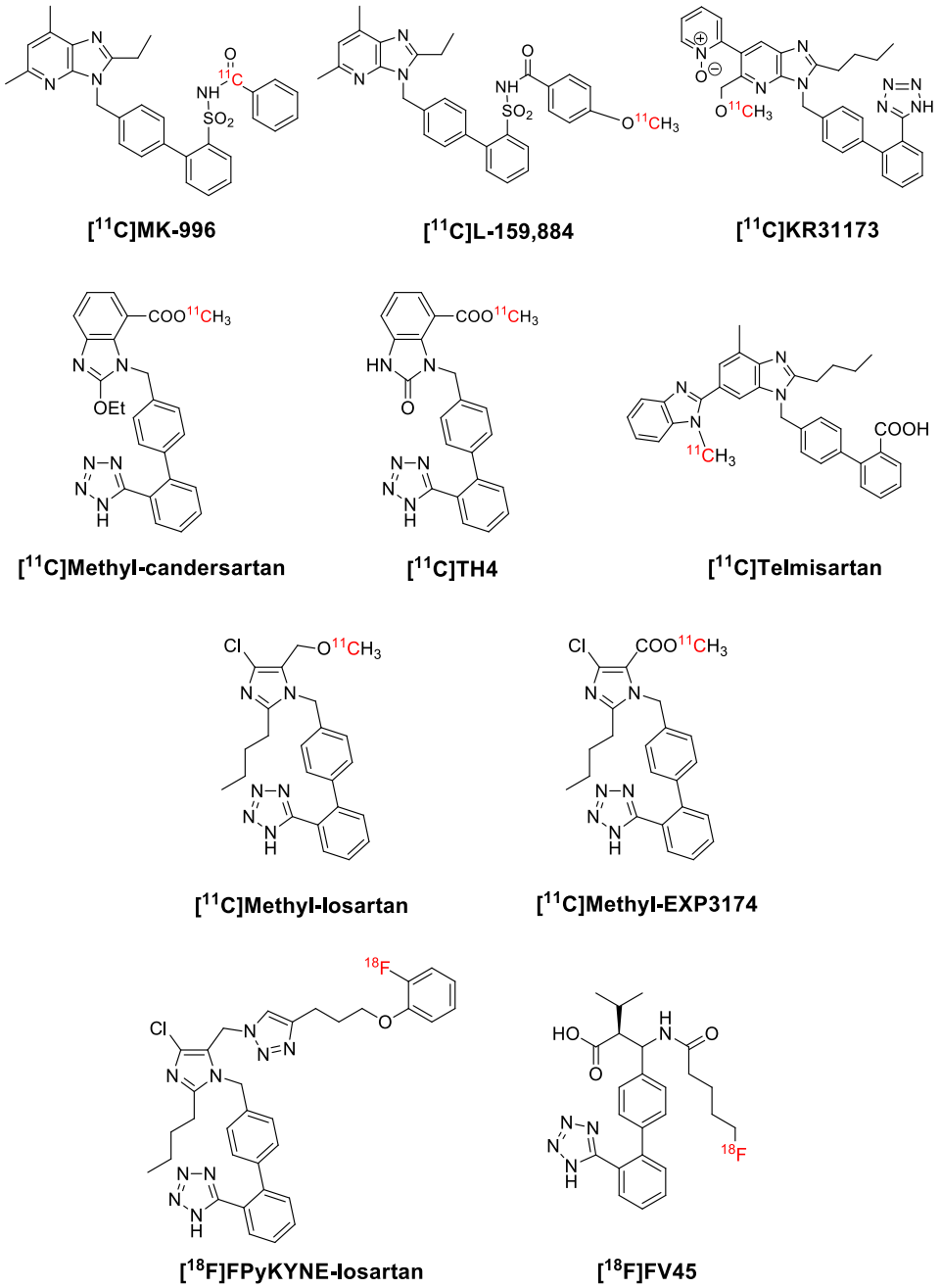

Source: thesis author.

3.8.1 AT_1R radioligands labeled with ^{11}C

According to the scientific literature, [^{11}C]MK-996 was the first ^{11}C-labeled ligand prepared to study AT_1R via PET imaging. [^{11}C]MK-996 was synthesized by N-benzoylation of the benzenesulfonamide precursor with [α-^{11}C]benzoyl chloride in 38 minutes using a two-step synthesis and two HPLC purifications (Mathews *et al.*, 1995). Despite the good imaging results in dogs, the radiosynthesis of [^{11}C]MK-996 was very laborious involving several steps of HPLC purification, and the authors later developed the radiotracer [^{11}C]L-159,884 that was prepared within 18 minutes with a higher molar activity using a single step synthesis followed by HPLC purification (Hamill *et al.*, 1996). [^{11}C]L-159,884 was synthesized via methylation of the phenol precursor with [^{11}C]methyl iodide (Hamill et al., 1996), and was successfully used in dogs to study AT_1R renal regulation *in vivo* (Szabo *et al.*, 2001; Zober *et al.*, 2008). However, *in vivo* studies in humans revealed that [^{11}C]L-159,884 is an unsuitable tracer because of its rapid metabolism (Mathews e Szabo, 2010). This same research group also developed [^{11}C]KR31173, which was prepared in 25 minutes through ^{11}C-methylation reaction, followed by acidic deprotection and HPLC purification (Mathews *et al.*, 2004). PET imaging studies showed that [^{11}C]KR31173 binds specifically to renal AT_1R in mice, dogs, baboon (Zober *et al.*, 2006), and to myocardial AT_1R in pigs (Fukushima *et al.*, 2012). The first study in four healthy volunteers with [^{11}C]KR31173 showed detectable and specific myocardial tracer retention, although at a lower level than in pigs (Fukushima *et al.*, 2012). Interestingly, myocardial AT_1R imaging with [^{11}C]KR31173 in patients with hypertrophic obstructive cardiomyopathy showed an abnormal increase of AT_1R expression in hypertrophic regions compared to healthy volunteers (Valenta *et al.*, 2017), demonstrating the potential of this PET tracer for the diagnosis of myocardial AT_1R in diseased conditions.

AT_1R PET tracers were also developed for brain imaging studies. [^{11}C]methyl-candesartan and its derivative [^{11}C]TH4 were synthetized in approximately 30 minutes by the ^{11}C-methylation of tetrazole-protected candesartan followed by acidic hydrolysis and HPLC purification (Hadizad *et al.*, 2009). *Ex-vivo* biodistribution studies in rats revealed that both radioligands displayed a high uptake in the liver and kidneys; however, none of them crossed

the blood-brain barrier (Hadizad *et al.*, 2009). Nonetheless, PET imaging also showed *in vivo* selective binding of [^{11}C]methyl-candesartan to AT_1R in rat kidneys (Lortie *et al.*, 2013).

[^{11}C]Telmisartan, another AT_1R PET tracer, was prepared by the ^{11}C-methylation of the precursor N-desmethyl telmisartan methyl ester, basic hydrolysis and HPLC purification with an overall synthesis time of 32-36 minutes (Iimori *et al.*, 2011). The biodistribution of [^{11}C]telmisartan was analyzed by PET imaging in conscious rhesus macaques to investigate the brain concentration and localization of telmisartan. This tracer showed little brain penetration but slow brain clearance compared to the plasma clearance (Noda *et al.*, 2012). According to recent literature, [^{11}C]telmisartan is the only tracer described that is capable to cross the blood-brain barrier, thus allowing AT_1R brain imaging.

In addition, other ^{11}C-labeled Angiotensin II Receptor Blockers such as [^{11}C]methyl-losartan and [^{11}C]methyl-EXP3174 were synthetized and evaluated as renal AT_1R PET tracers in rats. EXP3174 is the active carboxylic acid metabolite of losartan, which is formed from losartan oxidation by hepatic cytochromes P450 (Yasar U *et al.*, 2001). Both radioligands were prepared by the ^{11}C-methylation of tetrazole-protected losartan and tetrazole-protected EXP3174, respectively, followed by acid removal and HPLC purification, with a total preparation time of approximately 30 minutes (Hadizad *et al.*, 2011; Ismail *et al.*, 2015). Although both radioligands bound selectively to renal AT_1R, PET images using [^{11}C]methyl-EXP3174 displayed a high tissue-to-blood ratio signal in the rat kidney (Ismail *et al.*, 2015).

3.8.2 AT_1R radioligands labeled with ^{18}F

[^{18}F]FPyKYNE-losartan was the first AT_1R PET ligand labeled with ^{18}F. This radioligand was synthetized using a copper (I)-catalyzed click reaction between the correspondent ^{18}F-labeled terminal alkyne and azide-modified tetrazole-protected losartan, and followed by acidic deprotection and HPLC purification (Arksey *et al.*, 2014). *In vitro* saturation binding studies showed that [^{18}F]FPyKYNE-losartan bound with high affinity to the renal cortex AT_1R (with a dissociation constant of 49.4 nM and maximal binding of 348±112 fmol/mm^2) (Hachem *et al.*, 2016). Additionally, PET imaging of rats and pigs with [^{18}F]FPyKYNE-losartan exhibited a high tissue contrast in kidneys with slow

clearance and binding selectivity for renal AT_1R (Arksey *et al.*, 2014; Hachem *et al.*, 2016). However, the tracer antagonized the ANG II pressor effect with 4-fold potency reduction relative to losartan (Hachem *et al.*, 2016).

[^{18}F]F-Valsartan (FV45) was the last PET AT_1R ligand recently reported. [^{18}F]FV45 was prepared in 120 minutes by one-pot nucleophilic ^{18}F-fluorination and followed by deprotection procedure and HPLC purification (Chen *et al.*, 2018). Competitive binding assays revealed similar binding affinity between the cold FV45 (14.6 ± 10.0 nM) and the antagonist valsartan (11.8 ± 3.4 nM); the μPET/CT imaging in control rats showed a fast clearance and specific kidney uptake which was reduce after pretreatment with the AT_1R blocker valsartan (Chen *et al.*, 2018). Although the chemical modifications are minor in comparison with the chemical structure of valsartan, more than ten synthetic intermediaries are needed to synthetize the precursor of [^{18}F]FV45, which makes its use in AT_1R imaging not attractive.

In conclusion, most of the PET AT_1R radioligands described so far were radiolabeled with ^{11}C, which is considered a disadvantage for PET imaging when compared to ^{18}F. Moreover, all described radioligands were characterized for their affinity to renal AT_1R and showed binding selectivity to AT_1R *in vivo*. However, no PET imaging tracer with affinity for AT_1R has been considered for cancer imaging so far. Indeed, to the best of our knowledge this thesis is the first report on ^{18}F-labeled AT_1R ligands for PET imaging of tumors.

3.9 Final considerations

The renin angiotensin system seems to have a powerful connection with tumor development and cancer progression. Expression of angiotensin II type 1 receptor has been reported in several types of human cancer cells and tumor tissues from patients with cancer. AT_1R signaling in tumors can lead to proliferation, migration, invasion, angiogenesis, tumor growth and survival of tumor cells through the activation of kinases, transcription factors, matrix metalloproteinases, growth factors, and suppression of caspases and p53. Losartan, a selective AT_1R blocker, was previously radiolabeled to detect and quantify AT_1R in kidneys using PET imaging. Hence, PET/CT imaging with ^{18}F-labeled losartan analogs could be a promising strategy for *in vivo* and non-invasive diagnose of AT_1R-positive tumors. Both [^{18}F]fluoroethylation of losartan or $AMBF_3$

^{18}F-labeling approach may represent promising synthetic routes for preparing new ^{18}F-labeled losartan analogs.

4 MATERIALS AND METHODS

4.1 Chemicals, instrumentation and general methods

All chemicals and solvents were purchased with analytical grade from Ontario Chemicals (Canada), Sigma Aldrich (Brazil, Canada) and Fisher Scientific (EUA), and used without further purification. The cold compound FEtLos was synthesized at the School of Pharmaceutical Sciences of Ribeirão Preto, University of São Paulo, Ribeirão Preto, Brazil; whereas the cold $AMBF_3$Los was synthetized at the BC Cancer Research Centre, Vancouver, British Columbia, Canada. The fluoroalkylating agent 2-fluoroethyl tosylate was prepared according to the literature (Bernard-Gauthier *et al.*, 2015). High Resolution Mass Spectrometry (HRMS) and Nuclear Magnetic Resonance experiments were recorded on a Bruker Daltonics micrOTOF-Q II ESI-Qq-TOF spectrometer and Bruker Avance DRX 300, DPX 400, DPX 500 equipments, respectively, in Brazil. Chemical shifts (δ) were reported in parts per million (ppm) relative to an internal tetramethylsilane standard. Coupling constants (J) were reported in Hertz (Hz). Multiplicity was defined by singlet (s), doublet (d), triplet (t), quintet (q), sextet (sx), septet (sept), doublet of doublets (dd), or multiplet (m). Samples were dissolved in chloroform-d ($CDCl_3$), dimethyl sulfoxide-d6 (DMSO) or acetonitrile-d3 (CD_3CN). Only the $AMBF_3$-alkynyl (**6**) and the synthetic intermediate (**5**) were analyzed on a 5600 mass spectrometer (AB/Sciex) in Canada.

[^{18}F]$AMBF_3$Los was prepared using manipulators to handle high ^{18}F activity. [^{18}F]F^- was produced by the $^{18}O(p,n)^{18}F$ reaction using $H_2{}^{18}O$ target in an Advanced Cyclotron Systems Inc. (Richmond, Canada) TR19 cyclotron. µ-QMA and Sep-Pak C18 light cartridges were obtained from ORTG Inc. (Oakdale, TN), and Waters (Mississauga, Canada) respectively. A Capintec (Ramsey, NJ) CRC®-25R/W dose calibrator was used to measure the activity of fluorine-18. Agilent (Santa Clara, CA, USA) HPLC systems were used to purify the cold $AMBF_3$Los and the azide-losartan precursor, and to perform the purification

and quality control of [^{18}F]AMBF$_3$Los. HPLC systems were equipped with a model 1200 UV absorbance detector, a Bioscan (Washington DC, USA) NaI scintillation detector, and a model 1200 quaternary pump. The radio-detector was connected to a Bioscan B-FC-1000 flow-count system, and the output from the Bioscan flow-count system was fed into an Agilent 35900E Interface which converted the analog signal to digital signal (Gonçalves Nunes *et al.*, 2018). The Agilent ChemStation software was used to control the Agilent HPLC systems. The methods used for HPLC purification and quality control were the following ones. Method A: Phenomenex Luna C18 semi-preparative column (5 µ, 250 x 10 mm), solvent A: 0.1% trifluoroacetic acid (TFA) water, solvent B: MeCN, 40:60 B / A, 0-10 min, 40-100% B, 11-15 min, 100% B, 15-25 min, 4 mL/min, 254 nm. Method B: Phenomenex Luna C18 semi-preparative column (5 µ, 250 x 10 mm), solvent A: Milli-Q water, solvent B: MeCN, 20:80 B / A, 0-10 min, 40:60 B / A, 11-25 min, 4 mL/min, 254 nm. Method C: Phenomenex Luna C18 semi-preparative column (5 µ, 250 x 10 mm), 60:40, 0.1% TFA water / 0.1% TFA acetonitrile, 4.5 mL/min. Method D: Phenomenex analytical Luna C18 column (5 µ, 250 x 4.6 mm), solvent A: 0.1% TFA water, solvent B: 0.1% TFA MeCN, 60:40, A / B, 2 mL/min. The hot ligand [^{125}I]-(Sar^1,Ile^8)-Angiotensin II (81.4 TBq/mmol) and the membranes expressing the human AT$_1$R from CHO-K1 cells were purchased from Perkin Elmer (USA) for the *in vitro* competition binding assays. Balb/c mouse plasma was purchased from Innovative Research. A WIZARD 2480 gamma counter (PerkinElmer) was used to count the radioactivity of the samples from *in vitro* binding assays and *ex vivo* biodistribution studies. PET imaging experiments were executed using a Siemens (Malvern, PA) Inveon µPET/CT scanner. A Typhoon FLA 9500 scanner (GE Healthcare) was used for autoradiography studies.

The manual syntheses of [^{18}F]FEtOTs, [^{18}F]FEtLos and [^{18}F]AMBF$_3$Los were performed at the Radiopharmacy Center, IPEN, SP, Brazil. No carrier-added [^{18}F]F$^-$ was produced by the ^{18}O (p,n) ^{18}F nuclear reaction in a 18-MeV cyclotron (IBA, Belgium) using H$_2{}^{18}$O target. Sep-Pak Light QMA cartridges (Waters, Brazil) were pre-conditioned with 10 mL of 0.5-M K_2CO_3, followed by 20 mL of Milli-Q water and purged with air. Sep-Pak C18 Plus cartridges were obtained from Waters (Brazil) and pre-conditioned with 5 mL of ethanol and 10 mL of Milli-Q water. µ-QMA cartridges were always flushed with 3-mL brine and 6-mL Milli-Q water before [^{18}F]F$^-$ trapping. Sep-Pak C18 light cartridges (Waters, Brazil) were

preconditioned with 3-mL ethanol and 3-mL of Milli-Q water. Radioactivity measurement of fluorine-18 was performed using a Capintec radioisotope dose calibrator (CRC-15R, New Jersey, USA). Agilent HPLC system (USA) was used for the purifications and quality control of the ^{18}F-labeled compounds. HPLC system are equipped with a model 1260 quaternary pump, a model 1260 UV absorbance detector, and a radioactivity detector from Raytest (Germany). The Agilent ChemStation software was used to operate the Agilent HPLC systems. The methods used for HPLC purification and quality control are the following ones. Method E: Agilent analytical Zorbax Eclipse Plus C18 column (5 µ, 250 x 4.6 mm), solvent A: 0.1% TFA water, solvent B: MeCN, 55:45 A / B, 1 mL/min, 254 nm. Method F: Phenomenex Nucleosil C18 semi-preparative column (5 µ, 250 x 10 mm), solvent A: 0.1% TFA water; solvent B: MeCN, 50:50 A / B, 3 mL/min, 254 nm. Method G: Phenomenex Nucleosil C18 semi-preparative column (5 µ, 250 x 10 mm), solvent A: 0.1% TFA water, solvent B: MeCN, 55:45 A / B, 3 mL/min, 254 nm. Method H: Agilent analytical Zorbax Eclipse Plus C18 column (5 µ, 250 x 4.6 mm), solvent A: 0.1% TFA water, solvent B: MeCN, 0-15 min, 55:45 A / B, 15-20 min, 45-100% B, 20-30 min, 100% B, 1 mL/min, 254 nm. Method I: Agilent analytical Zorbax Eclipse Plus C18 column (5 µ, 250 x 4.6 mm), solvent A: 0.1% TFA water, solvent B: MeCN, 0-30 min, 0-100% B, 1 mL/min, 254 nm. The radioactivity of the samples from *in vitro* binding assays and *ex vivo* biodistribution studies were counted with a Cobra II gamma counter (Packard). The hypoxic chamber H35 hypoxystation (Don Whitley Scientific Ltd, Shipley) was used to simulate hypoxic conditions. PET imaging was performed using an Albira µPET/SPECT/CT imaging system (Bruker Corporation, Spain).

4.2 Chemistry

4.2.1 Synthesis of the cold FEtLos

The cold FEtLos (**1a**) was prepared following two synthetic routes represented by scheme 1.

Scheme 1 – The synthesis of the cold FEtLos (1a) by alkylation of losartan potassium commercially available provided the regioisomers 1a and 2a (**A**); while alkylation of compound 3 followed by trityl removal only delivered the derivative 1a (**B**).

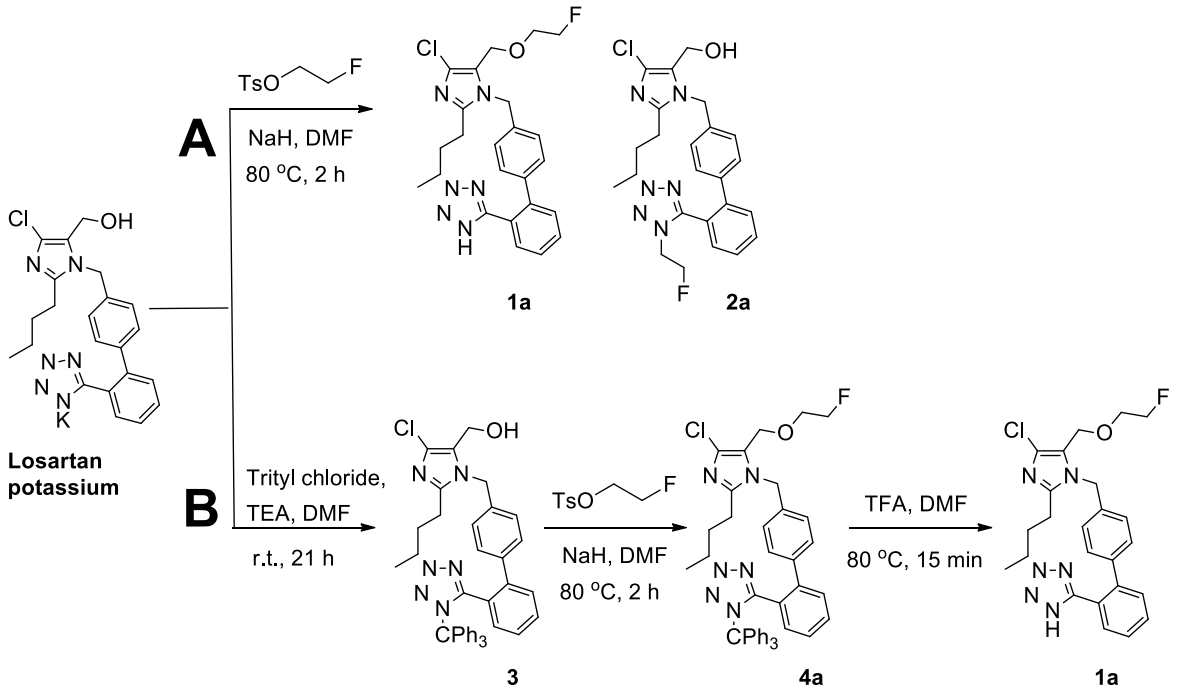

Source: thesis author.

*2-butyl-4-chloro-5-(hydroxymethyl)-1-[(2´-(1H-(1-(triphenylmethyl))tetrazol-5-yl) biphenyl-4-yl)methyl]-1H-imidazole (**3**)*

Compound **3** was synthetized according to the literature (Hadizad *et al.*, 2011). Trityl chloride (1.7 g, 6.1 mmol) was added to an ice-cooled solution of losartan potassium (2 g, 4.3 mmol) and triethylamine (0.86 mL, 0.62 g, 6.1 mmol) in anhydrous DMF (10 mL). The reaction was set at 0 ^{o}C for 1 h under stirring and then, at room temperature (22 ^{o}C) overnight (21 hrs). Thin layer chromatography (TLC) was used to monitor the completion of the reaction (silica gel, retention factor (Rf) of **3** = 0.5 using 50:50 hexane / ethyl acetate, and Rf of **3** = 0.8 using 30:70 hexane / ethyl acetate), and then, the reaction was quenched and the product extracted with ethyl acetate and brine. The organic layer was dried over magnesium sulfate ($MgSO_4$), filtered and the solvent was evaporated. The residue was purified by flash column chromatography (silica gel, hexane / ethyl acetate, 50:50) to obtain **3**, that was then analyzed by ^{1}H NMR (proton NMR), (^{1}H,^{1}H)-COSY (Correlation Spectroscopy), and HRMS.

*2-butyl-4-chloro-5-(2-fluoroethoxy)methyl-1-[(2´-(1H-(1-(triphenylmethyl))tetrazol-5-yl) biphenyl-4-yl)methyl]-1H-imidazole (**4a**)*

2-Fluoroethyl-tosylate (28 µL, 37 mg, 0.17 mmol) was added dropwise to an ice-cooled solution of **3** (50 mg, 0.11 mmol) and sodium hydride (NaH, 3.6 mg, 0.15 mmol) in anhydrous DMF (400 µL) under stirring and argon atmosphere. The reaction mixture was stirred at 0 ^{o}C for 30 minutes, and then, at 80 ^{o}C for 2 hrs (the reaction color changed from transparent to yellow). The formation of the product was monitored by TLC (silica gel, toluene / ethyl acetate, 90:10, Rf = 0.5). Afterwards, the reaction was quenched by dripping deionized water. Crude product was extracted by ethyl acetate (3 times) using brine as the aqueous phase. The organic layers were pool together, dried over $MgSO_4$, filtered and the solvent was evaporated. The residue was purified by flash column chromatography (silica gel, toluene / ethyl acetate, 90:10, Rf = 0.5) to obtain **4a**, which was then analyzed by ^{1}H NMR, ^{13}C NMR (Carbon NMR), ^{19}F NMR (Fluorine NMR), (^{1}H,^{1}H)-COSY and HRMS.

*2-butyl-4-chloro-5-(2-fluoroethoxy)methyl-1-[(2´-(1H-tetrazol-5-yl)biphenyl-4-yl) methyl]-1H-imidazole (**1a**)*

According to the scheme 1A, a solution of losartan potassium (100 mg, 0.22 mmol) in anhydrous DMF (500 µL) was added to an ice-cooled mixture of NaH (6 mg, 0.22 mmol) and anhydrous DMF (500 µL) under stirring and argon atmosphere. Next, a solution of 2-fluoroethyl-tosylate (40.4 µL, 0.24 mmol) in anhydrous DMF (400 µL) was dropwise added into the solution previously prepared. The reaction mixture was stirred at room temperature for 30 minutes, and then, at 80 ^{o}C for two hours (orange in color). The progress of the reaction was monitored by TLC (silica gel, Rf of **1a** = 0.31 using 50:50 hexane / ethyl acetate, and Rf of **1a** = 0.68 using 30:70 hexane / ethyl acetate). The reaction was quenched, and the solvent was evaporated using a rotary evaporator with vertical dry-ice condenser. The residue was purified by flash column chromatography (silica gel, hexane / ethyl acetate, 50:50 - 30:70) to obtain **1a.**

Following scheme 1B, a solution of DMF-TFA 40:1 (64 µL) was added to the solution of **4a** (8 mg, 11.3 µmol) diluted in DMF. After heating the mixture at 80 ^{o}C for 15 min, the reaction was monitored by TLC. Then, the crude product was purified by a semipreparative HPLC (Shimadzu Corporation, Japan) with the

following conditions: Nucleosil C18 column 250 x 10 mm 5 µm, solvent A: 0.1 % TFA water; solvent B: MeCN; 0-40 min, 10-100 % A; 3 mL / min; 254 nm.

The compound **1a** was analyzed by ^{1}H NMR, ^{13}C NMR, ^{19}F NMR, (^{1}H,^{13}C)-HMQC (Heteronuclear Multiple-Quantum Correlation), (^{1}H,^{13}C)-HMBC (Heteronuclear Multiple-Bond Correlation), and HRMS.

*2-butyl-4-chloro-5-(hydroxymethyl)-1-[(2´-(1H-(1-(2-fluoroethyl))tetrazol-5-yl)biphenyl-4-yl)methyl]-1H-imidazole (**2a**)*

Compound **2a** was synthetized following the scheme 1A, as a side-product during the synthesis of **1a.** The Rf values of **2a** on TLC plate (silica gel) were 0.28 using 50:50 hexane / ethyl acetate and 0.59 using 30:70 of hexane / ethyl acetate, during the assessment of the progress of the reaction to obtain **1a**. The starting material losartan always showed a lesser Rf than **1a** and **2a**. The compound **2a** was also purified by flash column chromatography (silica gel, hexane / ethyl acetate, 50:50 - 30:70). ^{1}H NMR, ^{19}F NMR, (^{1}H,^{13}C)-HMBC and HRMS were performed to characterize **2a**.

4.2.2 Synthesis of the cold $AMBF_3Los$

The cold $AMBF_3Los$ (**9a**) was prepared following the synthetic route represented by scheme 2.

Scheme 2 – Synthesis of the cold $AMBF_3Los$ (9a) by click chemistry using a copper (I)-catalyzed azide - alkyne cycloaddition

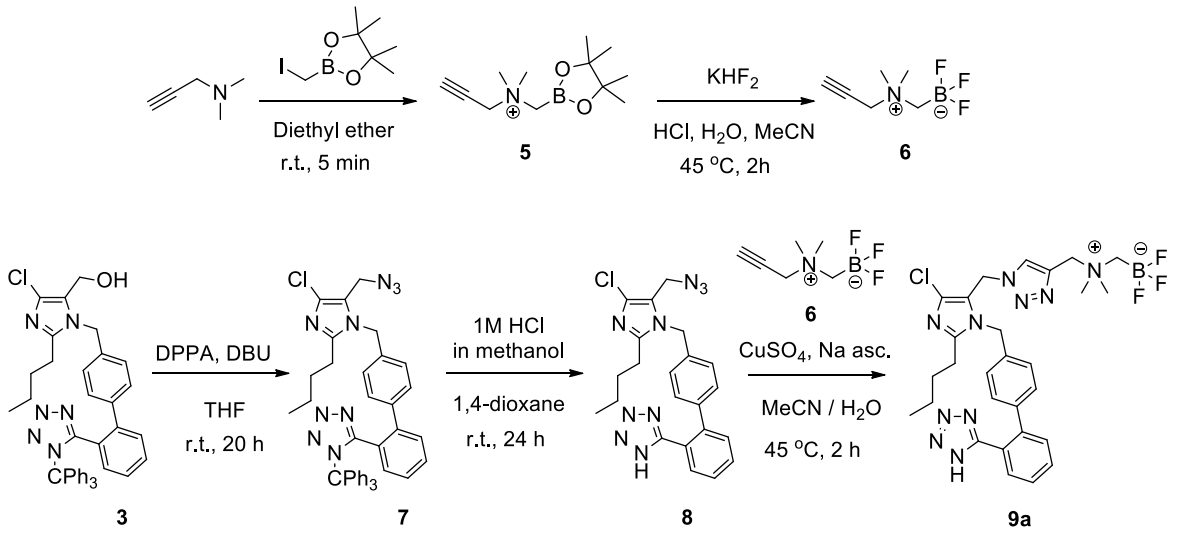

Source: thesis author.

*N-propargyl-N,N-dimethylammonio-methylboronyl pinacolate (**5**)*

Iodomethyl-pinacol boronate (200 µL, 1.1mmol) was dropwise added into the solution of N,N-dimethylpropargylamine (129 µL, 1.2 mmol) in anhydrous diethyl ether (4 mL) as previously described by Liu and coworkers (Liu, Pourghiasian, Radtke*, et al.*, 2014; Liu, Z. *et al.*, 2015). The mixture was stirred for 5 min at room temperature. The formed precipitate was filtered, washed with diethyl ether and dried under high vacuum to obtain the compound **5**. Compound **5** was analyzed by MS.

*N-propargyl-N,N-dimethyl-ammoniomethyl-trifluoroborate (**6**)*

Compound **6** ($AMBF_3$-alkynyl) was prepared according to Liu and coworkers (Liu, Pourghiasian, Radtke*, et al.*, 2014; Liu, Z. *et al.*, 2015). Hydrochloric acid (4M HCl) (6 eq.) and 3M potassium hydrogenfluoride (KHF_2) (5 eq.) were added to the solution of **5** (200 mg, 0.9 mmol) in MeCN (1.3 mL). The reaction was set at 45 ^{o}C for two hours, and then quenched with a concentrate ammonium hydroxide solution (NH_4OH, 60 µL) until pH reached ~7 on a pH paper. The top layer (MeCN) was extracted, the solvent was dried down using a rotary evaporator, and the residue was further dried using a vacuum line (yellowish oil) overnight. Subsequently, the crude product was dissolved in acetone to crash the salt; the salt was filtered out, and the collected acetone mixture was dried down on a rotary evaporator. The residue was then crashed out using diethyl ether, and the solid product was filtered. The product was further purified by a silica column using acetone as a mobile phase. Compound **6** was analyzed by MS.

*2-butyl-4-chloro-5-(azidomethyl)-1-[(2´-(1H-(1-(triphenylmethyl))tetrazol-5-yl)biphenyl-4-yl)methyl]-1H-imidazole (**7**)*

Compound **7** was prepared as previously described (Arksey *et al.*, 2014). 1,8-Diazabicyclo(5.4.0)undec-7-ene (DBU, 250 µL, 1.7 mmol) and diphenyl phosphoryl azide (DPPA, 360 µL, 1.7 mmol) were sequentially added to a solution of **3** (1 g, 1.5 mmol) in anhydrous tetrahydrofuran (THF, 10 mL) under nitrogen atmosphere. After stirring overnight at room temperature (20 hrs), the progress of the reaction was monitored by TLC (silica gel, Rf of **7** = 0.7 using 70:30 hexane / ethyl acetate). The reaction was quenched, extracted with ethyl acetate and brine, dried over $MgSO_4$, filtered and the solvent was evaporated. Compound **7** was

purified by flash column chromatography (silica gel, hexane / ethyl acetate, 95:5 - 70:30), and analyzed by HRMS and ^{1}H NMR.

*2-butyl-4-chloro-5-(azidomethyl)-1-[(2´-(1H- tetrazol-5-yl)biphenyl-4-yl)methyl]-1H-imidazole (**8**)*

Deprotection of the tetrazole moiety to obtain the compound **8** was performed according to the procedure reported by Hadizad and coworkers for the synthesis of [^{11}C]methyl-losartan (Hadizad *et al.*, 2011). A solution of 1M HCl in methanol (1.7 mL) was added to a solution of **7** (15.7 mg, 22.8 µmol) in 1,4-dioxane (1.4 mL). After stirring at room temperature (22 ^{o}C) for 24 hrs, the reaction was completed and monitored by HPLC (method A: retention time of 16 min). The reaction was quenched, extracted with ethyl acetate and brine, dried over $MgSO_4$, filtered and the solvent was evaporated. The residue was dissolved in MeCN and purified by HPLC. The product was also purified by flash column chromatography (silica gel, hexane / ethyl acetate, 95:5 - 30:70). The collected fractions were pooled together, concentrated and the product was freeze-dried. Compound **8** was analyzed by HRMS, ^{1}H NMR and ^{13}C NMR.

*2-butyl-4-chloro-5-[((1H-1,2,3-triazol-4-yl)-(N,N-dimethyl-ammoniomethyl-trifluoroborate)methyl)methyl]-1-[(2´-(1H-tetrazol-5-yl) biphenyl-4-yl)methyl]-1H-imidazole (**9a**)*

Finally, the compound **9a** was synthetized using the $AMBF_3$ approach developed by Perrin´s group (Liu, Z. *et al.*, 2015). Copper (II) sulfate ($CuSO_4$, 1M, 15 uL), sodium ascorbate (Na asc., 1M, 40 uL), 5% NH_4OH (vol/vol in 1:1 MeCN / H_2O, 150 uL), compound **6** (6.6 mg, 40 µmol, in 300 uL MeCN / H_2O 1:1) and compound **8** (4.8 mg, 10.7 µmol, in 700 uL of MeCN), were sequentially added to a 5-mL eppendorf. After stirring at 45 ^{o}C for 2 hrs, the product was purified by HPLC (method B: retention time of 15.2 min). The collected fractions were frozen and the product was freeze-dried. The purified **9a** was diluted in acetone and stored in aliquots of ~25 or 100 nmol for radiolabeling; the solvent was blow-dried. Compound **9a** was analyzed by ^{1}H NMR, ^{13}C NMR ^{19}F NMR, (^{1}H,^{13}C)-HMQC, (^{1}H,^{13}C)-HMBC and HRMS.

4.3 Radiochemistry

4.3.1 Radiosynthesis of [^{18}F]FEtOTs

4.3.1.1 Obtention and Azeotropic drying of [^{18}F]F$^-$

The irradiated water containing the [^{18}F]F$^-$ was loaded onto a QMA cartridge (130 mg, carbonate form), and [^{18}F]F$^-$ was eluted with 1 mL of K_2CO_3 (2 mg, 14 µmol) / K_{222} (11 mg, 29 µmol) mixture in 2:8 Milli-Q water / MeCN (Schoultz *et al.*, 2013). [K^+/ K_{222}]/[^{18}F]F$^-$/CO_3^{2-} complex was dried by azeotropic distillation at 100 ^{o}C and nitrogen atmosphere with a sequential addition of MeCN (1 mL, 3 times).

4.3.1.2 General protocol to prepare the [^{18}F]FEtOTs

[^{18}F]FEtOTs (scheme 3) was prepared according to previous protocols (Schirrmacher *et al.*, 2002; Schoultz *et al.*, 2013). The ethylene glycol bistosylate precursor (8 mg) was dissolved in 1 mL of anhydrous MeCN and added to the vial containing the [K^+/K_{222}]/[^{18}F]F$^-$/CO_3^{2-} dried complex. The reaction was set in sealed and non-sealed vials, at different labeling temperatures and reaction times, and different amounts of K_2CO_3 were used for [^{18}F]F$^-$ elution from the QMA cartridge. After cooling down the reaction vial, an aliquot of the crude mixture was analyzed by HPLC with the method E (retention time of 8.16 ± 0.04 min). Next, the crude mixture was injected onto a semi-preparative HPLC system to purify the product (method F: retention time of 14 min). The collected fraction of [^{18}F]FEtOTs was diluted and loaded onto a Sep-Pak C18 Plus cartridge. The loaded cartridge was washed with Milli-Q water (10 mL) and heated at 50 ^{o}C for 10 min while flushing with nitrogen (Schoultz *et al.*, 2013). Afterwards, [^{18}F]FEtOTs was eluted with DMF (1 mL). An aliquot of the final formulation was analyzed by HPLC to confirm the identity of the labeled compound by comparing the radiochromatogram of the cold compound on the 254-nm UV profile. The chemical and radiochemical purity were also evaluated.

Scheme 3 – General scheme to prepare the [^{18}F]FEtOTs following a bimolecular nucleophilic ^{18}F-substitution-SN2-reaction.

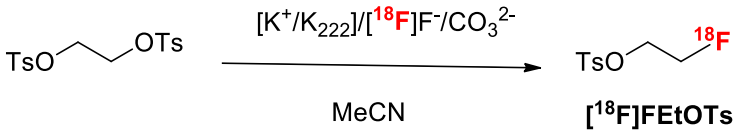

Source: thesis author.

4.3.1.3 Optimization of the labeling temperature and reaction time during the radiosynthesis of [^{18}F]FEtOTs

The influence of the labeling temperature [T(^{o}C)] and the reaction time [t(min)] were evaluated using a rotatable central composite design (RCCD) with a two-level full factorial core for two factors (2^2), analyzing just the crude mixture. All reactions were performed in sealed vials. The amount of K_2CO_3 was fixed at 2 mg because it is the most used amount according to the literature (Schirrmacher *et al.*, 2002; Tietze *et al.*, 2006; Zheng *et al.*, 2008; Prabhakaran *et al.*, 2012; Sun *et al.*, 2012; Majo *et al.*, 2013; Schoultz *et al.*, 2013). The activity of [^{18}F]F$^-$ for radiolabeling was 1.6 ± 0.3 GBq. The minimum (70 ^{o}C and 3 min) and maximum (130 ^{o}C and 15 min) levels of T(^{o}C) and t(min) were also chosen according to the literature (Kniess *et al.*, 2015). Ten different combinations of T(^{o}C) and t(min) were evaluated. The RCCD matrix comprised a 2^2 factorial core, center points and additional runs including the so-called star points. The experiment corresponding to the center point was repeated three times to calculate the experimental standard deviation. The star points were calculated using an axial distance of 1.42, based on previous reports (Domínguez Catasús *et al.*, 2014). The response or dependent variable was the percentage of the integrated signal of the ^{18}F-labeled side-product at ~5 min ([^{18}F]FSP5 (%)) on the HPLC profile (method E) of the crude mixture.

4.3.2 Radiosynthesis of [^{18}F]FEtLos

The hot compound [^{18}F]FEtLos (**1b**) was prepared following the two synthetic routes used for the synthesis of the cold compound, represented by scheme 4.

Scheme 4 – Radiosynthesis of the [^{18}F]FEtLos (1b) by [^{18}F]fluoroalkylation of losartan potassium commercially available, which provided the regioisomers 1b and 2b (**A**); while [^{18}F]fluoroalkylation of compound 3 followed by trityl removal only delivered the derivative 1a (**B**).

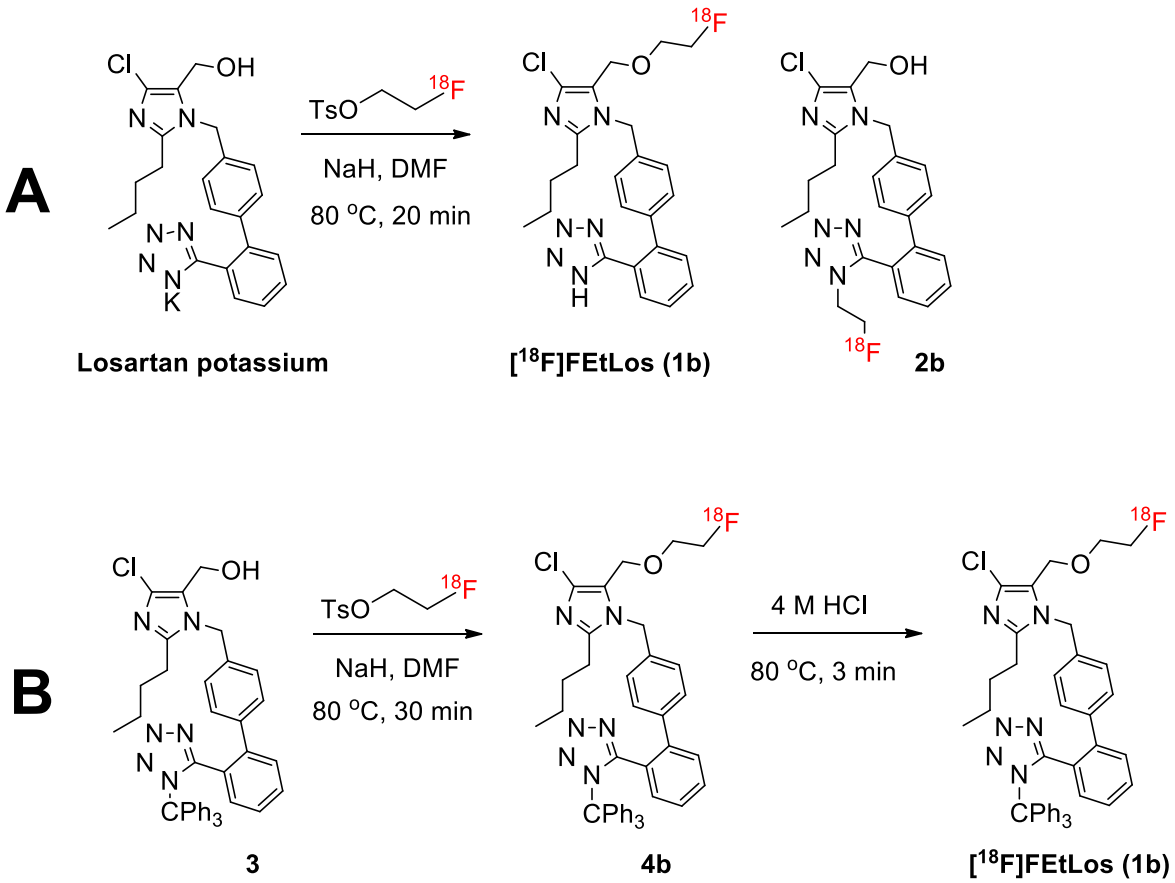

Source: thesis author.

Losartan potassium as precursor of the radiosynthesis (Scheme 4A)

A solution of [^{18}F]FEtOTs (200 ± 70 MBq = 5 ± 2 mCi) in DMF (800 µl) was added dropwise to a vial containing losartan potassium (1 mg) and NaH (8 eq.) in DMF (30 µL). The reaction vial was heated at 80 ^{o}C for 20 min under stirring and nitrogen atmosphere. The labeling reaction was monitored by analytical HPLC (method E). The crude mixture was diluted with 5:5 water / MeCN solution and injected onto a semi-preparative HPLC system to purify **1b** (method G: retention time of 21 min). The collected fraction was diluted with Milli-Q water and loaded onto a Sep-Pak C18 Plus cartridge. Finally, **1b** was eluted with MeCN (1 mL). The final formulation was concentrated at 100 ^{o}C and reconstituted with saline for *in vivo* studies.

*Compound **3** as precursor of the radiosynthesis (Scheme 4B)*

[^{18}F]fluoroethylation of **3** was performed according to the described procedure for obtention of [^{11}C]methyl-losartan (Hadizad *et al.*, 2011). A solution of [^{18}F]FEtOTs (150 MBq = 4 mCi) in DMF (170 µL) was added dropwise to a vial containing **3** (5 mg) and NaH (8 eq.) in DMF (30 µL). The reaction was allowed to proceed for 30 min at 80 ^{o}C under stirring and nitrogen atmosphere. After cooling the reaction vial in dry ice for one min, tetrazole moiety was deprotected by adding 200 µL of 4 M hydrochloric acid (HCl) and heating at 80 ^{o}C for three minutes. The reaction vial was cooled in dry ice for two minutes followed by addition of Milli-Q water (300 µL) and HPLC purification (method G). Each radiosynthesis' step was monitored by analytical HPLC (method H: 7.9 ± 0.1 min).

4.3.3 Radiosynthesis of [^{18}F]AMBF$_3$Los

The hot compound [^{18}F]AMBF$_3$Los (**9b**) was prepared following the simple synthetic route represented by scheme 5.

Scheme 5 – Radiosynthesis of the [^{18}F]AMBF$_3$Los (**9b**) by ^{18}F-^{19}F isotopic exchange (IE).

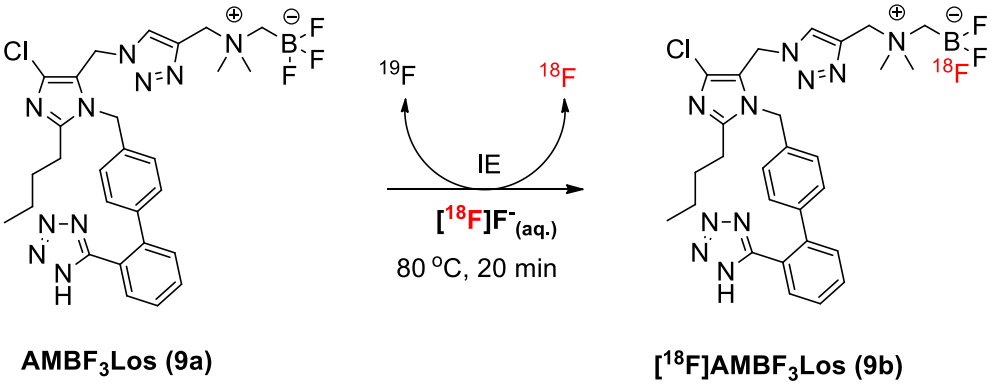

AMBF$_3$Los (9a) **[^{18}F]AMBF$_3$Los (9b)**

Source: thesis author.

Using high activities of [^{18}F]F$^-$

The compound **9a** (100 nmol) was resuspended in a mixture of DMF (15 µL), aqueous pyridazine-HCl buffer (1.0 M, pH 2.0–2.5, 15 µL), and aqueous solution of KHF_2 (7.5 mM, 1 µL). No carrier-added [^{18}F]F$^-$ (61 ± 23 GBq; 1.6 ± 0.6 Ci) was trapped on a µ-QMA cartridge (9 mg, QMA, chloride form). The [^{18}F]F$^-$ was eluted with 70-µL isotonic saline into the polypropylene Falcon tube (reaction vial) containing the precursor (**9**). The ^{18}F-labeling reaction was set at 80 ^{o}C for 20 minutes under vacuum, and quenched with NH_4OH (5% in water, 2 mL). The reaction mixture was then loaded onto a Sep-Pak C18 light cartridge. The

cartridge was washed with 2-mL Milli-Q water, and **9b** was eluted with 0.5-mL 1:1 ethanol / saline. The product was subsequently purified by HPLC (method C: retention time of 15.7 min) to totally remove the free [^{18}F]F^{-}. The collected fraction containing **9b** was diluted in 50-mL Milli-Q water and loaded onto a second Sep-Pak C18 light cartridge. Finally, [^{18}F]AMBF$_3$Los was eluted with 0.5-mL 1:1 ethanol / saline and reconstituted with phosphate-buffered saline (PBS) for biological studies (percent of ethanol < 10% in the final formulation).

Using low activities of [^{18}F]F^{-}

Similar to the procedure with high activities, the compound **9a** (25 nmol) was resuspended in a mixture of DMF (15 µL), aqueous pyridazine-HCl buffer (1.0 M, pH 2.0-2.5, 15 µL), and aqueous solution of sodium fluoride (15 mM, 1 µL). No carrier-added [^{18}F]F^{-} (700 ± 200 MBq; 19 ± 5 mCi), was trapped on the µ-QMA cartridge pre-conditioned with ions chloride. The [^{18}F]F^{-} was eluted with 100-µL isotonic saline into the polypropylene Falcon tube (reaction vial) containing the precursor (**9a**). The ^{18}F-labeling reaction also proceeded at 80 ^{o}C for 20 minutes under vacuum, and quenched with NH_4OH (5% in water, 2 mL). The reaction mixture was then loaded onto a Sep-Pak C18 light cartridge, washed with 2-mL Milli-Q water, and **9b** was eluted off with 0.5-mL 1:1 ethanol / saline. HPLC purification was not needed. The final formulation was concentrated at 45 ^{o}C under a slow nitrogen flow, and reconstituted with saline for the biological studies.

4.3.4 Quality control

Aliquots of the final formulation of **1b** and **9b** were analyzed by HPLC to determine the radiochemical purity, molar activity, and confirm the chemical identity. The compound **1b** was analyzed using the methods E and H (retention time of 7.9 ± 0.1 min), while methods D (retention time of 6.0 ± 0.4 min) and I (retention time of 17.60 ± 0.04 min) were used to analyze **9b**. Radiochemical yields were decay-corrected.

The molar activity was calculated at the end of the synthesis using a calibration curve (*nmol of the cold compound* vs. *area under the curve* recorded from the HPLC analytical profile). To calculate the molar activity, the injected activity of hot compound onto the HPLC was divided by the cold amounts (nmol) that were extrapolated from the calibration curve.

The chemical identities of the hot compounds were determined by co-injection with their cold compounds, respectively, onto analytical HPLC.

The radiochemical stability of **1b** and **9b** in saline was also evaluated by analytical HPLC for up to four hours.

Distribution coefficient of **1b** and **9b** at pH 7.4 (log $D_{7.4}$) was determined following a general method described in the literature (Lin *et al.*, 2015). Aliquots of the hot compound (2 µL) were added to polypropylene Falcon tube containing 3-mL octanol and 3-mL PBS. The samples were vortex mixed for 20 seconds (2 times) and centrifuged at 500 x *g* for 15 minutes. Aliquots (0.1 mL) of each layer were counted in a gamma counter to determine the log $D_{7.4}$ as *log [Counts in octanol layer / Counts in PBS layer]*.

Mouse plasma stability of **9b** was assessed following a general protocol previously described for other molecules (Lin *et al.*, 2015). Aliquots of **9b** (0.1 mL) were incubated in 400-µL of balb/c mouse plasma for 5, 15, 30, and 60 minutes at 37 ^{o}C. After each incubation time, the insoluble proteins were precipitated with 0.5-mL MeCN. The samples were centrifuged for 10 minutes; the supernatant was aspirated, filtered and analyzed by HPLC with the method D (retention time of 6.0 ± 0.4 min).

4.4 *In vitro* assays

4.4.1 Competition binding assays in membranes expressing the human AT_1R

The procedure was performed according to the *Recommended Assay Conditions* recommended on the Technical Data Sheet of the purchased hot ligand [^{125}I]-(Sar^{1},Ile^{8})-Angiotensin II. Losartan potassium, FEtLos (**1a**) and $AMBF_3$Los (**9a**) were used as cold ligands whereas losartan potassium was used as a positive control. The Multiscreen MSFCN6B50 - 96 well plates were used for this assay; 1.2 um upper pore size. Briefly, the membranes expressing the human AT_1R were diluted (1:150) with buffer Assay (50 mM tricine (Tris) - HCl pH 7.4, 5 mM magnesium chloride ($MgCl_2$)) to obtain a final concentration of 0.6 µg / well in 200-µL total volume per well. Eight samples of the cold ligand with decreasing concentrations (10^{-4} to 10^{-12} M) were also prepared; the competition assays were done in triplicate for each concentration of cold ligand (24 wells per cold ligand). The concentration of the hot ligand was adjusted to 0.3 nM taking into account the

activity of ^{125}I decay-corrected at the day of the assay and the specific activity of the hot compound (81.4 TBq (2200 Ci)/mmol).

The wells were preincubated for 1-2 hrs at 4 ^{o}C with 200 µL of 0.5 % bovine serum albumin (BSA). Next, all the wells were washed (3 times) with Assay buffer to remove the previous buffer and the plate was thoroughly blotted dry. The membranes (150 µL), cold (25 µL) and hot ligand (25 µL) were sequentially added to each well. After incubating for 60 minutes at 27 ^{o}C under stirring, all the wells were washed (9 times) with cold Wash Buffer (50 mM Tris - HCl pH 7.4). The backing plate was removed; membranes were punched out and counted in gamma counter. Inhibition constants (Ki) of the cold ligands were calculated by non-linear curve fitting using GraphPad Prism 7.01 Software.

4.4.2 Cell culture

MDA-MB-231(ATCC: HTB-26), SKOV3 (ATCC: HTB-77), U251 (Sigma: 08061901), U87 (ATCC: HTB-14), MiaPACA2 (ATCC: HTB-1420), SKBR3 (ATCC: HTB-30), BT474 (ATCC: HTB-20), MCF-7 (ATCC: HTB-22) and the Chinese hamster ovary cells CHO and CHO-AT_1R (a gift of the professor Claudio Costa-Neto from the Department of Biochemistry and Immunology, at the School of Medicine of Ribeirão Preto, University of São Paulo, Ribeirão Preto, Brazil), were cultured in high glucose Dulbecco's modification of Eagle medium (DMEM) (Gibco, Life technologies, MD, USA).

MKN45 [American Type Culture Collection, Manassas, VALLC (Tamura *et al.*, 1996)], PC3 (ATCC: CRL-1435), A549 (ATCC: CCL-185), Skmel-37 (Memorial Sloan-Kettering Cancer Center, N. Y., USA) and AGS (ATCC: CRL-1739) were cultured in Roswell Park Memorial Institute medium (RPMI) (Gibco, Life technologies, MD, USA).

All the cell lines were supplemented with 10% of fetal bovine serum (FBS) (Gibco, Life technologies, MD, USA), penicillin (100 U/mL) and streptomycin (100 µg/mL) (Sigma), and kept at regular normoxic conditions (37 ºC, 5% CO_2 and 21% O_2). For some experiments, cells were maintained under hypoxic conditions (37 ºC, 5% CO_2, 94% N_2 and 1% O_2) for 24 hours, generated using an adjustable hypoxic chamber suitable for cell culture experiments (H35 Hypoxystation, Don Whitley Scientific Ltd, Shipley, UK).

4.4.3 Real-time polymerase chain reaction (RT-PCR)

AT_1R mRNA abundance was assessed by RT-PCR in glioblastoma (U251, U87), pancreas (MiaPACA2), breast (MDA-MB-231, SKBR3, BT474), lung (A549), melanoma (SKMEL37), gastric (MKN45, AGS), prostate (PC3) and ovarian (SKOV3) human cancer cell lines. CHO-AT_1R and CHO cells were used as positive and negative controls of AT_1R expression, respectively. The AT_1R mRNA abundance was also measured in MDA-MB-231-, SKOV3-, MKN45-derived tumors (subcutaneously implanted on mice).

Total RNA from cells and tumors were isolated with Tri-Reagent (Sigma) according to the manufacturer's instructions. Complementary DNA was synthesized using the High capacity cDNA RT kit (Applied Biosystems), according to the manufacturer's protocols. Quantitative PCR analysis was performed in triplicate using the Power SYBR® Green PCR Master Mix (Applied Biosystems). Relative quantification was done using the ΔΔCt method and β-actin to normalize gene expression levels (Table 3 for primers details).

Table 3 – Primer's sequence

Primer	Forward 5' – 3'	Reverse 5' – 3'
Human AT_1R	GCGTCAGTTTCAACCTC	TCCGGGACTCGTAATG
Human β-actin	GCCAGGTCATCACCATTGG	GGTAGTTTCGTGGATGCCACA
Hamster β-actin	GGCAGGCAAAGGTTACTCTG	TGGTGACAGGTGGACAAGAT

Source: thesis author.

4.4.4 Binding assays in AT_1R-expressing cells

Cells were incubated at 4 ^oC for one hour with 10 µCi (370 kBq) of [^{18}F]FEtLos or [^{18}F]AMBF$_3$Los per vial or well, in the presence or absence of the AT_1R blocker. Losartan potassium (100 µM/well/vial) in PBS was used as AT_1R blocker to assess the *in vitro* binding specificity of both radioligands. The cells of the blocking group were treated with losartan 30 minutes before adding the tracer. The assay medium was the same cell culture medium.

All assays with [^{18}F]FEtLos were performed with the cells seeded in 6-well plates. After the tracer incubation, the supernatant was aspirated and the cells were washed six times with ice-cold PBS, removed with 1M NaOH solution (MDA-

MB-231 and MKN45) or a cell scraper (CHO-AT1R and CHO), and transferred to a gamma counter tube.

A set of experiments (MDA-MB-231, SKOV3, MKN45 and CHO-AT_1R) was performed using cells in suspension; the supernatant was removed by centrifugation (500 x *g*, 3 min, 4 ^{o}C) after the tracer incubation, and then, the cell pellet was washed three times with cold PBS, resuspended in PBS and transfer to a gamma counter tube. Another set of experiments (MDA-MB-231, CHO-AT_1R and CHO) was performed using adherent cells in 6-well culture plates; the supernatant was aspirated after the tracer incubation, the cells were washed six times with ice-cold PBS, removed with a cell scraper and transferred to a gamma counter tube. Additional experiments with [^{18}F]AMBF$_3$Los were also performed using adherent cells (MDA-MB-231, SKOV3 and MKN45) seeded in 6-well culture plates under normoxic and hypoxic conditions. In this case, the cells were lysed with trypsin and then transferred to a gamma counter tube.

4.5 *In vivo* assays

4.5.1 Animals

All the experiments were approved by the Institutional Animal Care and Use Committee at IPEN (São Paulo, Brazil) and University of British Columbia (Vancouver, Canada). Female immunodeficient Balb/c Nude mice were obtained from an in-house breeding colony in the Animal Resource Centre at IPEN. Immunodeficient NOD.Cg-*Prkdc*^{scid}*Il2rg*^{tm1Wjl}/SzJ (NSG) mice were obtained from an in-house breeding colony at the Animal Resource Centre at BC Cancer Research Facility.

4.5.2 Tumor-bearing mouse models

Female Balb/c Nude mice were subcutaneously injected with 1 x 10^6 human cancer cells (MKN45, MDA-MB-231 or SKOV3) in a 1:1 mixture of PBS and basement membrane matrigel (BD science) on the left flank. Three (MKN45), five (MDA-MB-231) and six (SKOV3) weeks after tumor cell implantation, *in vivo* and *ex vivo* biodistribution studies were performed. MKN45, MDA-MB-231, and SKOV3-derived tumors were also harvested and frozen to measure the AT_1R mRNA expression.

Female immunodeficient NOD.Cg-*Prkdc*^{scid}*Il2rg*^{tm1Wjl}/SzJ mice were subcutaneously implanted with 17β-estradiol pellets 0.72 mg, 60 day release

(Innovative Research of America). Seven days later, mice were subcutaneously injected with 6 x 10^6 MCF-7 breast cancer cells in a 1:1 mixture of PBS and basement membrane matrigel (BD science) on the left shoulder. Four weeks after cell implantation, *in vivo* and *ex vivo* studies with [^{18}F]AMBF$_3$Los were performed. MCF7 cells are AT_1R-positive breast cancer cell line according to the literature (Du *et al.*, 2012; Chen *et al.*, 2013).

4.5.3 µPET/CT imaging

Mice were divided into baseline and AT_1R blocked groups in some experiments to assess the tracer AT_1R binding specificity. Losartan potassium (dissolved in PBS) was the AT_1R blocker and always co-injected with the tracer. Before and during the acquisition, mice were sedated with a continuous flow of isoflurane.

Dynamic PET scan

Healthy NOD.Cg-*Prkdc*^{scid}*Il2rg*^{tm1Wjl}/SzJ mice were injected via the tail vein with 6 ± 1 MBq (170 ± 38 µCi) of [^{18}F]AMBF$_3$Los at the initial time of PET acquisition after a baseline CT scan for 12 minutes. Sixty-minute dynamic PET scans were carried out on a µPET/CT scanner (Inveon, Siemens) following procedures reported by the lab (Zhang *et al.*, 2017). The dose of the AT_1R blocker losartan was 18 mg/kg.

Static PET scan

Healthy Balb/c Nude and tumor-bearing mice were intravenously injected with the tracer at dose of 8 ± 3 MBq (218 ± 70 µCi). The mice were imaged with a µPET/CT scanner (Inveon, Siemens) in Canada (MCF7); while the Albira µPET/SPECT/CT imaging system (Brucker Corporation, Spain) was used at IPEN with the healthy Balb/c Nude, MDA-MB-231, MKN45, SKOV3 tumor-bearing mice. The µPET/CT imaging at IPEN was recorded using a FOV (field of view) of 60 mm and 15 min for PET scan, and 35 kV and 400 µA for CT scan. The tumor-bearing mice were imaged 60 minutes after tracer injection. The blocking studies in healthy mice were performed using 70 mg/kg of losartan potassium, chosen according to the literature (Coulson *et al.*, 2017).

Additional static PET scans were recorded using the Albira µPET/SPECT/CT imaging system after 60 minutes of intratumoral tracer injection (3.3 ± 0.5 MBq (89 ± 15 µCi)) on MDA-MB-231 tumor-bearing mice. In this case, the dose of losartan was also 70 mg/kg, chosen according to the literature (Coulson *et al.*, 2017).

4.5.4 Autoradiography

After the 60-min dynamic PET scans, the healthy NOD.Cg-*Prkdc*^{scid}*Il2rg*^{tm1Wjl}/SzJ mice were kept sedated with isoflurane, and euthanized using CO_2 inhalation. Kidneys were harvested, rinsed in PBS and frozen in isopentane / dry-ice bath.

Following general procedures of the lab (Zhang *et al.*, 2017), ten µm-thick slides of the kidneys were obtained using a cryostat (Leica), and thaw-mounted onto Superfrost Plus microscope slides (Fisherbrand). Afterwards, the kidney slides were exposed to a phosphor screen overnight and imaged on a Typhoon FLA 9500 scanner (GE Healthcare).

4.5.5 *Ex vivo* biodistribution studies

Mice were intravenous or intratumoral injected with tracer dose of 3 ± 1 MBq (90 ± 27 µCi). AT_1R blocker losartan (70 mg/kg) was co-injected with the tracer for *in vivo* blocking studies. Mice were sedated with isoflurane before euthanasia. Healthy Balb/c Nude mice were euthanized by cervical dislocation 10 min post injection (p.i.). The healthy NSG, MCF7, MDA-MB-231, MKN45, and SKOV3 tumor-bearing mice were euthanized 60 min p.i. by CO_2 inhalation (Canada) or cervical dislocation (Brazil). Blood, tumor, organs, bone and muscle were harvested, rinsed in PBS, weighted and counted in a gamma counter to quantify the percentage of injected dose per gram of tissue (%ID/g).

4.5.6 Blood clearance

MDA-MB-231, MKN45, and SKOV3 tumor-bearing mice were injected with 3 ± 1 MBq (90 ± 27 µCi) of [^{18}F]AMBF$_3$Los. At 0, 5, 10, 20, 30 and 60 minutes after tracer injection, blood samples (5 µL) were collected and counted in a gamma counter. Then, the counts were converted into percentage of injected dose per volume of blood (%ID/µL) to calculate the half-life of [^{18}F]AMBF$_3$Los by one phase decay curve using GraphPad Prism 7.01 Software.

4.6 Statistical analysis

Data was expressed as the mean ± standard deviation (SD). Results of the RCCD were statistically processed by an analysis of variance (multifactor ANOVA) using the software STATGRAPHICS Plus *version 5.0*. The rest of the statistical analysis was performed using GraphPad Prism 7.01 Software. Results of the RT-PCR assays were analyzed by one-way ANOVA (Tukey´s multiple comparisons test). One unpaired t-test (multiple t tests) was used to analyze the blocking effect at the *in vitro* and ex *vivo* assays. One-way ANOVA (Dunnett´s multiple comparisons test) was used to compare each tissue uptake to blood at the *ex vivo* biodistribution data. The outliers were removed before analyzing the data. A <0.05 p-value was considered statistically significant.

5 RESULTS

5.1 Chemistry

5.1.1 Synthesis of the cold FEtLos

We initially started the synthesis of a new analog of 2-butyl-4-chloro-5-hydroxymethyl-1-[(2´-(1*H*-tetrazol-5-yl)biphenyl-4-yl)methyl]-1*H*-imidazole (losartan) aiming for a substitution in the imidazole 5-position. Two synthetic routes were designed and tested for that purpose (scheme 1A e 1B).

The synthetic route from scheme 1A, originated two compounds, 2-butyl-4-chloro-5-(2-fluoroethoxy)methyl-1-[(2´-(1*H*-tetrazol-5-yl)biphenyl-4-yl) methyl]-1*H*-imidazole (**1a**) and, 2-butyl-4-chloro-5-(hydroxymethyl)-1-[(2´-(1*H*-(1-(2-fluoroethyl))tetrazol-5-yl)biphenyl-4-yl)methyl]-1*H*-imidazole (**2a**) with substitution at the imidazole 5-position and tetrazole moiety, respectively. Both **1a** and **2a** are regioisomers, and were obtained as a result of an alkylation reaction of losartan potassium, commercially available, with the prosthetic group 2-fluoroethyl tosylate following a one-step synthetic route (scheme 1A) with poor yields. In spite of the complex mixture of by-products originated from this reaction, **1a** and **2a** were successfully purified by flash column chromatography.

The synthetic route, scheme 1B, on the other hand, originated the compound **1a** as a single regioisomer from the alkylation of the tetrazole-protected losartan (**3**) followed by an acid trityl removal with poor yield (scheme 1B).

Both compounds (1**a** and 2**a**) were analyzed by HRMS and NMR techniques that confirmed the chemical structure of the regioisomers**.** HRMS and NMR data reported below.

Compound **1a**: 26% yield following reaction scheme 1A, and 15% yield following the last step of the reaction scheme 1B, obtained as light-yellow oil. **^{1}H NMR (300 MHz, $CDCl_3$)** δ_H 7.82 (dd, *J* = 7.4 Hz, 1.4 Hz, 1H), 7.53-7.32 (m, 4H), 7.08 (d, *J* = 8.2 Hz, 2H), 6.89 (d, *J* = 8.1 Hz, 2H), 5.14 (s, 2H), 4.77 (s, 2H), 4.70-4.65 (m, 1H), 4.64-4.57 (m, 1H), 4.41 (s, 2H), 2.53 (d, *J* = 7.6 Hz, 2H), 1.61 (q, *J* = 7.6 Hz, 2H), 1.29 (sx, *J* = 7.3 Hz, 2H), 0.82 (t, *J* = 7.3 Hz, 3H).**^{13}C NMR (75 MHz, $CDCl_3$)** δ_C 165.6, 148.7, 141.3, 140.8, 135.0, 130.8, 130.5, 130.4, 130.0, 128.0, 127.7, 126.1, 125.8, 124.9, 81.3, 79.0, 53.3, 53.0, 47.5, 29.9, 26.9, 22.6, 13.9. **^{19}F NMR (282 MHz, $CDCl_3$)** δ_F -147.17 (sept, $J_{F\text{-}H}$ = 49.9 Hz (F-CH), $^{3}J_{F\text{-}H}$ = 25.3 Hz (F-C-CH)). **HRMS (ES^+): m/z $[M+H]^+$** calculated for $C_{24}H_{27}ClFN_6O$: 469.1919, found: 469.1923. **(^{1}H,^{13}C)-HMQC (300 MHz, 75 MHz, $CDCl_3$)** $\delta_{H,C}$ 7.90,130.37 ($CH_{biphenyl}$), 7.54,130.18 ($CH_{biphenyl}$), 7.51,127.80 ($CH_{biphenyl}$), 7.43,130.59 ($CH_{biphenyl}$), 7.16,129.81 ($CH_{biphenyl}$), 7.15,125.65 ($CH_{biphenyl}$), 6.98,129.95 ($CH_{biphenyl}$), 6.97,125.67 ($CH_{biphenyl}$), 5.22,47.03 (imidazole-CH_2-biphenyl), 4.85,78.69 (F-CH_2), 4.69,81.06 (F-C-CH_2), 4.49,52.92 (imidazole-CH_2-O-), 2.60,26.52 (CH_2), 1.68,29.55 (CH_2), 1.36,22.19 (CH_2), 0.84,13.44 (CH_3). **(^{1}H,^{13}C)-HMBC (300 MHz, 75 MHz, $CDCl_3$)** showed a correlation over three bonds between the methylene hydrogen (4.70 ppm) from the fluoroethyl moiety and the methylene carbon (52.70 ppm) at imidazole 5-position (Figure 6).

Figure 6 – Chemical structure of FEtLos (**1a**). The red arrow indicates the methylene hydrogens from the fluoroethyl moiety, which correlates with the methylene carbon at imidazole 5-position.

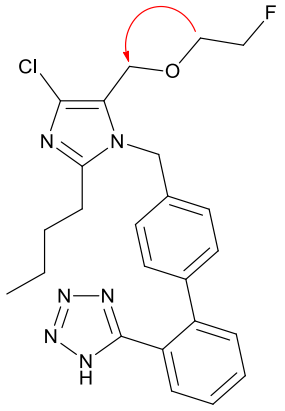

Source: thesis author.

Compound **2a**: 7% yield as light yellow oil. **^{1}H NMR (400 MHz, $CDCl_3$)** δ_H 7.67 – 7.59 (m, 1H), 7.52 – 7.46 (m, 2H), 7.19 (s, 2H), 7.05 (d, J = 8.4 Hz, 2H), 6.87 (d, J = 8.4 Hz, 2H), 5.11 (s, 2H), 4.46 (t, J = 5.0 Hz, 1H), 4.41 (s, 2H), 4.34 (t,

J = 5.0 Hz, 1H), 3.86 (t, J = 5.0 Hz, 1H), 3.80 (t, J = 5.0 Hz, 1H), 2.48 – 2.44 (m, 2H), 1.63 – 1.53 (m, 2H), 1.27 (sx, J = 7.4 Hz, 2H), 0.81 (t, J = 7.2 Hz, 3H). **^{19}F NMR (282 MHz, $CDCl_3$)** δ_F -147.16 (sept, J_{F-H} = 49.1 Hz (F-CH), $^3J_{F-H}$ = 24.5 Hz (F-C-CH)). **HRMS (ES^+): m/z $[M+H]^+$** calculated for $C_{24}H_{26}ClFN_6O$, 469.1919, found 469.1923. As expected, **(^{1}H,^{13}C)-HMBC (400 MHz, 75 MHz, $CDCl_3$)** did not show a heteronuclear correlation between the methylene hydrogen from the fluoroethyl moiety and the methylene carbon at imidazole 5-position.

Compound **3**: 83% yield as white powder. **^{1}H NMR (300 MHz, DMSO)** δ_H 7.77 (d, J = 7.5 Hz, 1H), 7.62 – 7.49 (m, 2H), 7.41 – 7.27 (m, 10H), 7.04 (d, J = 8.1 Hz, 2H), 6.90 – 6.83 (m, 8H), 5.21 (t, J = 5.2 Hz, 1H), 5.17 (s, 2H), 4.19 (d, J = 5.1 Hz, 2H), 2.35 (t, J = 7.6 Hz, 2H), 1.39 (q, J = 7.5 Hz, 2H), 1.12 (sx, J = 7.4 Hz, 2H), 0.71 (t, J = 7.3 Hz, 3H). **HRMS (ES^+): m/z $[M+H]^+$** calculated for $C_{41}H_{37}ClN_6O$, 665.2795; found, 665.2811. Similar to previous works (Hadizad *et al.*, 2011), the correlation between the hydroxyl proton (5.17 ppm) and methylene protons (4.19 ppm) linked to the imidazole ring was also found in our case by the two-dimensional **(^{1}H,^{1}H)-COSY (300 MHz, DMSO)**.

Compound **4a**: 33% yield as yellow oil. **^{1}H NMR (300 MHz, $CDCl_3$)** δ_H 7.93 (dd, *J* = 7.5 Hz, 1.5 Hz, 1H), 7.53-7.41 (m, 2H), 7.38-7.32 (m, 4H), 7.29-7.22 (m, 6H), 7.11 (d, *J* = 8.2 Hz, 2H), 6.95-6.90 (m, 6H), 6.75 (d, *J* = 8.3 Hz, 2H), 5.07 (s, 2H), 4.53-4.44 (m, 1H), 4.39-4.33 (m, 1H), 4.23 (s, 2H), 3.62-3.54 (m, 1H), 3.52-3.45 (m, 1H), 2.57-2.47 (m, 2H), 1.77-1.56 (m, 2H), 1.36-1.20 (m, 2H), 0.86 (t, *J* = 7.3 Hz, 3H).**^{13}C NMR (75 MHz, $CDCl_3$)** δ_C 164.1, 149.0, 141.4, 141.0, 134.6, 130.9, 130.4, 130.3, 130.1, 130.0, 129.3, 129.2, 128.5, 128.1, 127.9, 127.8, 126.4, 125.4, 121.7, 83.6, 83.0, 82.0, 68.60, 68.4, 61.1, 47.3, 29.9, 26.9, 22.5, 13.9. **HRMS (ES^+): *m/z* $[M+H]^+$** calculated for $C_{43}H_{41}ClFN_6O$: 711.3014; found: 711.3018. The two-dimensional **(^{1}H,^{1}H)-COSY (300 MHz, $CDCl_3$)** spectra did not show the signal for the coupling of the hydroxyl proton to the methylene protons.

In conclusion, HMBC spectroscopy detected some differences between **1a** and **2a** (scheme 1A) regarding the correlation between the methylene hydrogen from the fluoroethyl moiety and the methylene carbon at the imidazole 5-position. Although two losartan analogs were obtained, only the regioisomer 1**a** was considered for further studies. Compound 2**a** lacks the 5-substituted tetrazole with mobile hydrogen which is indispensable for the binding affinity of losartan to AT_1R. Indeed, the negatively-charged tetrazole moiety plays a crucial role in receptor

binding through salt bridge formation with basic amino acid residues of the AT_1R (Carini *et al.*, 1991; Vauquelin *et al.*, 2001; Zhang *et al.*, 2015).

5.1.2 Synthesis of the cold $AMBF_3$Los

2-Butyl-4-chloro-5-[((1*H*-1,2,3-triazol-4-yl)-(*N,N*-dimethyl-ammonio methyl-trifluoroborate)methyl)methyl]-1-[(2´-(1*H*-tetrazol-5-yl)biphenyl-4-yl)methyl]-1*H*-imidazole (**9a**) was also synthetized as new derivative of losartan with substitution at the imidazole 5-position. Compound **9a** ($AMBF_3$Los) was synthetized by click chemistry in mild conditions with moderate yield. As illustrated in scheme 2, the hydroxyl group of the compound **3** was substituted by the azide function resulting into compound **7** with good yields; the $AMBF_3$-alkynyl (**6**) was synthetized in moderate yield. Next, compound **8** was synthetized by acid removal of trityl protecting group in excellent yield. Finally, compound **9a** was synthetized by a copper (I)-catalyzed cycloaddition of the compounds **6** and **8**, that exclusively delivered the 1,4-disubstituted regioisomer as expected. The copper (I) catalyst was *in situ* formed by reduction of copper (II) with sodium ascorbate. NH_4OH (5%) was immediately added to the solution of $CuSO_4$ / Na asc. in order to avoid the precipitation of the copper (I) complex because of its poor solubility in aqueous solutions (Liu *et al.*, 2015). ^{1}H NMR, ^{19}F NMR, HRMS, (^{1}H,^{13}C)-HMQC showed a direct carbon-hydrogen correlations, and (^{1}H,^{13}C)-HMBC exhibited a correlation between quaternary carbons and protons separated by two, three and four bonds, confirming the identity of **9a** as the cold $AMBF_3$Los.

Compound **5**: 75% yield as fluffy white powder. **MS** calculated for $C_{12}H_{23}BNO_2^+$, 224.1816, found, 224.1609.

Compound **6**: 52% yield as white powder. **MS** calculated for $C_6H_{11}BF_2N$ $[M\text{-}F]^+$, 146.0953, found 146.0576, as previously reported (Liu *et al.*, 2015).

Compound **7**: 77% yield as white powder. **^{1}H NMR (400 MHz, $CDCl_3$)** δ_H 7.96 (dd, J = 1.8 Hz, 7.4 Hz, 1H), 7.48 (qnd, J = 1.8 Hz, 7.0 Hz, 2H), 7.36 - 7.23 (m, 10 H), 7.12 (d, J = 8 Hz, 2H), 6.91 (d, J = 8.4 Hz, 6H), 6.70(d, J = 8.0 Hz, 2H), 4.99 (s, 2H), 3.94 (s, 2H), 2.54 - 2,50 (m, 2H), 1.67 (m, 2H), 1.30 (sx, J = 7.4 Hz, 2H), 0.86 (t, J = 7.4 Hz, 3H). **HRMS (ES^+): *m/z* $[M+H]^+$** calculated for $C_{41}H_{36}ClN_9$, 690.2861; found,690.2859.

Compound **8**: 96.2% yield as white powder. **^{1}H NMR (300 MHz, $CDCl_3$)** δ_H 7.95 (dd, *J* = 7.5 Hz, 1.4 Hz, 1H), 7.66-7.51 (m, 2H), 7.42 (dd, *J* = 7.2 Hz, 1.5

Hz, 1H), 7.15 (d, *J* = 8.2 Hz, 2H), 6.85 (d, *J* = 8.1 Hz, 2H), 5.14 (s, 2H), 4.12 (s, 2H), 2.43 (t, 2H), 1.59 (q, *J* = 7.6 Hz, 2H), 1.32 (sx, *J* = 7.4 Hz, 2H), 0.88 (t, *J* = 7.3 Hz, 3H). **^{13}C NMR (75 MHz, $CDCl_3$)** δ_c 149.3, 140.6, 139.9, 135.1, 131.4, 131.1, 130.7, 130.0, 128.6, 120.3, 77.2, 47.3, 42.9, 30.0, 26.8, 22.5, 13.9. **HRMS (ES^+)**: **m/z $[M+H]^+$** calculated for $C_{22}H_{23}ClN_9$: 448.1765; found: 448.1758.

Compound **9a**: 52% yield as fluffy white powder. **^{1}H NMR (500 MHz, CD_3CN)** δ_H 7.96 (s, 1H), 7.80 (d, *J* = 7.4 Hz, 1H), 7.65 (t, *J* = 7.4 Hz, 1H), 7.56 (t, *J* = 7.4 Hz, 1H), 7.47 (d, *J* = 7.6 Hz, 1H), 6.96 (d, *J* = 8.1 Hz, 2H), 6.68 (d, *J* = 7.9 Hz, 2H), 5.49 (s, 2H), 5.45 (s, 1H), 5.24 (s, 2H), 4.28 (s, 2H), 3.27 (s, 1H), 2.83 (s, 6H), 2.58 (t, *J* = 7.6 Hz, 2H), 1.60 (q, *J* = 7.7 Hz, 2H), 1.33 (h, 2H), 0.87 (t, *J* = 7.3 Hz, 3H).**^{13}C NMR (75 MHz, CD_3CN)** δ_C 149.7, 136.7, 131.3, 131.0, 130.7, 129.3, 128.0, 127.5, 125.6, 59.7, 52.5, 47.0, 42.5, 29.3, 26.3, 21.9, 13.0. **^{19}F NMR (470 MHz, CD_3CN)** δ_F -137.25 – -137.75 (m). **HRMS (ES^+): *m/z* $[M+H]^+$** calculated for $C_{28}H_{34}BClF_3N_{10}$: 613.2702; found: 613.2693. **(^{1}H,^{13}C)-HMQC (300 MHz, 75 MHz, CD_3CN)** $\delta_{H,C}$ 7.98,126.77 ($CH_{triazol}$), 7.81;130,53 ($CH_{biphenyl}$), 7.65,130.72 ($CH_{biphenyl}$), 7.57,127.56 ($CH_{biphenyl}$), 7.48;130.28 ($CH_{biphenyl}$), 6.97,128.73 (2 x $CH_{biphenyl}$), 6.69,125.06 (2 x $CH_{biphenyl}$), 5.50,41.90 (imidazole-CH_2-biphenyl), 5.25,46.45 (imidazole-CH_2-triazole), 4.30,58.90 (triazol-CH_2-N), 3.30,121.10 (CH_2-BF_3), 2.83,51.86 (2 x CH_3), 2.57,29.65 (CH_2), 1.59,28.60 (CH_2), 1.32,21.35 (CH_2), 0.86,12.44 (CH_3). **(^{1}H,^{13}C)-HMBC (300 MHz, 75 MHz, CD_3CN)** $\delta_{H,C}$ 7.97,136.51 (two bonds: $H_{C5\text{-}Htriazol}$ - $C_{4\text{-substituted triazol}}$), 7.80,131.14 (three bonds: $H_{C3'\text{-}H\ biphenyl}$ - $C_{tetrazole}$), 7.46,129.17 (three bonds: $H_{C6'\text{-}H\ biphenyl}$ - $C_{2'\text{- substituted biphenyl}}$), 6.96,135.65 (two bonds: $H_{C3\text{-}H\ biphenyl}$ - $C_{4\text{- substituted biphenyl}}$), 6.96,129.17 (three bonds: $H_{C3\text{-}H\ biphenyl}$ - $C_{1'\text{- substituted biphenyl}}$), 5.24,149.63 (four bonds: $H_{CH2\text{-}imidazol}$ - $C_{2\text{-substituted imidazol}}$), 5.50,129.08 (two bonds:H_{CH2} - $C_{1\text{- substituted biphenyl}}$), 5.24,125.34 (two bonds: $H_{CH2\text{-}imidazol}$ - $C_{5\text{-substituted imidazol}}$), 5.24,119.40 (three bonds: $H_{CH2\text{-}imidazol}$ - $C_{4\text{-substituted imidazol}}$), 4.28,136.54 (two bonds: $H_{CH2\text{-}N\text{-}dimethylammonio}$ - $C_{4\text{-substituted triazol}}$), 2.58,149.54 (two bonds: $H_{n\text{-}butyl\ chain}$ - $C_{2\text{-substituted imidazol}}$) (Figure 7).

Figure 7 – Chemical structure of AMBF$_3$Los (**9a**). The carbons that were referred at the (^{1}H,^{13}C)-HMBC data are represented in red, blue and pink colors.

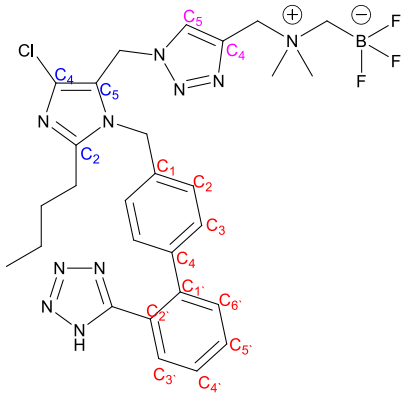

Source: thesis author.

5.2 Radiochemistry

5.2.1 Radiosynthesis of [^{18}F]FEtOTs

The radiosynthesis of the [^{18}F]fluoroalkylating agent [^{18}F]FEtOTs was optimized from a radiation safety point of view varying some reaction parameters. Firstly, results of the radiolabeling reaction in sealed and non-sealed vials suggested the formation of one radioactive volatile side-product with the reaction conditions: 130 ^{o}C, 15 min, 2 mg of K_2CO_3, and 1200 ± 200 MBq of [^{18}F]F^-.

HPLC analysis of the crude mixtures (Figure 8) showed the formation of ^{18}F-labeled side-products with retention times between 2.5 and 5 min. However, the HPLC signals of these side-products were smaller when the reaction was done in a non-sealed vial in which the solvent was completely evaporated in comparison to the sealed vial. We therefore considered that the ^{18}F-labeled side-product with a retention time of ~5 min was a volatile by-product because the signal was considerably decreased in the radiochromatogram of the crude mixture after complete evaporation of solvent (non-sealed vial) in comparison to the sealed vial. In addition, we could observe a loss of ^{18}F activity, (decay-corrected) by 20%, when the reaction proceeded in non-sealed vials while the activity of ^{18}F was invariable in the sealed vials. Since the radiosynthesis of [^{18}F]FEtOTs may increase the risk of a radioactive contamination because of the formation of a radioactive gas, all further radiolabeling reaction were performed in sealed vials.

Figure 8 – Radiochromatograms of the crude mixture of [^{18}F]FEtOTs (8.16 ± 0.04 min) in non-sealed (A) and sealed (B) reaction vials. The analyses showed a decreased signal of ^{18}F-labeled side-products (2.5-5 min) when solvent evaporation was complete (A). The analytical HPLC conditions were 55:45, 0.1% TFA water / MeCN, 1 mL/min.

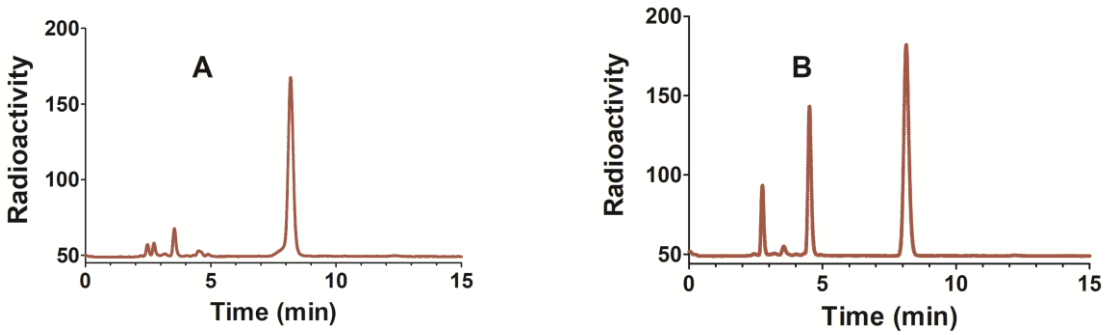

Source: thesis author.

Next, different temperatures (70 ºC to 130 ºC) and reaction times (3 to 15 min) were tested to evaluate the best condition for [^{18}F]FEtOTs production, without the formation of volatile compounds. The HPLC profiles of the crude mixtures from the different radiolabeling conditions tested are shown in Figure 9. As shown, an increase of the reaction time from 3 min (Figure 9A) to 15 min (Figure 9B) at the minimum test temperature (70 ^{o}C), enhanced the formation of a side product with retention time of approximately 5 minutes ([^{18}F]FSP5). When the temperature was raised to 130 ºC (Figure 9C and 9D), an increase in the formation of [^{18}F]FSP5 was observed in comparison to 70 ºC. The formation of [^{18}F]FSP5 at 130 ºC was further improved when the reaction time raised from 3 min (Figure 9C) to 15 min (Figure 9D). The crude yields of [^{18}F]FEtOTs, analyzed by HPLC, was in the range of 60 and 74%; the higher yield (74%) was reached when temperature was set at 70 ºC with a reaction time of 15 min.

Figure 9 – Radiochromatograms of crude mixtures of [^{18}F]FEtOTs (8.6 ± 0.5 min) at different combinations of labeling temperature and reaction times in sealed vials. A: 70 ^{o}C for 3 min. B: 70 ^{o}C for 15 min. C: 130 ^{o}C for 3 min. D: 130 ^{o}C for 15 min. The signal of the ^{18}F-labeled side-product with retention time of ~5 min ([^{18}F]FSP5) was maximum at the highest test temperature (130 ^{o}C). The analytical HPLC conditions were 55:45, 0.1% TFA water / MeCN, 1 mL/min.

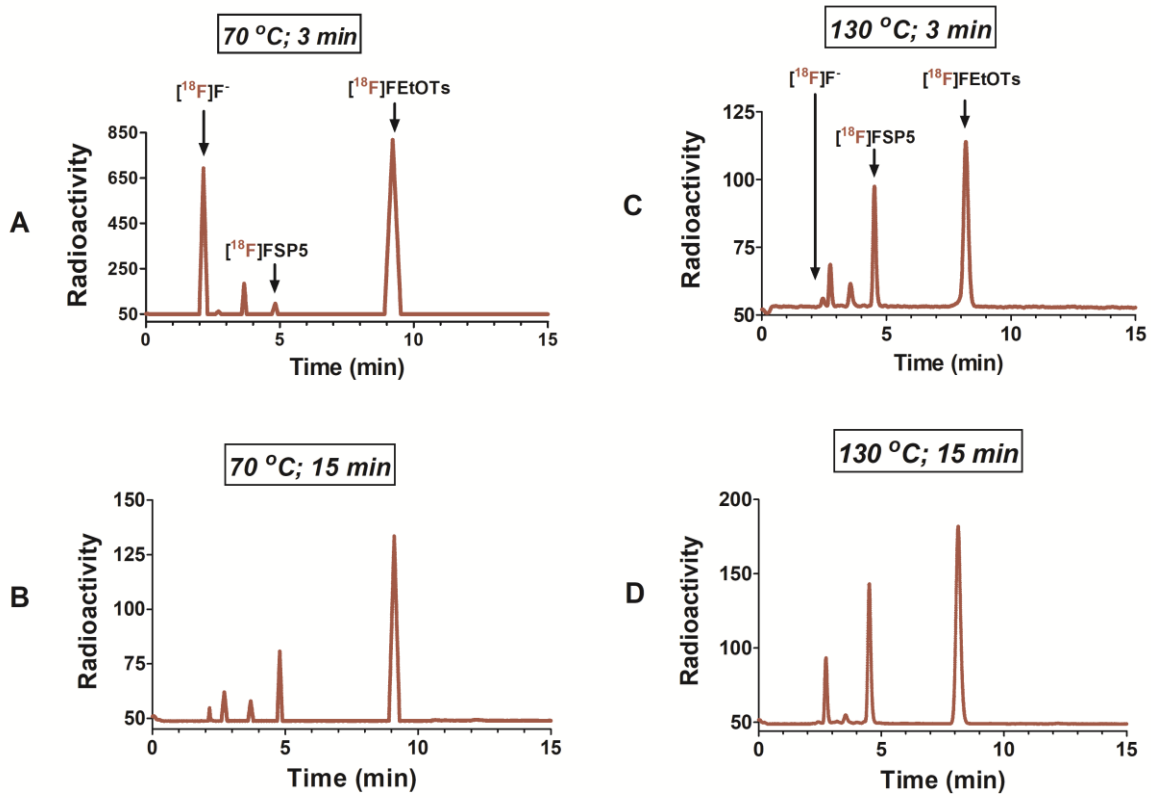

Source: thesis author.

Next, the radiosynthesis of [^{18}F]FEtOTs was optimized using a rotatable central composite design (RCCD) matrix to choose the best reaction time and temperature conditions to obtain the final product with the lowest percentage of the volatile by-product (observed at a retention time of ~5 min). Ten different combinations of labeling temperature and reaction time were performed and the percentage of ^{18}F-labeled side-product ([^{18}F]FSP5) (in the crude yield by HPLC) and the analysis of variance, are presented in Table 4.

Table 4 – Results from the rotatable central composite design for the volatile ^{18}F-labeled side-product [^{18}F]FSP5

RCCD matrix			***Experimental results***	***Analysis of variance***	
Exp. No.	T (^{o}C)	t (min)	[^{18}F]FSP5 (%)		
1	70	3	2	Effect	p-value
2	70	15	16	T (^{o}C)	0.0023*
3	130	3	26	t (min)	0.0177*
4	130	15	28	T (^{o}C) * t (min)	0.1471
5	100	9	23	T (^{o}C) * T (^{o}C)	0.5215
6	100	9	20	t (min) * t (min)	0.8304
7	100	9	18		
8	100	10	23	*significance at p < 0.05	
9	79	9	13		
10	121	9	20		
11	100	5	11		
12	100	13	25		
Experimental standard deviation = 2					

Source: thesis author.

The highest yield of [^{18}F]FSP5 (28%) was observed at both the maximum temperature (130 ^{o}C) and reaction time (15 min) tested (exp. 4); whereas the lowest yield of [^{18}F]FSP5 (2%) was obtained with the minimum temperature (70^{o}C) and time reaction (3 min) tested (exp. 1). The experimental results showed that the combinations of 70 ^{o}C & 15 min, 100 ^{o}C & 5 min, 79 ^{o}C & 9 min and 70 ^{o}C & 3 min led to the lowest percentage of [^{18}F]FSP5 by-product while [^{18}F]FEtOTs, was obtained with 74%, 67%, 62% and 61% in the crude yields by HPLC (data not shown), using the same experimental conditions, respectively. The analysis of variance confirmed the significant influence of the temperature (p = 0.0023 at 95% confidence) and time (p = 0.0177 at 95% confidence) in the percentage of [^{18}F]FSP5 production. Pareto chart (Figure 10) showed that both temperature and reaction time positively favor the formation of [^{18}F]FSP5.

Figure 10 – Pareto chart obtained from the statistical analysis of the experimental results on the obtained yield of [^{18}F]FSP5. The chart shows the significant positive influence of increasing the labeling temperature and reaction time with a 95% confidence for the formation of [^{18}F]FSP5.

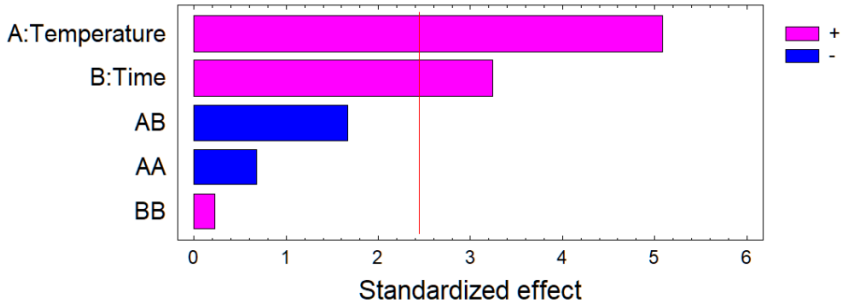

Source: thesis author.

Afterward, we evaluated the formation of [^{18}F]FSP5 by shortening the reaction time to one minute and heating at 100 ^{o}C, and found an increased formation of [^{18}F]FEtOTs with low formation of [^{18}F]FSP5 (6% ± 2%; n=5). At these conditions, the crude yield of [^{18}F]FEtOTs by HPLC was 80% ± 4% (n=5), and the identity of [^{18}F]FEtOTs was confirmed by comparing with the profile of the cold compound (Figure 11). These experiments were achieved with 1.8 ± 0.3 GBq of [^{18}F]F^{-}.

Figure 11 – Radiochromatogram of the crude mixture of [^{18}F]FEtOTs (8.8 min) after heating at 100 ^{o}C for 1 min. The HPLC profile of the cold compound (8.7 min) confirmed the chemical identity of the hot compound [^{18}F]FEtOTs. The analytical HPLC conditions were 55:45, 0.1% TFA water / MeCN, 1 mL/min.

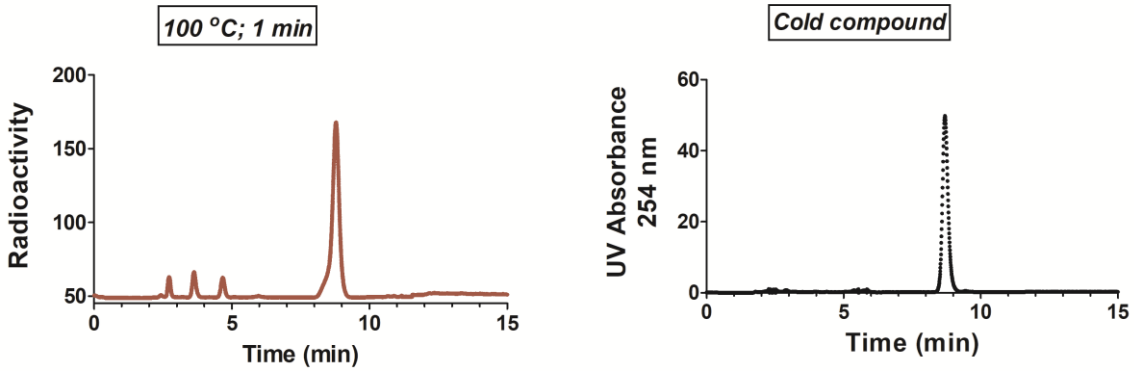

Source: thesis author.

Additional experiments with 130 ^{o}C, 15 min and sealed vials were performed using a lower (0.7 mg) and higher (5 mg) amount of K_2CO_3 than the conventionally used (2 mg) during the elution of [^{18}F]F^{-} (1200 ± 100 MBq) from the

QMA cartridge. The HPLC profiles showed in Figure 12, a high percentage (>90%) of free [^{18}F]F$^-$ when a low mass of K_2CO_3 (0.7 mg) was used for the labeling. In contrast, the addition of 2 and 5 mg of K_2CO_3 led to the formation of 28% and 12% [^{18}F]FSP5, respectively, whereas the crude yield of [^{18}F]FEtOTs obtained by HPLC was 60% and 65%, respectively.

Figure 12 – Radiochromatograms of the crude mixture of [^{18}F]FEtOTs (8.1 min) varying the amounts of K_2CO_3. The reaction was set at 130 ^{o}C for 15 min with 0.7 mg (A), 2 mg (B) or 5 mg (C) of K_2CO_3. Low mass of K_2CO_3 (0.7 mg) affected the labeling reaction; while 2 and 5 mg afforded 60% and 65% crude yields for [^{18}F]FEtOTs, respectively. Besides, 2 mg formed higher [^{18}F]FSP5 (28%). The analytical HPLC conditions were 55:45, 0.1% TFA water / MeCN, 1 mL/min.

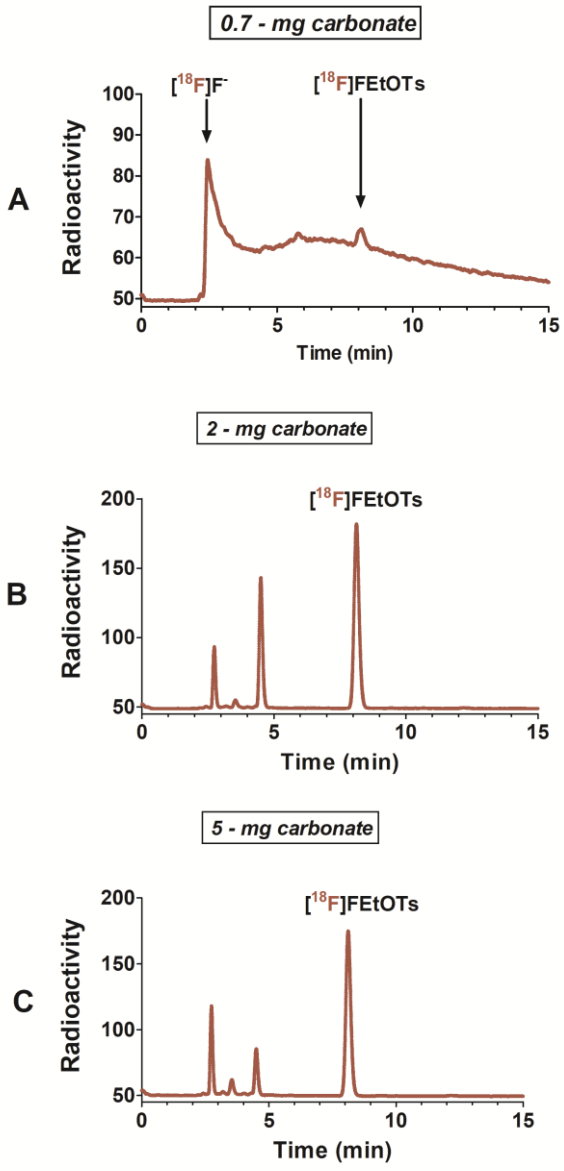

Source: thesis author.

Therefore, the subsequent manual radiosyntheses of [^{18}F]FEtOTs were performed at 100 ^{o}C for 1 min in sealed vials, which were the best reaction conditions observed from a radiation safety point of view (lower amount of volatile compound), also improving both the reaction time and [^{18}F]FEtOTs yield. The amount of K_2CO_3 was kept at 2 mg in further experiments. The radiochemical yield of [^{18}F]FEtOTs was 30% ± 8% (decay-corrected from dried [^{18}F]F^-) after HPLC purification and concentration.

In order to further improve ^{18}F]FEtOTs radiosynthesis, the purification of [^{18}F]FEtOTs using only SPE cartridges (C18 Plus and silica Plus) was also tested following previously described procedures (Schoultz *et al.*, 2013; Khanapur *et al.*, 2014). However, the [^{18}F]fluoroethylation reaction with our target molecules only proceeded when [^{18}F]FEtOTs was purified by semi-preparative HPLC. Purification using SPE cartridges provided ≥92% radiochemical purity of [^{18}F]FEtOTs; however, this purification procedure was not capable of eliminating the precursor ethylene glycol bis-tosylate from [^{18}F]FEtOTs. In contrast, with HPLC purification [^{18}F]FEtOTs was obtained with >99% chemical and radiochemical purity, and the [^{18}F]fluoroethylation reaction was successfully achieved.

5.2.2 Radiosynthesis of [^{18}F]FEtLos

[^{18}F]Fluoroethylation of both losartan potassium (scheme 4A) and compound **3** followed by acid trityl removal (scheme 4B) provided the desired regioisomer **1b** ([^{18}F]FEtLos). The first successful radiosynthesis was performed using 50 mg of losartan potassium as a precursor; however, in subsequent reactions, the mass of the precursor was gradually decreased up to 1 mg without affecting the overall yield. The [^{18}F]Fluoroalkylation of losartan potassium formed two regioisomers, **1b** and **2b,** with an overall yield of 48% and 37% by HPLC, respectively (Figure 13A). Similar to the cold synthesis, [^{18}F]Fluoroalkylation of **3** only formed the ^{18}F-labeled derivative **4b** with a crude yield of 56% analyzed by HPLC. The regioisomer **1b** was formed with a crude yield of 55% after deprotection of tetrazole moiety and without further purification of **4b** (scheme 4B). However, the product **4b** was only formed at higher reaction time (Figure 13B).

Figure 13 – Representative HPLC profiles of both crude mixtures after [^{18}F]fluoroethylation of losartan potassium (A), and compound 3 (B). The retention times of 4a, 3, 1a, 2a and losartan potassium were 24, 22.8, 7.9, 5.7 and 4 min, respectively at 254-nm UV detector. The retention times of 1b and 2b were 7.9 ± 0.1 min and 5.8 ± 0.2 min respectively. The analytical HPLC conditions were 0-15 min, 55:45, 0.1% TFA water / MeCN, 15-20 min, 45-100% MeCN, 20-30 min, 100% MeCN, 1 mL/min.

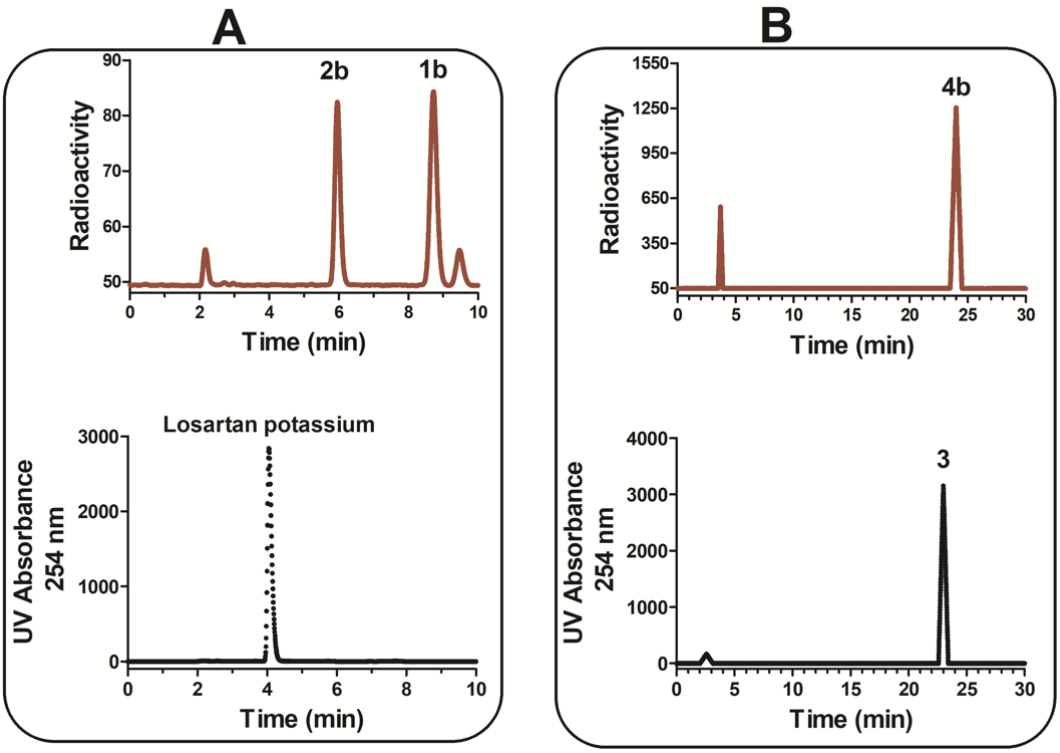

Source: thesis author.

The isomer **1b** was successfully purified by semi-preparative HPLC from the mixture containing **2b,** with >99% chemical and radiochemical purity (Figure 14A). The chemical identity of the [^{18}F]FEtLos was confirmed by analytical HPLC through the co-injection of **1b** and the cold compound ([^{19}F]FEtLos) **1a** (Figure 14B). [^{18}F]FEtLos was prepared in 12% ± 5% yield (decay-corrected from [^{18}F]FEtOTs) and 1.4 ± 1.2 GBq (38 ± 33 mCi)/μmol molar activity (n=12). The overall yield was 2.7% ± 0.9% (decay-corrected from dried [^{18}F]F^{-}). A typical radiosynthesis (scheme 4A) began with 1480 MBq of dried [^{18}F]F^{-} and afforded 13 MBq of [^{18}F]FEtLos, which was enough to perform the biological studies.

Figure 14 – Quality control of the final formulation of [^{18}F]FEtLos . Representative HPLC profiles of the final formulation of 1b (A), and the co-injection of the cold compound 1a (B). The analytical HPLC conditions were 55:45, 0.1% TFA water / MeCN, 1 mL/min.

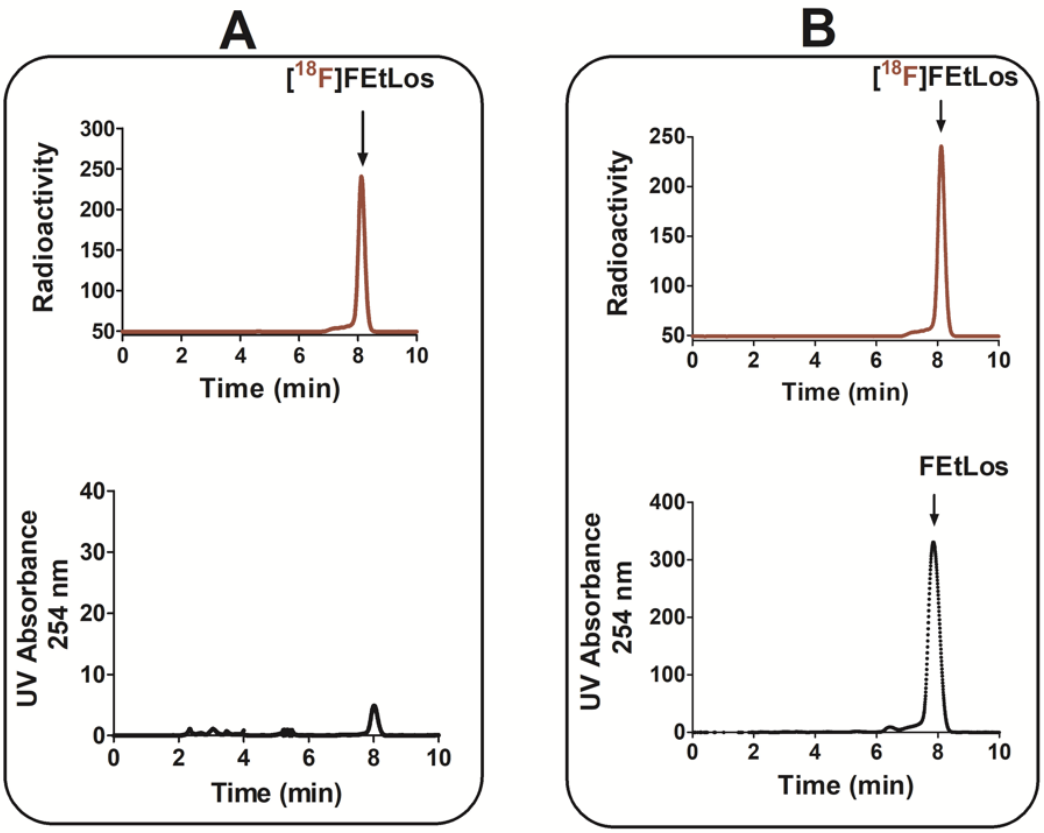

Source: thesis author.

[^{18}F]FEtLos was stable in saline for at least 4 hours (Figure 15) and displayed less lipophilicity (log $D_{7.4}$ = 0.21 ± 0.09 (n=3)) than the parental losartan (log $D_{7.4}$ = 1.7 (Kalgutkar and Daniels, 2010)).

Figure 15 –Stability of [^{18}F]FEtLos in saline. [^{18}F]FEtLos was incubated in saline for 5 min, 1, 2 and 4 hrs. Retention time of the unchanged tracer was 7.9 ± 0.1 min. The analytical HPLC conditions were 55:45, 0.1% TFA water / MeCN, 1 mL/min.

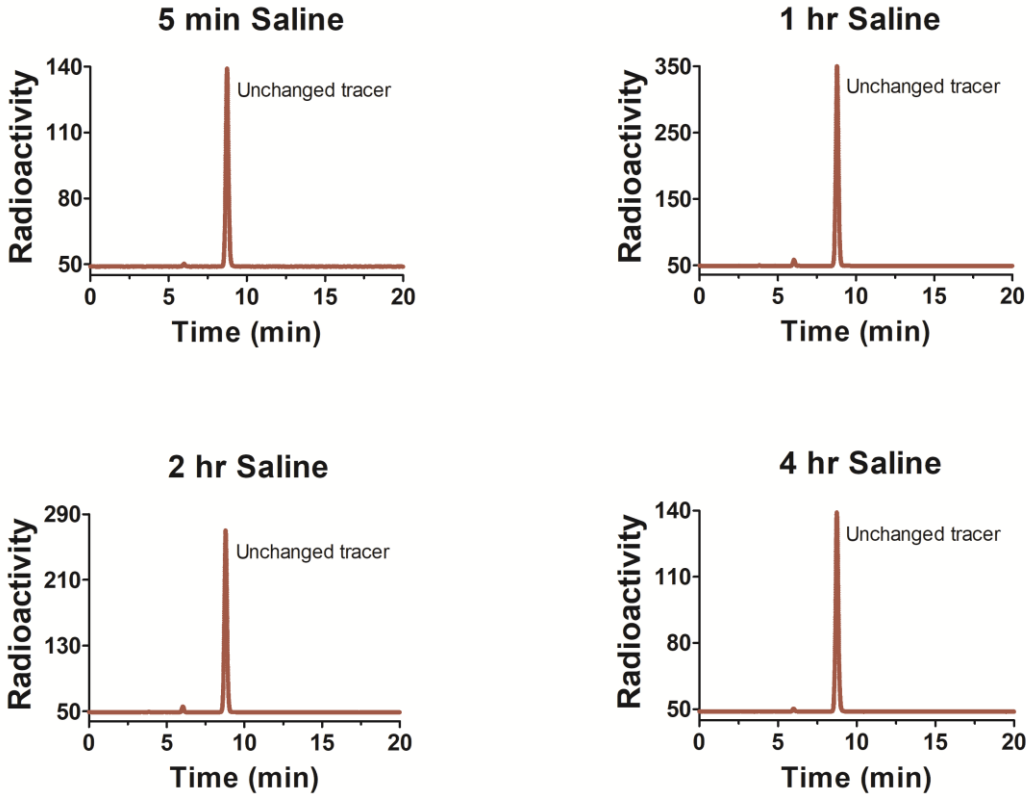

Source: thesis author.

5.2.3 Radiosynthesis of [^{18}F]AMBF$_3$Los

The hot compound [^{18}F]AMBF$_3$Los (**9b**) was synthetized via a ^{18}F-^{19}F isotopic exchange reaction in aqueous medium without azeotropic drying of [^{18}F]F$^-$ in a hot cell using manipulators (Facility in Canada). The labeling reaction started with high ^{18}F activities (61 ± 23 GBq), and 100 nmol (~61 µg) of cold AMBF$_3$Los and led to the production of [^{18}F]AMBF$_3$Los with a good molar activity (108 ± 29 GBq (2.9 ± 0.8 Ci)/µmol). In these conditions, the overall radiochemical yield was 10% ± 1%, and the radiochemical purity was higher than 99%. The total radiosynthesis was achieved within 52-65 minutes, including HPLC purification and reformulation (n=4).

On the other hand, in order to produce manually [^{18}F]AMBF$_3$Los at the Radiopharmacy Center of the IPEN (Brazil) without using manipulators, we tested different reaction conditions. Firstly, we performed the synthesis of [^{18}F]AMBF$_3$Los

using 100-fold lower activities of [^{18}F]F$^-$ and the same amount of precursor (100 nmol), which led to the obtention of [^{18}F]AMBF$_3$Los with radiochemical yield of 26 % and lower molar activity (0.8 GBq/µmol) (entry 1; Table 5) in comparison to the higher molar activity obtained when the synthesis was performed using manipulators (108 ± 29 GBq). In order to increase the molar activity of molecule, the amount of precursor was reduced from 100 to 10 nmol (Table 5). When using 10 nmol of the precursor (entry 4; Table 5), [^{18}F]AMBF$_3$Los was obtained in very low radiochemical yield (4%) but with higher molar activity (4.9 GBq/µmol) in comparison with 100 nmol of the precursor. Therefore, we next tested 25 and 50 nmol of the precursor in order to obtain [^{18}F]AMBF$_3$Los with enough yield and molar activity to enable the *in vivo* studies. As can be seen in Table 5 and Figure 16A, when using 25 nmol of the precursor, [^{18}F]AMBF$_3$Los was obtained with molar activity of 2.9 GBq/µmol, radiochemical yield of 17% and radiochemical purity higher than 97%, and therefore this reaction condition was chosen. A typical manual radiosynthesis started with 700 MBq of [^{18}F]F$^-$ and afforded 60 MBq [^{18}F]AMBF$_3$Los with molar activity of 2.4 ± 0.5 GBq (0.06 ± 0.01 Ci) / µmol, and radiochemical yield of 11 ± 4 %. The total radiosynthesis time, including C18 Sep-Pak purification, solvent evaporation and reformulation was 55-65 min (n=20). The chemical identity of [^{18}F]AMBF$_3$Los was always confirmed by a single peak on the analytical HPLC profile after co-injection of the final formulation with the cold AMBF$_3$Los (Figure 16B).

Table 5 – The best results of radiochemical yield, molar activity and radiochemical purity of [^{18}F]AMBF$_3$Los when different amounts of precursor with low activities of [^{18}F]F$^-$ were tested.

Entry	Precursor (nmol)	Radiochemical yield (%)	Molar activity (GBq/µmol)	Radiochemical purity (%)
1	100	26	0.8	>97
2	50	22	2.1	>97
3	25	17	2.9	>97
4	10	4	4.9	>97

Source: thesis author.

Figure 16 – Quality control of the final formulation of [^{18}F]AMBF$_3$Los. The figure shows representative HPLC profiles of the final formulation of 9b (A), and the co-injection with 9a (B). The retention times of 9a and 9b were 17.50 ± 0.04 min and 17.60 ± 0.04 min, respectively. The analytical HPLC conditions were solvent A: 0.1% TFA water, solvent B: MeCN, 0-30 min, 0-100% B, 1 mL/min.

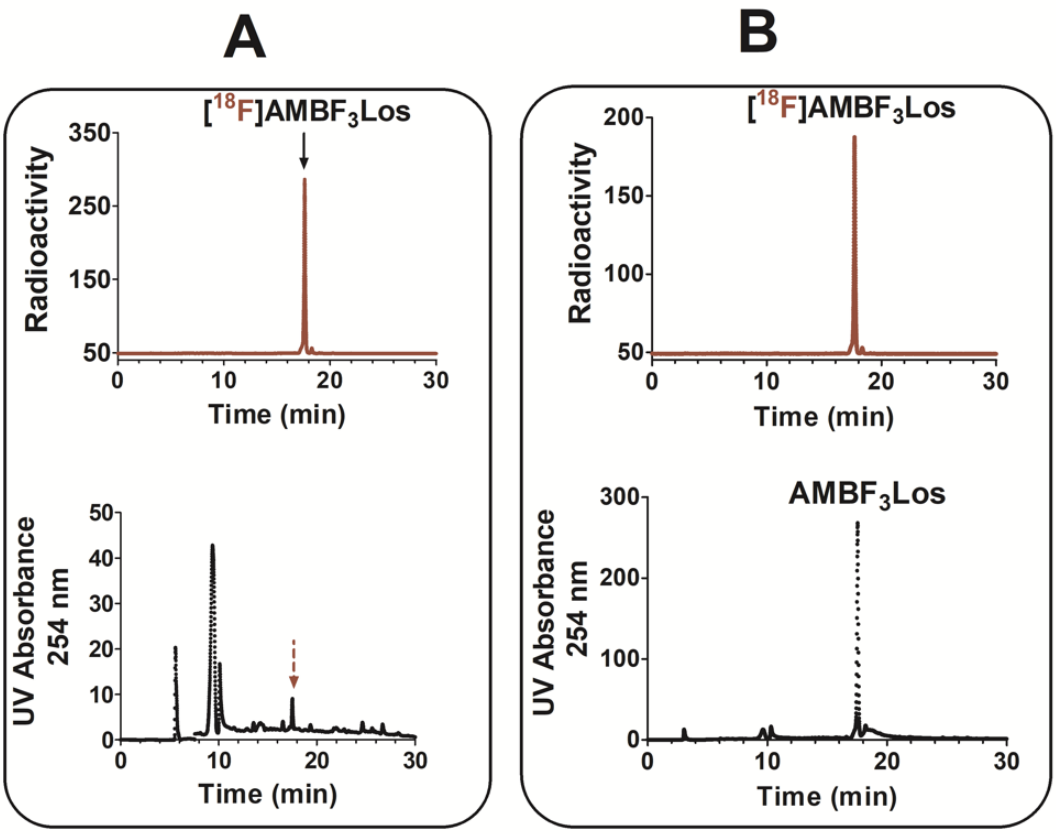

Source: thesis author.

[^{18}F]AMBF$_3$Los displayed a log $D_{7.4}$ of -0.43 ± 0.02 (n=3), and was stable in saline (Figure 17) and mouse plasma for at least 60 min (Figure 18).

Figure 17 –Stability of [^{18}F]AMBF$_3$Los in saline. [^{18}F]AMBF$_3$Los was incubated in saline for 5 min, 1, 2 and 4 hrs. Retention time of the unchanged tracer was 17.60 ± 0.04 min. The analytical HPLC conditions were solvent A: 0.1% TFA water, solvent B: MeCN, 0-30 min, 0-100% B, 1 mL/min.

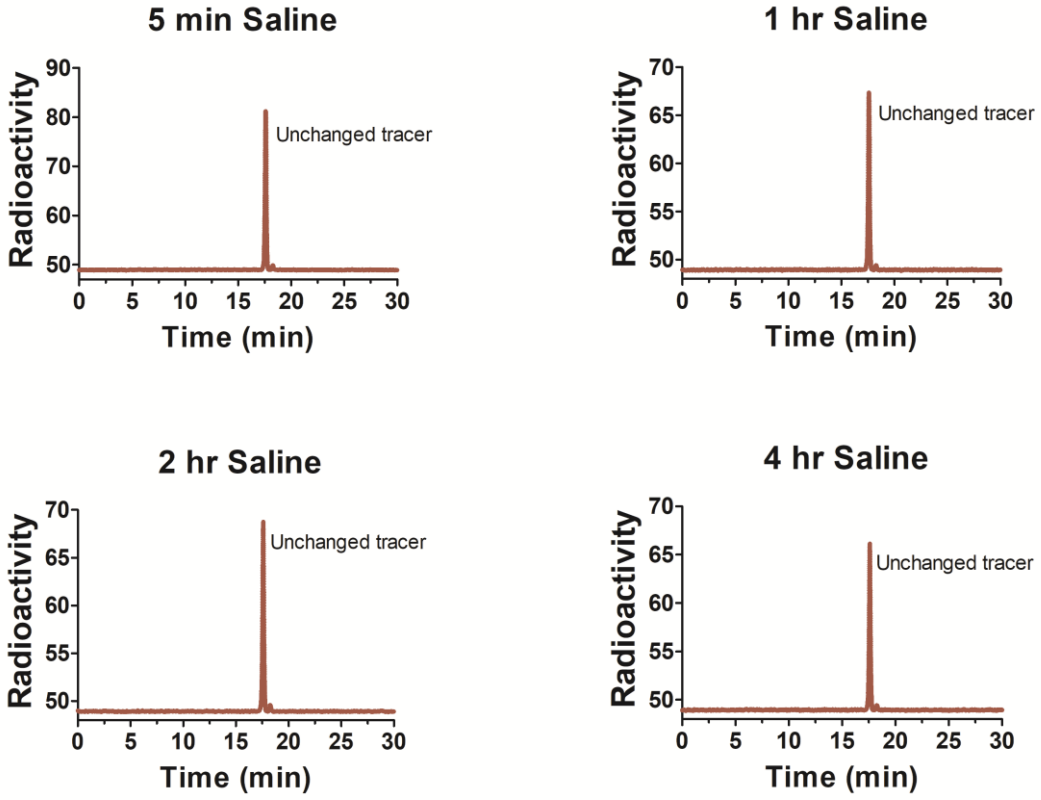

Source: thesis author.

Figure 18 – Mouse plasma stability of [^{18}F]AMBF$_3$Los. [^{18}F]AMBF$_3$Los was incubated in mouse plasma for 5, 15, 30 and 60 min. Retention time of the unchanged tracer was 6.34 ± 0.01 min. The analytical HPLC conditions were 60:40, 0.1% TFA water / 0.1% TFA MeCN, 2 mL/min.

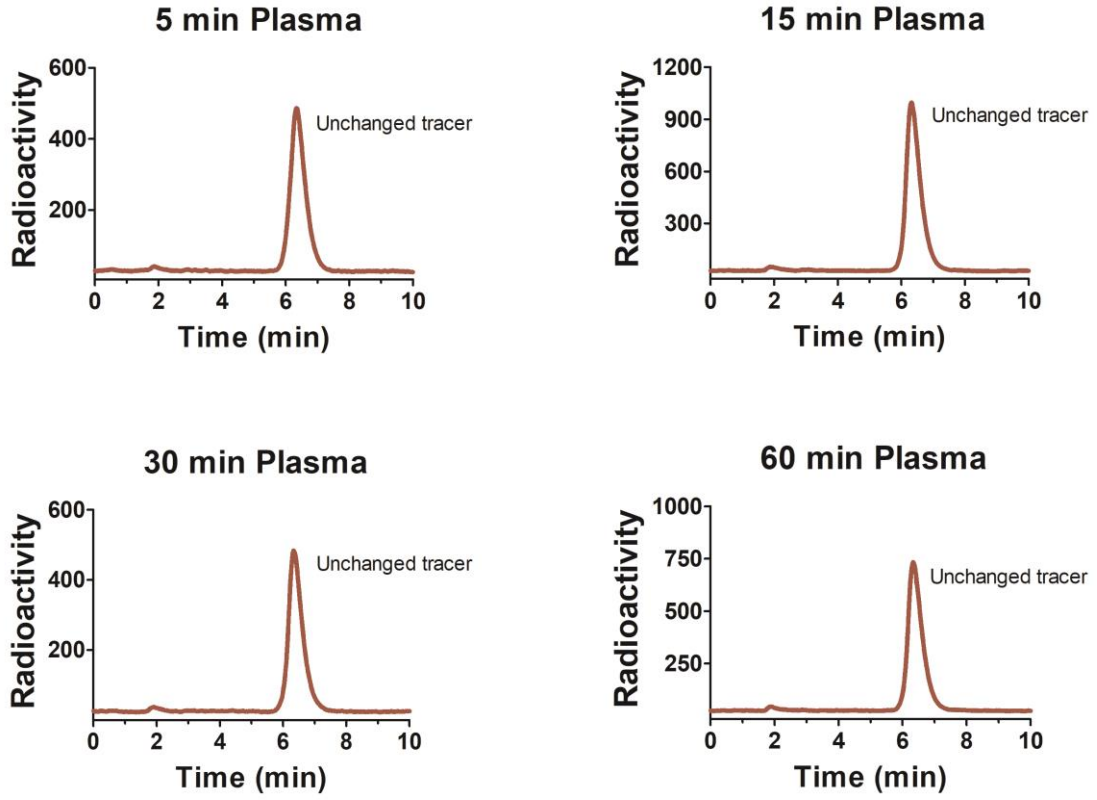

Source: thesis author.

5.3 *In vitro* assays

5.3.1 Competition binding assays in membranes expressing the human AT$_1$R

To evaluate the best radiotracer for the detection of AT$_1$R, we next performed an *in vitro* competition binding assay using the cold ligands FEtLos and AMBF$_3$Los to displace the binding of [^{125}I]-(Sar1,Ile8)-Angiotensin II to AT$_1$R (Figure 19). The Ki values of FEtLos, AMBF$_3$Los and losartan potassium (positive control) were 2.2 ± 0.2 µM (n=3), 7.9 ± 0.4 nM (n=3) and 1.5 ± 0.3 nM (n=3), respectively. AMBF$_3$Los showed the best AT$_1$R binding affinity compared to FEtLos.

Figure 19 – *In vitro* competition binding assays. Competition curve of FEtLos (1a), $AMBF_3Los$ (9a and losartan potassium with [^{125}I]-(Sar1,Ile8)-Angiotensin II to human AT_1R expressed in membranes from CHO-K1 cells. Ki of FEtLos: 2.2 ± 0.2 µM (n=3); Ki of $AMBF_3Los$: 7.9 ± 0.4 nM (n=3); Ki of losartan potassium: 1.5 ± 0.3 nM (n=3).

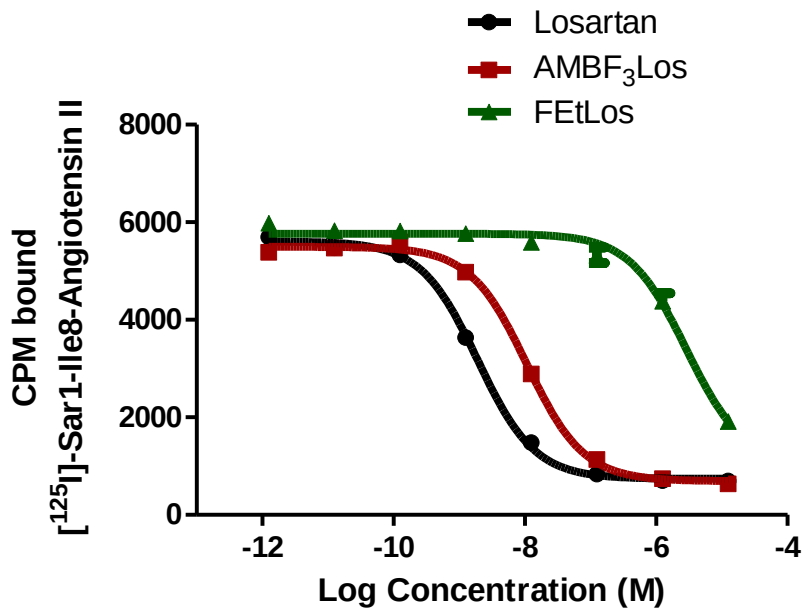

Source: thesis author.

5.3.2 RT-PCR

We next checked the mRNA expression of AT_1R in several cancer cell lines and derived tumors (Figure 20) in order to choose the best model for *in vitro* and *in vivo* binding studies. MDA-MB-231 (breast), SKOV3 (ovary), U251 (glioma), SKBR3 (breast), and MKN45 (gastric) presented a high expression of AT_1R mRNA in comparison to U87 (glioma), MiaPACA2 (pancreas), BT474 (breast), A549 (lung), SKMEL37 (melanoma), PC3 (prostate) e AGS (gastric). Among all cells tested, the one with the highest AT_1R mRNA expression was MDA-MB-231 breast cancer cell line. Nonetheless, MKN45-derived tumor displayed the highest expression of AT_1R mRNA among all tumors analyzed. Interestingly, MDA-MB-23, SKOV3 and MKN45-derived tumors displayed higher AT_1R mRNA abundance compared to their respective cell culture. The non-cancerous cell line overexpressing AT_1R (CHO-AT_1R) showed higher levels of AT_1R than the control CHO. The subsequent *in vitro* and *in vivo* studies were performed using MDA-MB-231, SKOV3 and MKN45 cancer cell lines. CHO cells were included in the *in vitro*

assays to evaluate the specific binding of the radiotracers to AT_1R in AT_1R-overexpressing cells (CHO-AT_1R) and control (CHO).

Figure 20 – AT_1R mRNA expression in several cancer cell lines and some derived tumors. The AT_1R mRNA expression (n=3) was determined by RT-PCR in glioblastoma (U251, U87), pancreas (MiaPACA2), breast (MDA-MB-231, SKBR3, BT474), lung (A549), melanoma (SKMEL37), gastric (MKN45, AGS), prostate (PC3) and ovarian (SKOV3) human cancer cell lines (black bars); Chinese hamster ovary cells (CHO-AT1R, CHO) (gray bars), and MDA-MB-231, SKOV3, MKN45-derived tumors (subcutaneously implanted on mice) (red bars). Relative quantification was done using the ΔΔCt method normalizing to β-actin gene expression. Data analyzed by one-way ANOVA (Turkey´s multiple comparisons test); **** p<0.0001, *** p<0.001, ** p<0.01, * p<0.05, n.s. (not significant).

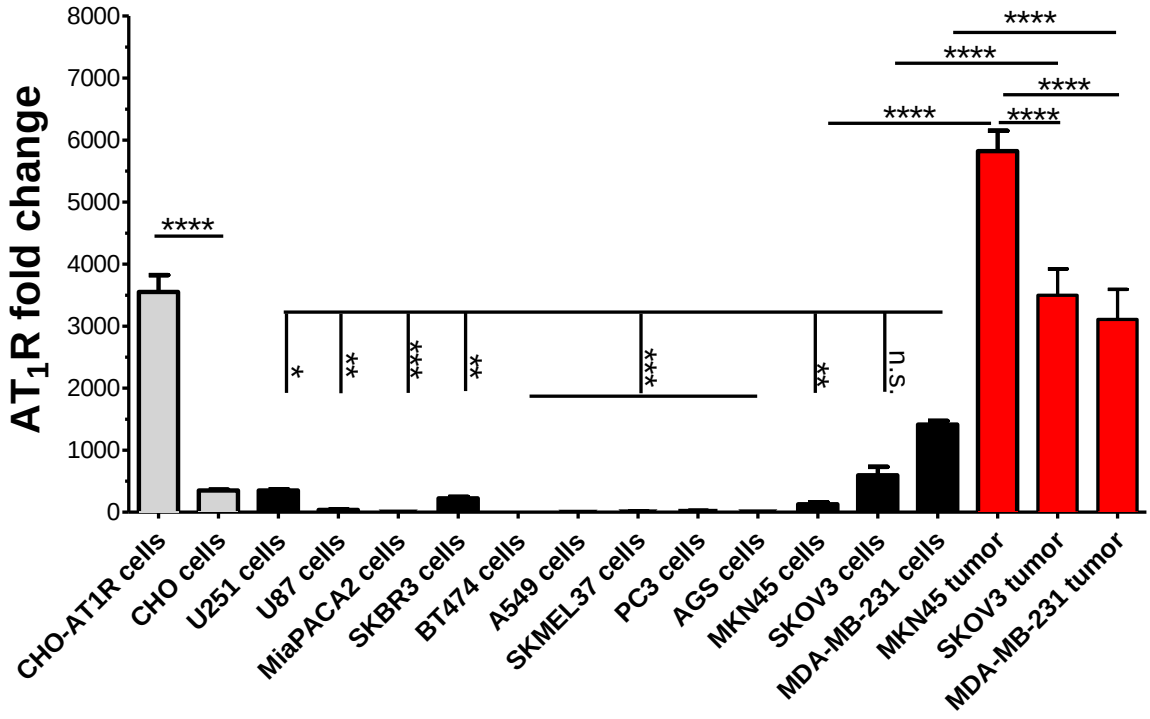

Source: thesis author.

5.3.3 Binding assays in AT_1R-expressing cells

We next evaluated the *in vitro* binding of [^{18}F]FEtLos and [^{18}F]AMBF$_3$Los AT_1R-expressing cells in suspension.

The results of the binding assays with [^{18}F]FEtLos showed high [^{18}F]FEtLos uptake after incubation for 60 minutes at 4 ^{o}C, and a non-significant AT_1R blocking effect (Figure 21). Therefore, the results showed high non-specific binding. We expected quite lower activity uptake since the AT_1R binding affinity of the cold compound FEtLos was low.

Figure 21 – *In vitro* assays with [^{18}F]FEtLos in AT_1R-positive cancer cells (**A**) and non tumoral cells (**B**) after incubation for 60 minutes at 4 ^{o}C in presence (white bars) or absence (black bars) of the AT_1R blocker losartan (100 µM/vial). Graph shows the mean ± SD of three independent experiments (n=3). The blocking effect was analyzed using the one unpaired t-test (multiple t tests); non-significant blocking effect was obtained.

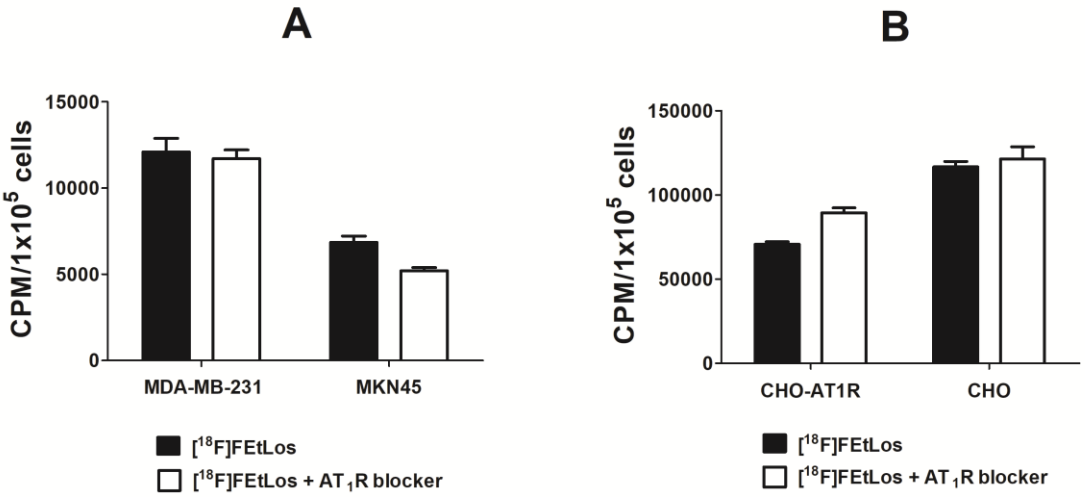

Source: thesis author.

Then, binding assays with [^{18}F]$AMBF_3$Los using cells in suspension (MDA-MB-231, MKN45, SKOV3 and CHO-AT_1R)(Figure 22) demonstrated that the binding of [^{18}F]$AMBF_3$Los to CHO-AT_1R cells was receptor-mediated since saturation of the receptors by preincubation with unlabeled $AMBF_3$Los significantly decreased the binding of the radiolabeled [^{18}F]$AMBF_3$Los ($p<0.001$). Nonetheless, low [^{18}F]$AMBF_3$Los uptake was found in the tested human cancer cells and binding was not inhibited by the cold compound.

Figure 22 – *In vitro* assays with [^{18}F]AMBF$_3$Los in suspension cells. AT$_1$R-positive cancer cells (MDA-MB-231, MKN45 and SKOV3) and the non tumoral CHO-AT$_1$R-overexpressing cell lines were incubated for 60 minutes at 4 ^{o}C in the presence (white bars) or absence (black bars) of potassium losartan (AT$_1$R blocker, 100 µM/vial). Graph shows the mean ± SD of three independent experiments (n=3). The blocking effect was analyzed using the one unpaired t-test (multiple t tests); *** p<0.001.

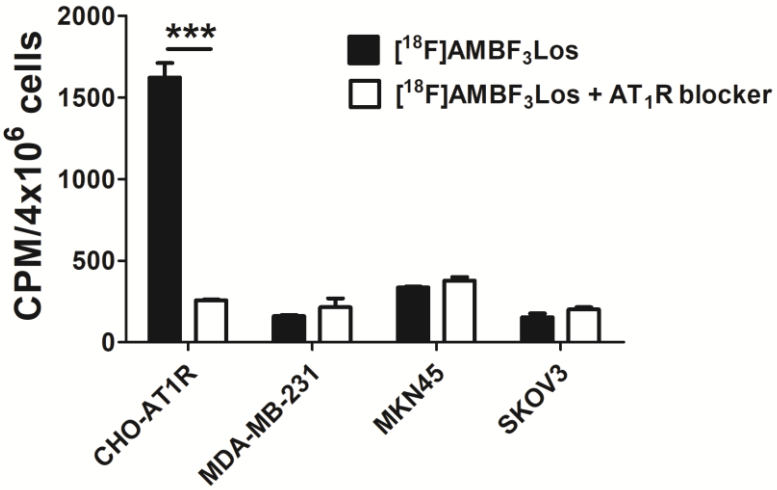

Source: thesis author.

Binding assays with [^{18}F]AMBF$_3$Los were also performed in the human cancer cell line MDA-MB-231, and in the non tumoral cells CHO-AT$_1$R and CHO previously seeded in 6-well plates (Figure 23). Similarly to the previous results, CHO-AT$_1$R exhibited the highest uptake of [^{18}F]AMBF$_3$Los, which was inhibited by AT$_1$R blockade. The uptake levels of [^{18}F]AMBF$_3$Los in MDA-MB-231 cells were similar to the ones found in the control CHO cells.

Figure 23 – *In vitro* assays with [^{18}F]AMBF$_3$Los in cells seeded on 6-well plates. AT$_1$R-positive cancer cells (MDA-MB-231) and the non tumoral CHO and CHO AT$_1$R-overexpressing cells were incubated with [^{18}F]AMBF$_3$Los for 60 minutes at 4 ^{o}C in the presence (white bars) or absence (black bars) of potassium losartan (AT$_1$R blocker, 100 µM/well). Graph shows the mean ± SD of three independent experiments (n=3). The blocking effect was analyzed using the one unpaired t-test (multiple t tests); ***p<0.001.

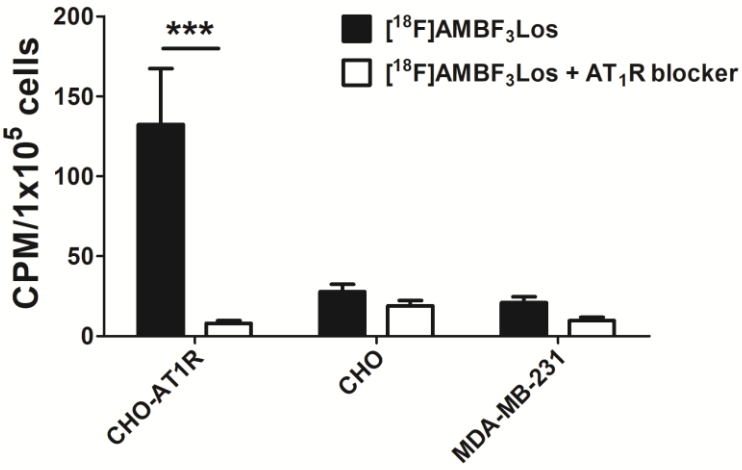

Source: thesis author.

It has been previously reported that AT$_1$R mRNA expression levels increase in cancer cells cultured under hypoxic (1% O_2) conditions for 24 hrs in comparison to normoxic (21% O_2) conditions (Liu *et al.*, 2013; Fan *et al.*, 2014). Based on these results, we subsequently prepared adherent cell cultures of MDA-MB-231, MKN45 and SKOV3 tumor cells under normoxic (21% O_2) or hypoxic (1% O_2) conditions for 24 hours and evaluated [^{18}F]AMBF$_3$Los cellular binding (Figure 24). As shown, hypoxic conditions did not increase [^{18}F]AMBF$_3$Los uptake by cells in comparison to normoxic conditions. However, we found that the previous treatment of SKOV3 cells with losartan potassium blocked [^{18}F]AMBF$_3$Los uptake both in normoxic and hypoxic conditions. On the other hand, AT$_1$R blockade by losartan potassium was only observed in MKN45 and MDA-MB-231 cells cultured under hypoxic conditions.

Figure 24 – *In vitro* assays with [^{18}F]AMBF$_3$Los in MDA-MB-231, MKN45 and SKOV3 cells cultured under normoxic and hypoxic conditions. AT$_1$R-positive cancer cells (MDA-MB-231, MKN45 and SKOV3) were seeded in a 6-well plates and kept under hypoxia or normoxia culture for 24 h (n=3). [^{18}F]AMBF$_3$Los was incubated for 60 minutes at 4 ^{o}C in the presence (white bars) or absence (black bars) of potassium losartan (AT$_1$R blocker, 100 µM/well). Graph shows the mean ± SD of three independent experiments (n=3). The blocking effect was analyzed using the one unpaired t-test (multiple t tests); **p<0.01, *p<0.05.

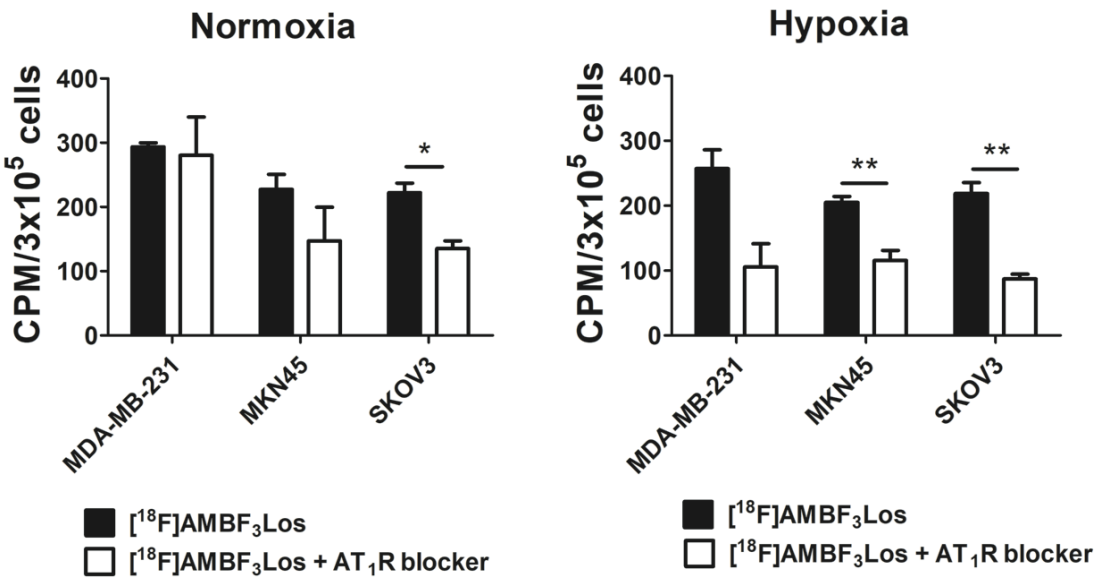

Source: thesis author.

Overall these data demonstrate that [^{18}F]AMBF$_3$Los has a better AT$_1$R binding affinity compared to [^{18}F]FEtLos, and suggest that the cancer cells tested have a low AT$_1$R protein expression level, unlike expected.

5.4 *In vivo* assays

5.4.1 µPET/CT imaging and autoradiography in healthy mice

Since kidneys are physiologically AT$_1$R-rich organs, we then aimed to evaluate the *in vivo* binding specificity of the new derivatives [^{18}F]FEtLos and [^{18}F]AMBF$_3$Los to renal AT$_1$R in healthy mice. It was previously reported that losartan derivatives presented the highest renal uptake at early time points after injection in rats: 10-15 min (Arksey *et al.*, 2014; Ismail *et al.*, 2015). Therefore, renal AT$_1$R binding specificity of [^{18}F]FETLos was evaluated by an *ex vivo* µPET/CT imaging of the mice kidneys 10 min post tracer injection. Our results showed an increased renal [^{18}F]FETLos uptake (baseline), which was blocked

when losartan potassium (AT_1R blocker) was co-injected with [^{18}F]FETLos (Figure 25A and B). Interestingly, [^{18}F]FETLos uptake was mainly observed in the renal medulla instead of the cortex.

Figure 25 – (A) Representative *ex vivo* µPET/CT imaging (coronal view) of Balb/c Nude mice kidneys 10 minutes after [^{18}F]FEtLos intravenous injection in the absence (baseline) or presence of losartan potassium (AT_1R blocked). Quantification of [^{18}F]FEtLos %ID/g in kidneys is presented in graph (B). The blocking effect was analyzed using the one unpaired t-test (multiple t tests); *p<0.05. LK: left kidney; RK: right kidney.

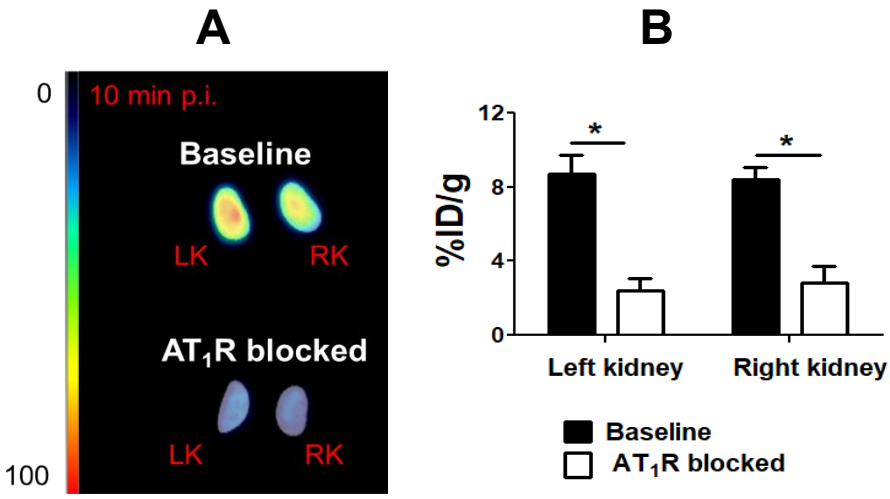

Source: thesis author.

On the other hand, the renal AT_1R binding specificity of [^{18}F]AMBF$_3$Los was evaluated in NOD.Cg-*Prkdc*^{scid}*Il2rg*^{tm1Wjl}/SzJ mice with a 60-min dynamic µPET scan followed by autoradiography. As shown in Figure 26A, there was a high renal [^{18}F]AMBF$_3$Los uptake at early time points (Figure 26A), which was reduced when losartan potassium (AT_1Rblocker) was co-injected with [^{18}F]AMBF$_3$Los (Figure 26B). Unlike [^{18}F]FEtLos, the uptake of [^{18}F]AMBF$_3$Los was observed on the kidney cortex rather than medulla. These results were similar to the ones reported Arksey *et al.*, using the analog [^{18}F]FPyKYNE-losartan (Arksey *et al.*, 2014). The µPET images also showed a fast clearance of [^{18}F]AMBF$_3$Los from most of the mouse tissues. For example, a high [^{18}F]AMBF$_3$Los uptake was found in the liver at early time points, which markedly decreased 25-30 min p.i. In addition, the time-activity curves (TAC) showed that the most of the tracer uptake occurred within the first few minutes, and the activity was slowly washed out (Figure 26C). However, the TACs did not showed significant differences between

baseline and AT_1R blocked possibly due to the small number of animals per group (n=3), or a low dose of the AT_1R blocker losartan potassium (18 mg/kg).

Figure 26 – Representative frames of the dynamic PET imaging (coronal view, 0-10% ID/g) with [^{18}F]$AMBF_3$Los in healthy NOD.Cg-*Prkdc*^{scid}*Il2rg*^{tm1Wjl}/SzJ mice of the baseline (A) and AT_1R blocked (B) groups. The images showed a high tracer uptake by the renal cortex 5-15 minutes post-injection, and a decreased [^{18}F]$AMBF_3$Los uptake when the AT_1R blocker losartan (18 mg/kg) was co-injected. C. The time-activity curves obtained from the dynamic PET data at baseline (n=3) and AT_1R blocked (n=3) groups.

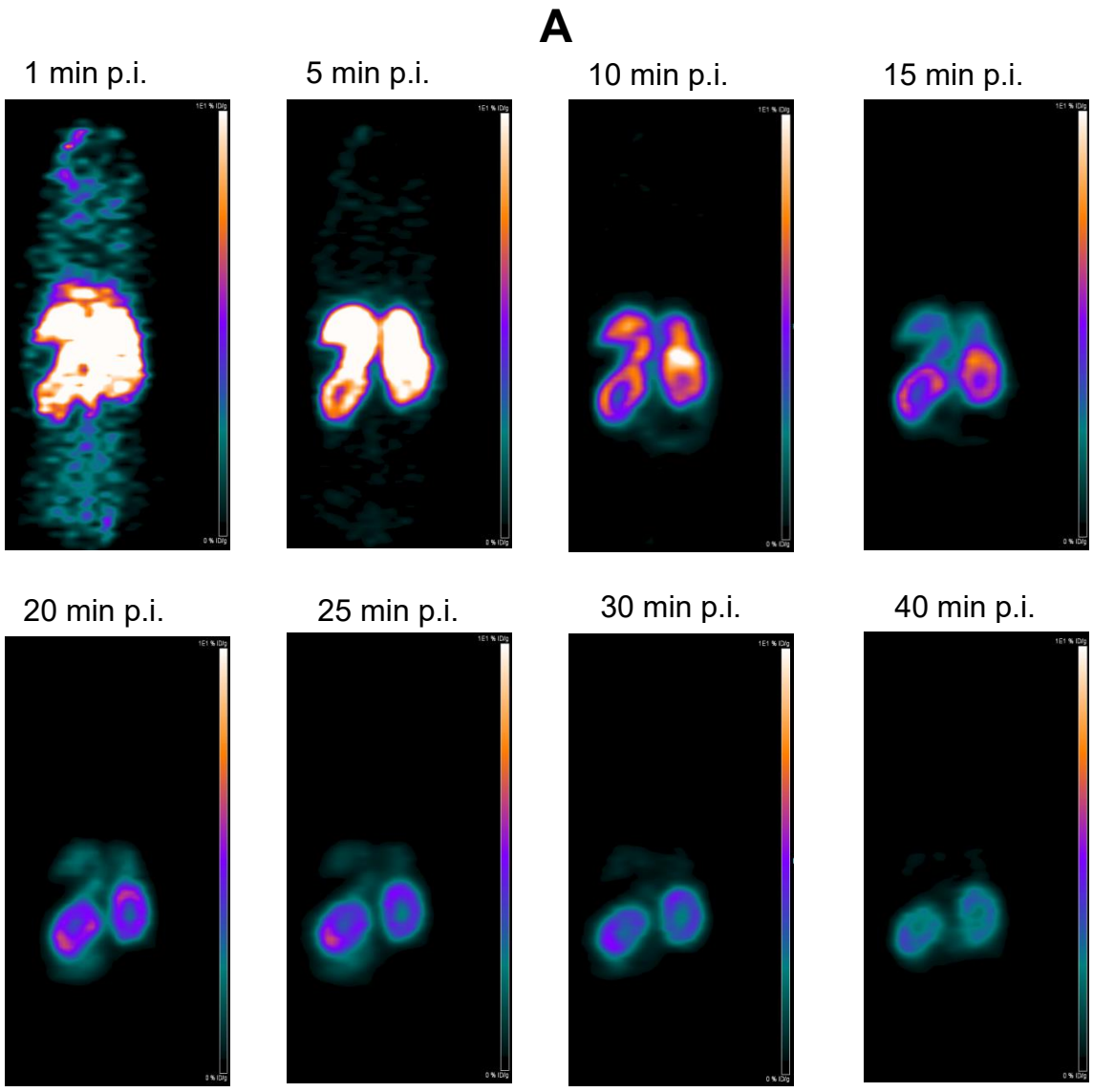

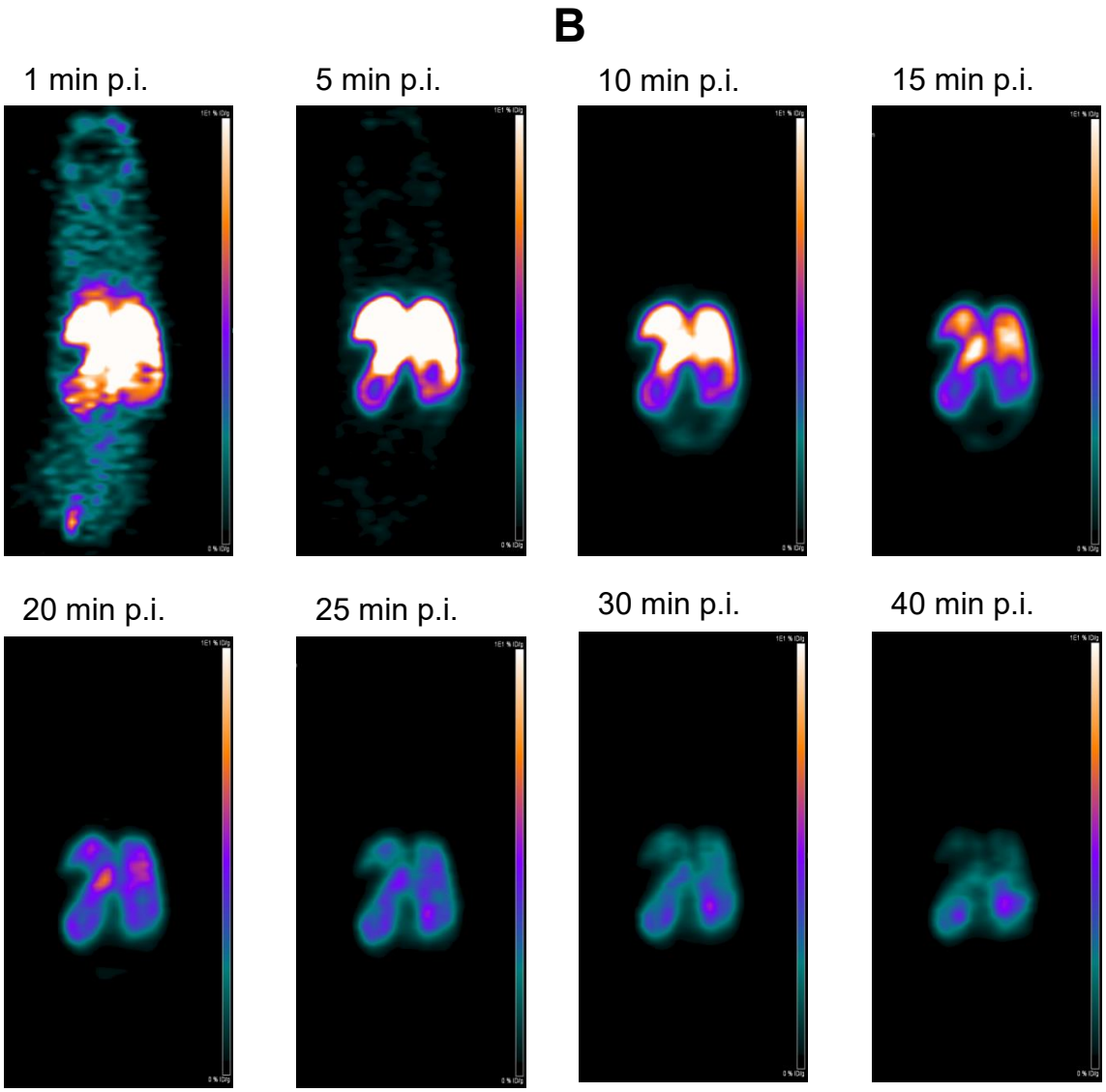

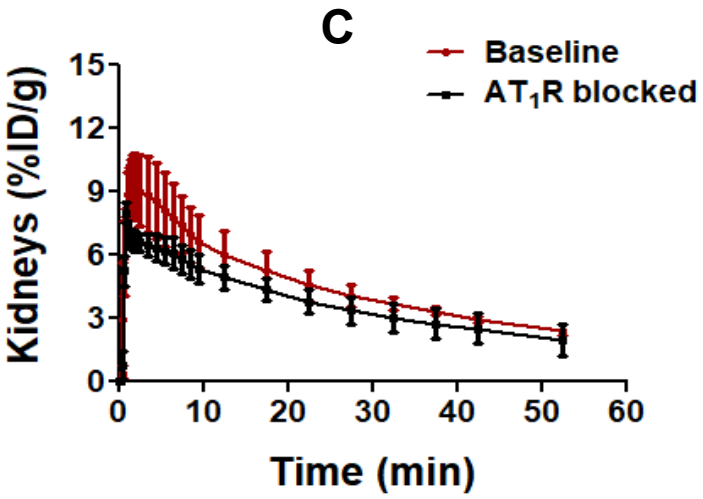

Source: thesis author.

Autoradiographic studies were performed after the 60-min dynamic PET scans and we confirmed that [^{18}F]AMBF$_3$Los was mainly captured on kidney cortex, and this uptake was blocked by the co-injection of losartan potassium (Figure 27). The renal cortex activity was approximately 5-times smaller in the mouse kidney blocked with losartan potassium.

Figure 27 – Representative autoradiographic images of kidneys from healthy NOD.Cg-*Prkdc*^{scid}*Il2rg*^{tm1Wjl}/SzJ mice after the 60-min dynamic PET scan with [^{18}F]AMBF$_3$Los (baseline) and [^{18}F]AMBF$_3$Los + losartan potassium (AT$_1$R blocked group). The images showed a reduced signal in the kidney cortex when AT$_1$R was blocked with losartan potassium (18 mg/kg).

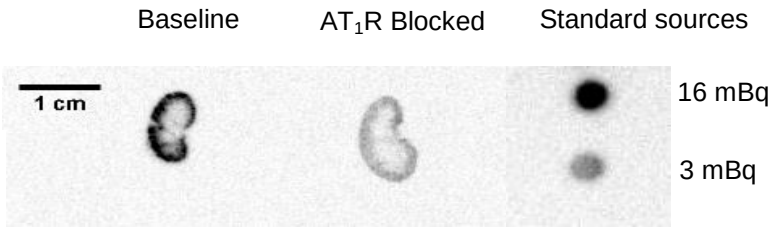

Source: thesis author.

These findings suggested that [^{18}F]FEtLos and [^{18}F]AMBF$_3$Los are specific radioligands for renal AT$_1$R.

5.4.2 µPET/CT imaging in tumor-bearing mice

We then evaluate whether [^{18}F]AMBF$_3$Los was able to image AT$_1$R-expressing tumors *in vivo* by µPET/CT scan. Four tumor-bearing mouse models were tested: tumor derived from MKN45 (Figure 28), SKOV3 (Figure 29), MDA-MB-231 (Figure 30) or MCF7 (Figure 31) cells, all positive for AT$_1$R expression. Unfortunately, 60 min after tracer injection, no signal was found in the tumor in none of the groups. Static µPET/CT imaging at this time point only exhibited [^{18}F]AMBF$_3$Los uptake in the intestines and gallbladder (Figures 28-31).

Figure 28 – Representative static µPET/CT imaging of MKN45 gastric tumor-bearing mice after 60 minutes of intravenous [^{18}F]AMBF$_3$Los injection.

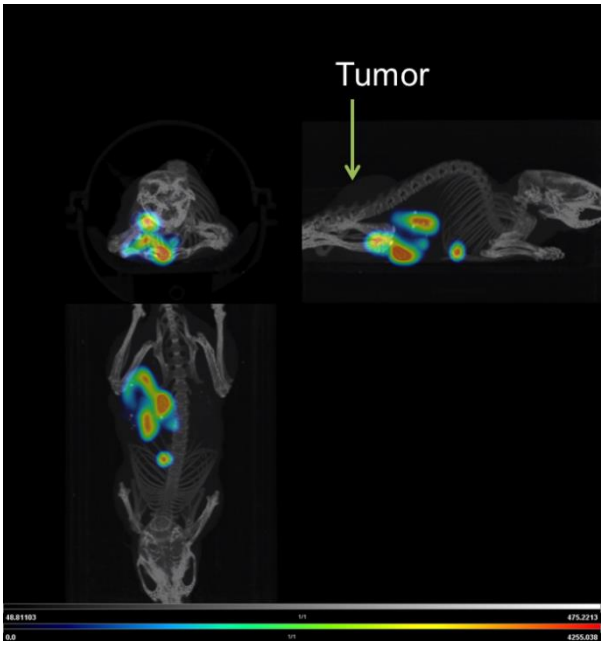

Source: thesis author.

Figure 29 – Representative static µPET/CT imaging of SKOV3 ovarian tumor-bearing mice after 60 minutes of intravenous [^{18}F]AMBF$_3$Los injection.

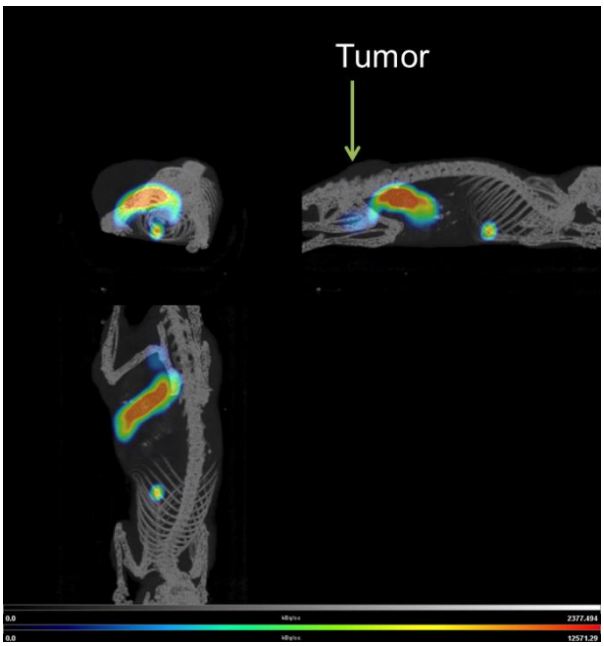

Source: thesis author.

Figure 30 – Representative static µPET/CT imaging of MDA-MB-231 breast tumor-bearing mice after 60 minutes of intravenous [^{18}F]AMBF$_3$Los injection.

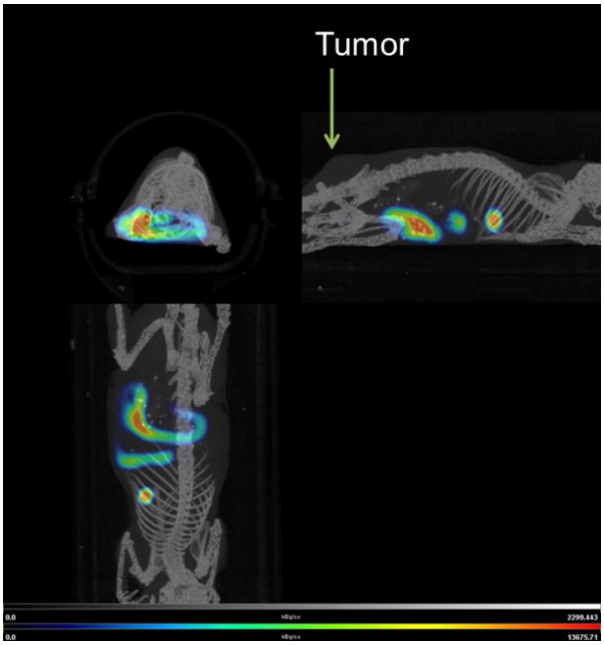

Source: thesis author.

Figure 31 – Representative static µPET/CT imaging (coronal view) of MCF7 breast tumor-bearing mice after 60 minutes of intravenous [^{18}F]AMBF$_3$Los injection. No tumor uptake was found at the baseline and in AT$_1$R blocked (20 mg/kg of losartan potassium) groups.

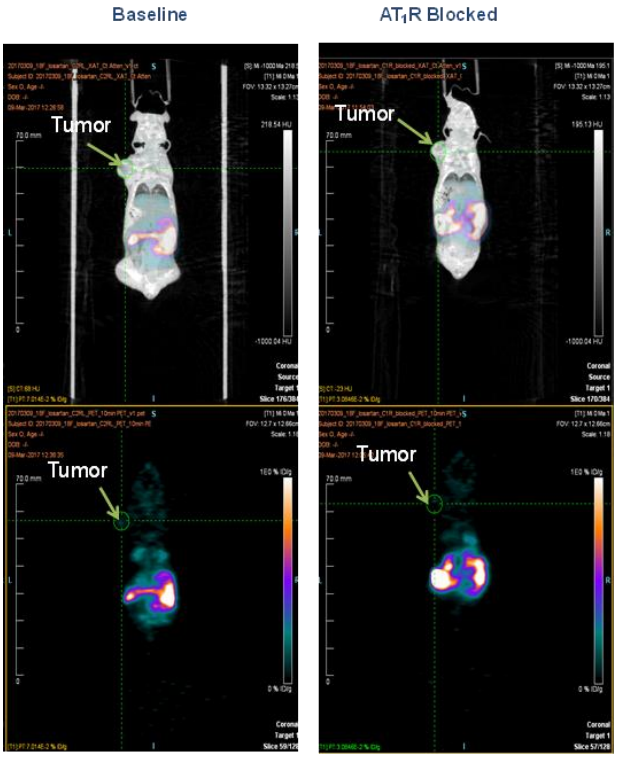

Source: thesis author.

5.4.3 *Ex vivo* biodistribution studies in tumor-bearing mice

The *ex vivo* biodistribution studies were then performed in MKN45 (Figure 32), SKOV3 (Figure 33), MDA-MB-231 (Figure 34) or MCF7 (Figure 35) tumor-bearing mice to quantify tissue uptake of [^{18}F]AMBF$_3$Los. However, 60 min after the intravenous tracer injection no uptake was found in the tumor and kidneys of all studied groups. Intestines, gallbladder and bladder displayed the highest uptake at this time point, suggesting that [^{18}F]AMBF$_3$Los was rapidly excreted via hepatobiliary and renal pathways. When losartan potassium (20 mg/kg) was co-injected with [^{18}F]AMBF$_3$Los, a significant decrease of tracer uptake was found in the intestines (Figure 35).

Figure 32 – *Ex vivo* biodistribution of [^{18}F]AMBF$_3$Los in MKN45 gastric tumor-bearing mice after 60 minutes of intravenous injection (baseline group). Graph shows the mean ± SD (n=5). Data were analyzed using one-way ANOVA (Dunnett´s multiple comparisons test compared to blood); * p<0.05, ** p<0.01.

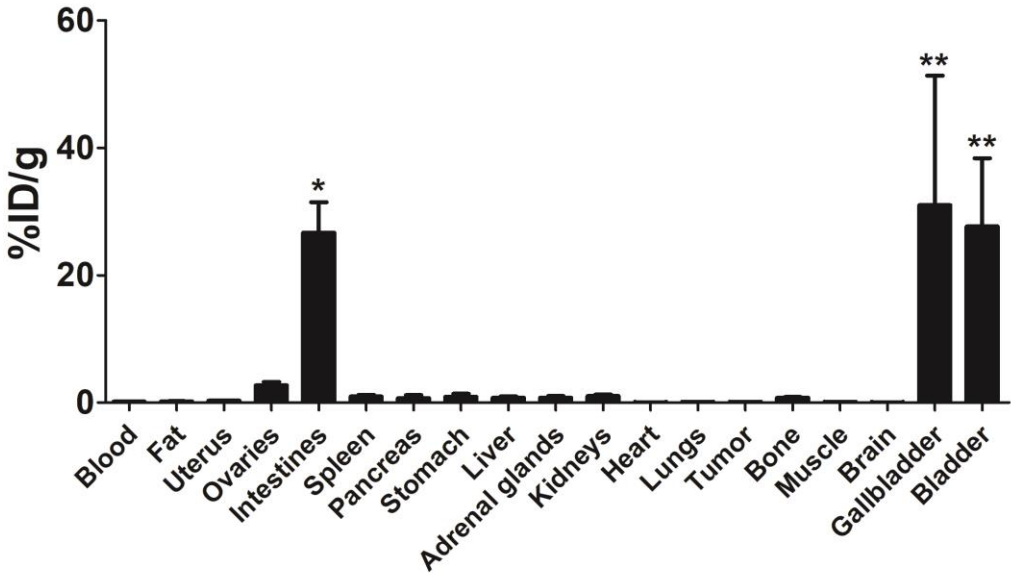

Source: thesis author.

Figure 33 – *Ex vivo* biodistribution of [^{18}F]AMBF$_3$Los in SKOV3 ovarian tumor-bearing mice after 60 minutes of intravenous injection at baseline group. Graph shows the mean ± SD (n=5). Data were analyzed using one-way ANOVA (Dunnett´s multiple comparisons test compared to blood); **** p<0.0001.

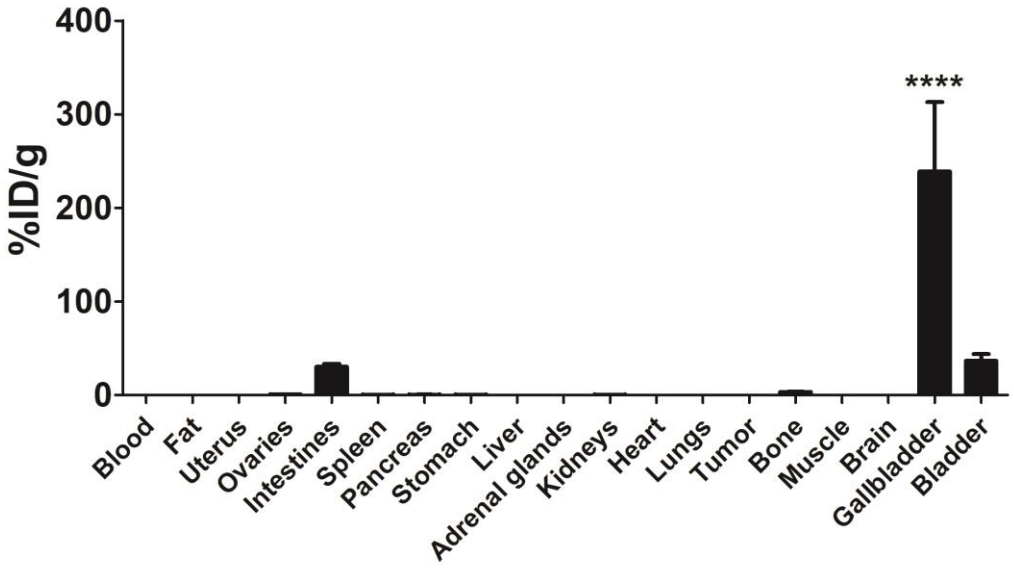

Source: thesis author.

Figure 34 – *Ex vivo* biodistribution of [^{18}F]AMBF$_3$Los in MDA-MB-231 breast tumor-bearing mice after 60 minutes of intravenous injection (baseline group). Graph shows the mean ± SD (n=4). Data were using one-way ANOVA (Dunnett´s multiple comparisons test compared to blood); ** p<0.01, **** p<0.0001.

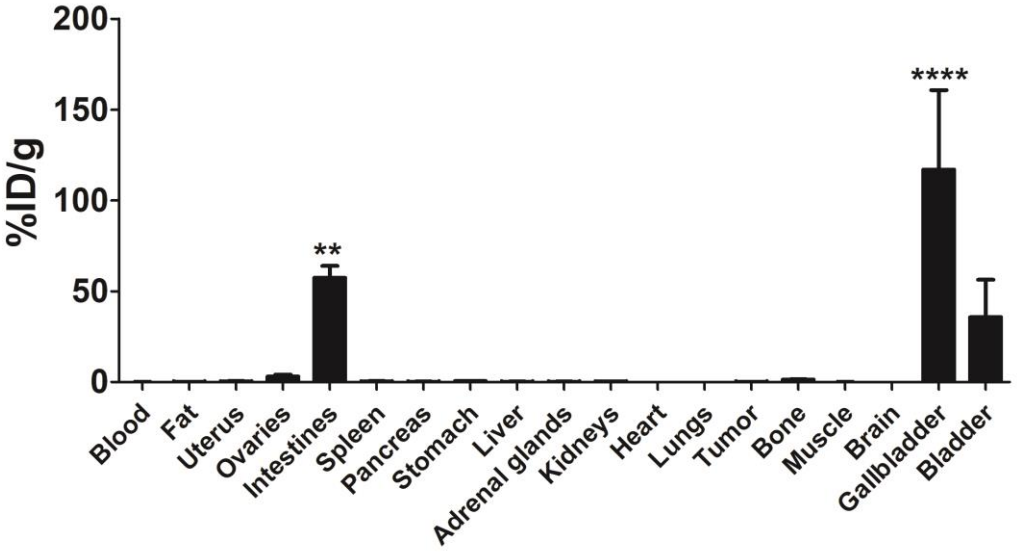

Source: thesis author.

Figure 35 – *Ex vivo* biodistribution of [^{18}F]AMBF$_3$Los in MCF7 breast tumor-bearing mice 60 min after intravenous injection. Baseline group are black bars, (n=4) and AT$_1$R blocked are white bars, (n=3). Graph shows the mean ± SD and data were analyzed using one-way ANOVA (Dunnett´s multiple comparisons test) to analyze the individual effect of each tissue compared to blood, and one unpaired t-test (multiple t tests) to analyze the AT$_1$R blocking effect; **** p<0.0001; * p<0.05.

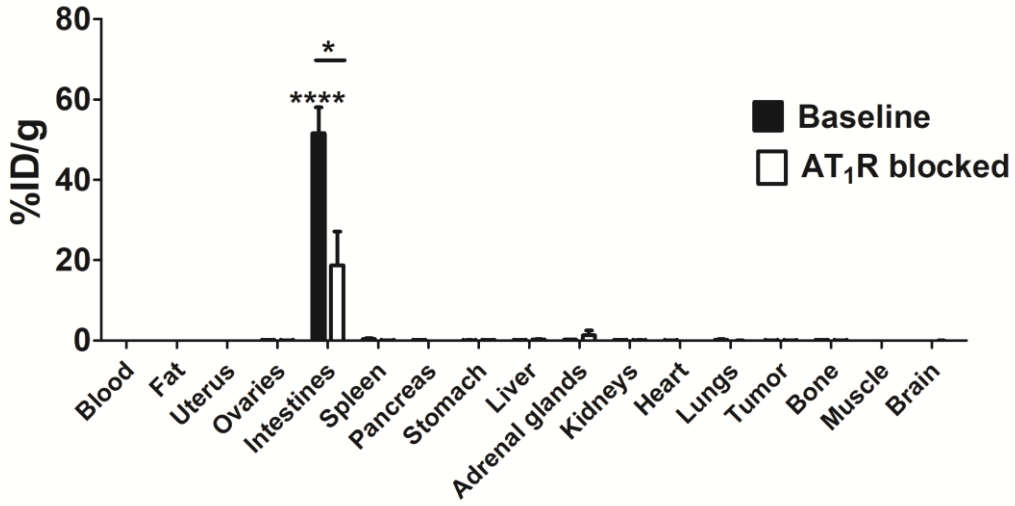

Source: thesis author.

5.4.4 *Ex vivo* biodistribution studies and µPET/CT imaging after intratumoral injection

To further evaluate [^{18}F]FEtLos and [^{18}F]AMBF$_3$Los binding specificity to tumoral AT$_1$R, we performed a direct intratumoral injection of both radioligands (in the presence or absence of cold losartan) in MDA-MB-231 breast tumor-bearing mice and evaluated tumor tissue uptake by *ex vivo* biodistribution studies. Sixty minutes p.i., [^{18}F]FEtLos showed a tumor uptake of 40% (baseline) and co-injection with losartan potassium (AT$_1$R blocker) did not block the radiotracer uptake (Figure 36). [^{18}F]FEtLos displayed a significant uptake in the gallbladder and bladder, sugesting an hepatobiliar and renal excretion pathways. Overall, these data suggest that [^{18}F]FEtLos is not a suitable PET radioligand for AT$_1$R-expressing tumor microenvironment since it did not show any specific AT$_1$R binding for MDA-MB-231 breast cancer or CHO-AT1R non-cancer cells (Figure 21B) which is in agreement with the low Ki value (Figure 19).

Figure 36 – *Ex vivo* biodistribution of [^{18}F]FEtLos in MDA-MB-231 breast tumor-bearing mice 60 min after intratumoral injection. Baseline group are black bars, (n=4) and AT_1R blocked (70 mg/kg) are white bars, (n=3). Graph shows the mean ± SD (n=3) and data were analyzed by one unpaired t-test, * p<0.05, *** p<0.001.

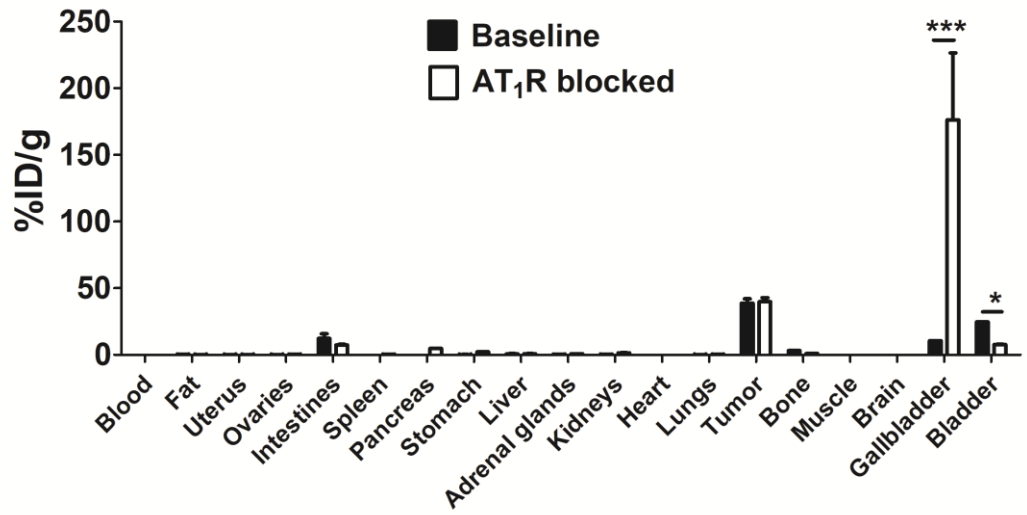

Source: thesis author.

On the other hand, when [^{18}F]AMBF$_3$Los was injected intratumorally in MDA-MB-231 breast cancer-bearing mice, the ex-vivo biodistribution studies obtained 60 min p.i. showed a high tumor uptake (%ID/g ~ 80 %) that was significantly reduced (to a %ID/g ~ 20%) by the co-injection of losartan potassium (AT_1R blocker) (Figure 37). In addition, static µPET/CT imaging showed a high activity concentration in tumor 60 minutes after intratumoral injection (baseline) that was significantly reduced by the co-injection of losartan potassium (AT_1R blocker) (Figure 38). These findings suggested that although [^{18}F]AMBF$_3$Los is specific for tumor AT_1R binding, because of its very short time in the bloodstream, it may not reach the tumor when injected intravenously.

Figure 37 – *Ex vivo* biodistribution of [^{18}F]AMBF$_3$Los in MDA-MB-231 breast tumor-bearing mice 60 min after intratumoral injection. Baseline group are black bars, (n=4) and AT$_1$R blocked (70 mg/kg) are white bars, (n=3). Graph shows the mean ± SD (n=3) and data were analyzed by one unpaired t-test, ** p<0.01.

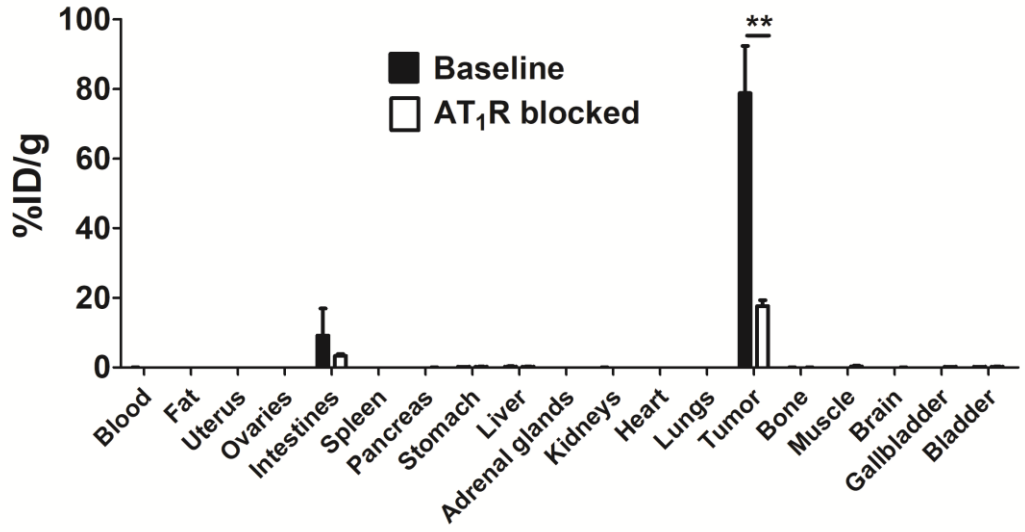

Source: thesis author.

Figure 38 – Representative static µPET/CT imaging (transverse view) of MDA-MB-231 breast tumor-bearing mice 60 minutes after the intratumoral injection of [^{18}F]AMBF$_3$Los. The image shows a high tumor uptake at the baseline, and notable tumor uptake reduction in the AT$_1$R blocked group.

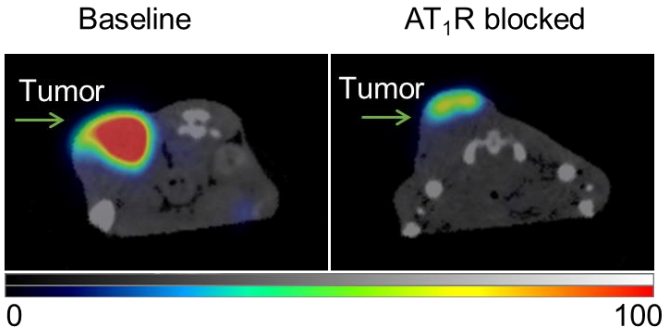

Source: thesis author.

5.4.5 Blood clearance

Finally, the half-life of [^{18}F]AMBF$_3$Los in blood circulation was determined in MKN45, SKOV3, and MDA-MB-231 tumor-bearing mice. The results showed that [^{18}F]AMBF$_3$Los displays a very fast blood clearance of 0.76 min (46 seconds) for MKN45 (Figure 39A) and SKOV3 (Figure 39B) tumor-bearing mice, and 0.91 min (55 seconds) for the MDA-MB-231 group (Figure 39C).

Figure 39 – Blood clearance of [^{18}F]AMBF$_3$Los in MKN45 (A), SKOV3 (B), and MDA-MB-231 (C) tumor-bearing mice. Data are representative of n=3 and the half-life was calculated by fitting to one phase decay curve.

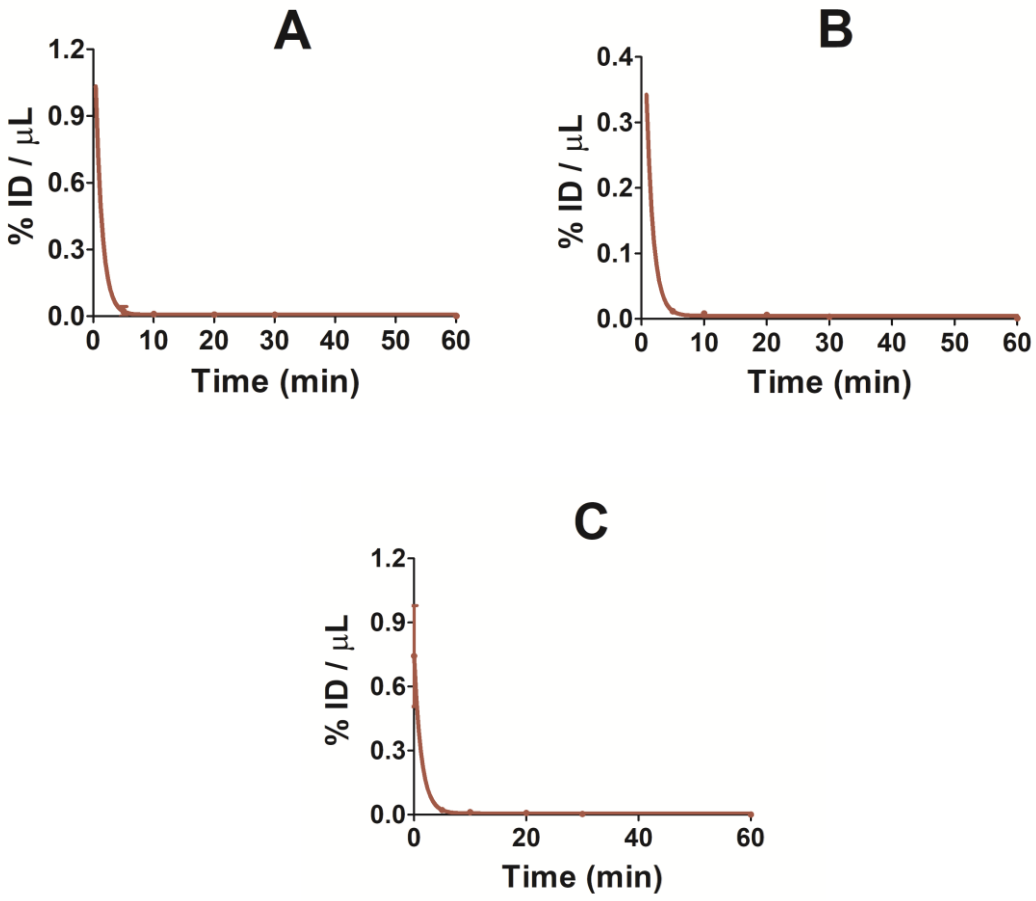

Source: thesis author.

In summary, we showed in this thesis for the first time that [^{18}F]AMBF$_3$Los, a new AT$_1$R PET radioligand, binds specifically to AT$_1$R-expressing tumor cells *in vitro* and displays a high tissue uptake in the kidney cortex of mice. When injected intratumorally, [^{18}F]AMBF$_3$Los was found to bind specifically to tumor xenograft and was competitively inhibited by cold losartan. However, [^{18}F]AMBF$_3$Los was not able to reach the tumor site once injected

intravenously probably because of its rapid metabolism and very fast clearance. Nonetheless our results demonstrate that ^{18}F- ARBs derivatives could be suitable tracers to cancer imaging AT_1R-expressing tumor microenvironment, however, radiolabeled ARBs that possess better pharmacokinetics profile may be required.

6 DISCUSSION

Many PET tracers have been developed using the [^{18}F]fluoroalkylating agent [^{18}F]FEtOTs since its first reported radiosynthesis in 1987 (Block *et al.*, 1987; Kniess *et al.*, 2015). [^{18}F]FEtOTs has been prepared by nucleophilic ^{18}F-substitution on the ethylene glycol bistosylate precursor at different labeling temperatures and reaction times varying mostly from 70 to 130 ^{o}C and 3 to 15 minutes, respectively, with 30% - 90% radiochemical yields (Kniess *et al.*, 2015). According to the literature, the formation of a radioactive gas as side-product during the radiosynthesis of [^{18}F]FEtOTs has not been reported yet. However, the formation of an unknown volatile radioactive side-product during the [^{18}F]fluoroalkylation reaction using [^{18}F]FEtOTs as a [^{18}F]fluoroalkylating agent was mentioned previously (De Vries *et al.*, 2003). These authors suggested that [^{18}F]vinyl fluoride might have been formed through the β-elimination of [^{18}F]FEtOTs (De Vries *et al.*, 2003). The indirect ^{18}F-radiolabeling using the prosthetic group [^{18}F]FEtOTs usually involves high temperatures and strong basic medium that may favor elimination over substitution mechanisms. The radiolabeling reaction with [^{18}F]F^{-} to prepare the [^{18}F]FEtOTs also proceeds at high temperatures and basic medium, which might have enhanced the formation of the gas [^{18}F]vinyl fluoride. In addition, the nucleophile [^{18}F]F^{-} can also act as a base, inducing the elimination mechanism. According to our results, a radioactive gas was formed during the radiosynthesis of [^{18}F]FEtOTs, which may lead to radioactive contamination if lab conditions are inadequate or handling procedures are misguidedly performed. Therefore, the radiosynthesis of [^{18}F]FEtOTs was optimized (temperature, time and amount of base) in order to afford [^{18}F]FEtOTs and reduce the formation of volatile radioactive side-products as much as possible.

Temperature and reaction times mainly influenced the formation of a radioactive gas. The reaction conditions of 100 ^{o}C and 1 min in sealed vials provided a safer manual radiosynthesis with high HPLC crude yields of [^{18}F]FEtOTs. This product is quickly formed at 100 ^{o}C and both labeling temperature and reaction time, varying from 70 to 130 ^{o}C and 3 to 15 min respectively, significantly enhanced the formation of the radioactive gas at 95% confidence. However, the increased amount of base did not favor the formation of the radioactive gas. The best crude yields of [^{18}F]FEOTs (80 ± 4%) with a low formation of the radioactive gas (6 ± 2%) were reached at the labeling conditions:100 ^{o}C and 1 minute. At the same time, HPLC profiles at 2 and 5 mg of K_2CO_3 exhibited a formation of the^{18}F-labeled side-product with a retention time of 2.7 minutes approximately in a K_2CO_3-dependent way, which might be 2-[^{18}F]fluoroethanol due to the basic reaction conditions as mentioned by other reports (Tietze *et al.*, 2006).

In conclusion, the formation of radioactive gas is expected both during the radiosynthesis of [^{18}F]FEtOTs and the following [^{18}F]fluoroalkylation reaction. Therefore, both radiosynthesis must always proceed in radioisotope fume hoods or hot cells with excellent exhaustion and radioactivity trapping. In effect, the formation of a radioactive gas was also recorded when the [^{18}F]fluoroethylation of losartan was performed with >3.7GBq activities of [^{18}F]FEtOTs, using the strong base NaH, and heating at 80 ^{o}C for 20 min.

Two new Angiotensin II receptor Blockers [$^{19/18}$F]FEtLos and [$^{19/18}$F]AMBF$_3$Los were designed, synthetized and evaluated as novel AT_1R radioligands for PET imaging of AT_1R-positive tumors. Both compounds were designed via substitution of the hydroxyl group by fluoro ligands at imidazole 5-position of losartan. Several substituents with different length such as a small methyl group (Hadizad *et al.*, 2011) and a bulky side chain (Verjans *et al.*, 2008), have been introduced into the losartan pharmacophore at the same position, without reducing the AT_1R binding affinity. For instance, the chelate-coupled losartan-Leucine-Diglycoloyl-Tetraethyleneglycol-Tetraamine showed superior AT_1R affinity (Ki = 60 pM) compared to parental losartan (Ki = 10 nM); radiolabeling of this compound with ^{99m}Tc displayed an acceptable biodistribution profile in mouse model of post-myocardial infarction heart failure (Verjans *et al.*, 2008). The increase of AT_1R affinity of this losartan analog is probably due to the

higher possibility to form hydrogen bonds, which may increase their affinity to the receptor (Figure 40). Other losartan derivatives were synthesized by adding nitric oxide (NO)-donor side chains to losartan at imidazole 5-position as well (Figure 41), and all of them displayed antagonist potency values similar to losartan (Breschi *et al.*, 2004). The [^{18}F]FPyKYNE-losartan derivative also showed high affinity to kidney AT_1R in rats and pigs (Hachem *et al.*, 2016).

Figure 40 – Structure of the chelate-coupled losartan-Leucine-Diglycoloyl-Tetraethyleneglycol-Tetraamine for radiolabeling with ^{99m}Tc and SPECT imaging in cardiology

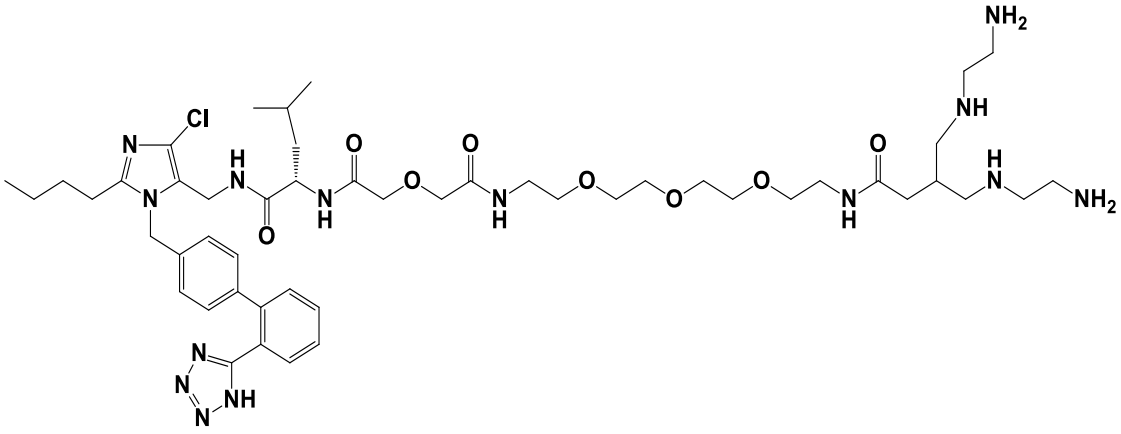

Source: (Verjans *et al.*, 2008).

Figure 41 – Structure of the NO-releasing derivatives of losartan as cardiovascular drugs with vasorelaxing effects and AT_1R-antagonist activity

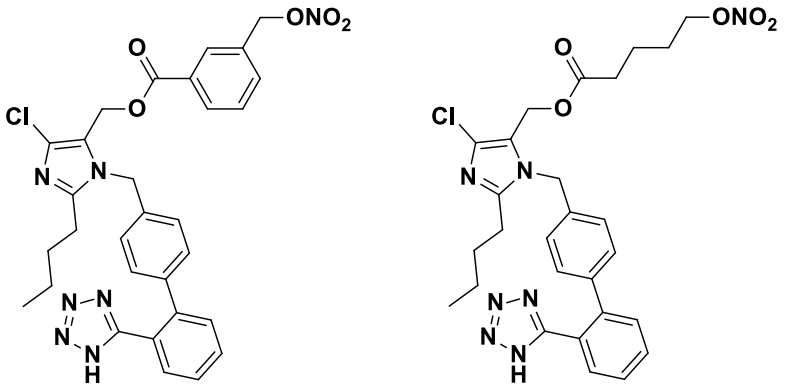

Source: modified from literature (Breschi *et al.*, 2004).

[^{18}F]FEtLos and the cold FEtLos were synthetized by both [$^{18/19}$F]fluoroethylation of losartan potassium and tetrazole-protected losartan through a SN2 reaction. The regioisomer with the substitution at the imidazole 5-position was obtained with higher yield due to the localized negative charge on oxygen atom in contrast to the delocalized negative charge at the tetrazol moiety,

which is stabilized by resonance. We also put some efforts in synthetizing a precursor for direct ^{18}F-labeling, however we did not achieve successfully results. On this regard, it is worth mentioning that the reaction of tetrazole-protected losartan with ethylene glycol bistosylate failed when we tested three different bases: NaH, K_2CO_3 and sodium ethoxide (NaOEt), either at room temperature / 80 ^{o}C up to 24 h, or microwaves radiation (80 ^{o}C for 5 min, 300 watts). The reaction color varied from yellow to dark brown with the strong base NaH, and TLC results always showed the presence of the starting material and the consumption of ethylene glycol bistosylate without forming UV-visible products. The formed products obtained with NaOEt were not the expected ones, and no product was observed when using the weaker base K_2CO_3.

On the other hand, the cold AMBF_3Los was synthetized via a copper (I) - catalyzed Huisgen alkyne - azide 1,3-dipolar cycloaddition, the most used click reaction, and the ^{18}F-labeled compound was obtained from an aqueous ^{18}F-^{19}F isotopic exchange reaction. The one step ^{18}F-^{19}F isotopic exchange approach using organotrifluoroborates is like a kit for ^{18}F-labeling. This approach was successfully used for radiolabeling peptides and smaller molecules within 40 min, obtained with radiochemical purity greater than 95%, without further HPLC purification and in high molar activities ranging from 24 to 207 GBq/µmol. All these radiosynthesis started with ≥ 3.7 GBq of [^{18}F]F^{-} (Liu, Pourghiasian, Bénard*, et al.*, 2014; Lau *et al.*, 2015; Pourghiasian *et al.*, 2015; Gonçalves Nunes *et al.*, 2018; Huang *et al.*, 2018).

The AMBF_3-alkynyl (**6**) was prepared according to the literature by alkylating the tertiary amine N,N-dimethylpropargylamine with iodomethyl-pinacol boronate, followed by the fluorination reaction with mildly acidic KHF_2 (Liu, Pourghiasian, Radtke*, et al.*, 2014; Liu *et al.*, 2015). The fluorination mechanism is represented in Figure 42 and involves a one-pot two-step reaction: (1) acid catalyzed hydrolysis of the boronic ester to boric acid and (2) conversion of the boric acid to trifluoroborate (Lin *et al.*, 2019).

Figure 42 – Reaction mechanism to synthetize the $AMBF_3$-alkynyl (**6**)

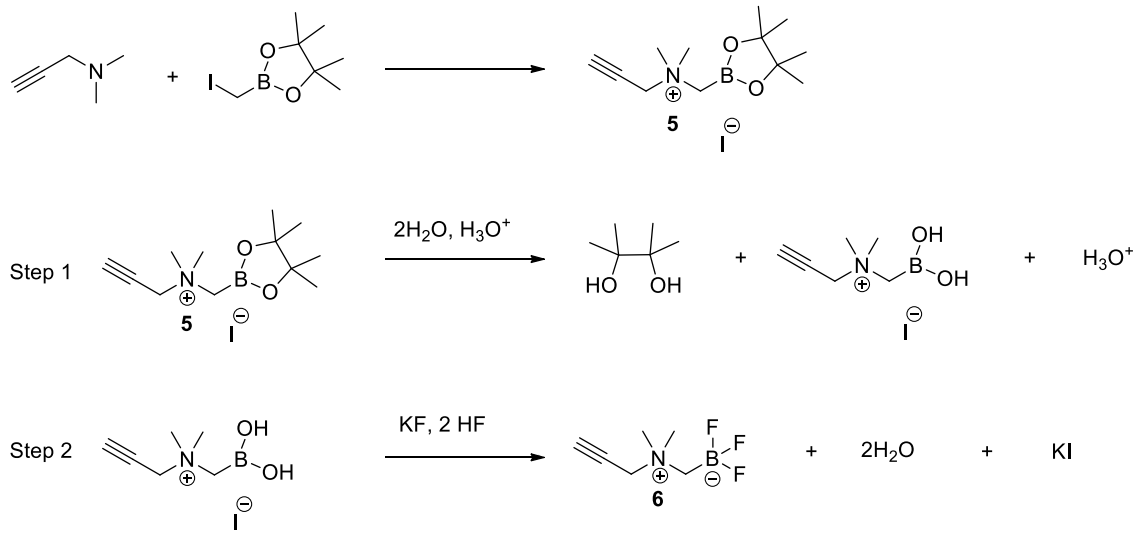

Source: modified from literature (Lin *et al.*, 2019).

The alcohol to azide conversion at the imidazole 5-position of losartan took place by a SN2 inversion following a Mitsunobu displacement with the azide nucleophile. The mechanism for converting the alcohol moiety to the corresponding azide initially involves the formation of the phosphate of the alcohol and the DBU salt; then, the phosphate leaving group is displaced by the organic soluble form of azide at ambient temperature (Thompson *et al.*, 1993; Thompson and Grabowski, 1995). The DBU salt of diphenyl phosphate is also formed, and can be removed with an aqueous wash (Thompson *et al.*, 1993; Thompson and Grabowski, 1995). This method allows getting the azide product in high yield (60-95 %) and enantiomeric purity, which can be used to produce azides from the corresponding benzylic alcohols or alpha hydroxyl alkane esters (Thompson and Grabowski, 1995). The reaction mechanism for converting alcohol into azide at losartan is represented in Figure 43. We also used tetrazole-protected losartan (**3**) as precursor for avoiding formation of side-products due to deprotonation of tetrazole moiety at losartan commercially available.

Figure 43 – Reaction mechanism to introduce the azide function at the losartan molecule

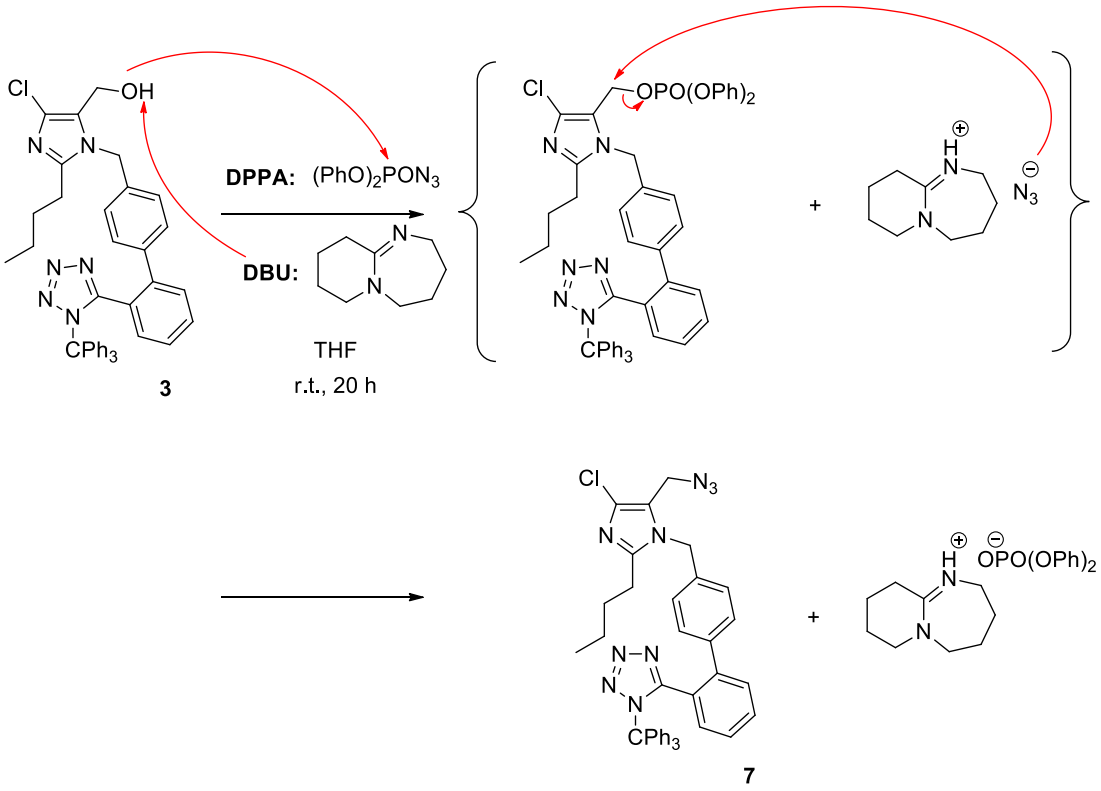

Source: thesis author.

Trityl protecting group was then removed under acidic conditions before proceeding to the click reaction for avoiding trifluoroborate hydrolysis at the $AMBF_3$-conjugated losartan. The cold $AMBF_3$Los was finally afforded in similar yield to other compounds using the same approach (Lau *et al.*, 2015; Pourghiasian *et al.*, 2015).

The radiochemical yield of [^{18}F]$AMBF_3$Los was low due to a significant part of the [^{18}F]F^- was lost by volatilization as [^{18}F]HF during the ^{18}F-^{19}F isotopic exchange reaction, which is performed in acidic conditions under vacuum and heating. According to the literature, the reaction pH is the crucial step of this radiolabeling approach, and a pH of 2-2.5 generally gives lower by-product (boronic acid) levels, and better radiochemical yield (Liu *et al.*, 2015). The carrier [^{19}F]fluoride was used during the radiolabeling because it increases the [^{18}F]BF_3 formation while still providing a molar activity of 37 GBq/µmol (Lin *et al.*, 2019).

In addition, log $D_{7.4}$ measurements of [^{18}F]FEtLos (0.2) and [^{18}F]$AMBF_3$Los (-0.4) showed that these new derivatives are more hydrophilic than the parental losartan with a log $D_{7.4}$ of 1.7 (Kalgutkar and Daniels, 2010).

Therefore less non-specific liver uptake is expected compared to the [^{18}F]FPyKYNE-losartan.

Nonetheless, results of the *in vitro* competition binding assays showed that only the derivative AMBF$_3$Los (Ki = 7.9 nM) displayed a good binding affinity to human AT$_1$R. The high Ki value (2.2 µM) of FEtLos reveals that FEtLos has a low binding affinity for AT$_1$R. Therefore, the substitution of hydroxyl group by the 2-fluoroethoxy moiety substantially affected the AT$_1$R binding due to the lack of hydrogen bonding or other intermolecular forces. In case of AMBF$_3$Los, the 1,2,3-triazole is a polar moiety and a good hydrogen bond acceptor that may keep the receptor binding affinity of the modified losartan. The derivative [^{18}F]FPyKYNE-losartan, also containing a 1,2,3-triazole at the imidazole 5-position, displayed high affinity (dissociation constant = 49.4 nM) to rat kidney AT$_1$R (Hachem *et al.*, 2016). The structure-activity relationships at the imidazole 5-position revealed that it generally prefers small hydrogen-bonding substituents such as alcohols or carboxylic acids but also tolerates a wide range of functional groups (Carini *et al.*, 1991). Thus, our results corroborate data from the literature showing that hydrogen-bonding substituents at the imidazole 5-position also play an important role to the AT$_1$R binding affinity.

For the biological evaluation of the new derivatives in cancer models, the AT$_1$R mRNA abundance was firstly confirmed by RT-PCR on several cells and derived tumors. As AT$_1$R is physiologically localized on vascular smooth muscle cells to mediate vasoconstriction (Paul *et al.*, 2006), the increased AT$_1$R mRNA abundance on tumors was expected because of tumor vascularization. In particular, we hypothesize that the great increase of the AT$_1$R mRNA abundance on MKN45-derived tumor compared to MKN45 cell culture is probably due to the hypoxic condition. Hypoxia promotes vessel growth to deliver oxygen and nutrients by upregulating multiple angiogenic factors such as extracellular matrix degradation and vascular permeability (Krock *et al.*, 2011). In addition, we confirmed that MKN45 tumors are hypoxic because of the tumor uptake of [^{18}F]Fluoroazomycin arabinoside ([^{18}F]FAZA), a hypoxia PET tracer (unpublished data from our research group). On the other hand, AT$_1$R mRNA expression levels were significantly increased in human lung fibroblast (HLF-1) cells after 24 hrs of hypoxic treatment (Liu *et al.*, 2013). These authors found that hypoxia induced the mRNA expression of other RAS components (angiotensinogen and ACE) in HLF-1

cells and increased ANG II levels (Liu *et al.*, 2013). ANG II, ACE and AT_1R were also up-regulated in mouse Lewis lung carcinoma (LLC) cells after 24 hrs of hypoxia exposure (Fan *et al.*, 2014). Since hypoxia can regulate a local RAS as well, we expected a higher tracer uptake by the cancer cells cultured under hypoxia. Nevertheless, AT_1R-positive MDA-MB-231, SKOV3 and MKN45 cells did not show a substantial [^{18}F]AMBF$_3$Los uptake at normoxic nor at hypoxic conditions. In contrast, CHO-AT1R cells displayed high [^{18}F]AMBF$_3$Los uptake and extremely significant AT_1R blockade at normoxia. The low [^{18}F]AMBF$_3$Los uptake by MDA-MB-231, SKOV3, and MKN45 cells compared to CHO-AT_1R cells could be due to a significantly lower AT_1R protein expression. Levels of mRNA are not always positively correlated with protein expression. In fact, several reports have shown that mRNA expression is useful, however certainly far from perfect in predicting the protein levels of certain proteins (Guo *et al.*, 2008; Maier *et al.*, 2009). Moreover, cancer cells probably have a lower AT_1R concentration which may have been saturated with the cold mass of the tracer formulation. In general, receptors have relatively low concentration (10 pmol/mg tissue) and therefore, molar activities must be as high as possible to avoid receptor saturation, and to ensure maximal ligand-receptor binding (Elsinga, 2002). Although these assays were performed with low molar activity, the increased uptake at the CHO-AT_1R cells indicated the concentration of the receptor is another important parameter to ensure and visualize the ligand-receptor binding. In addition, it is well known that tumor cells display aberrant glycosylation (Munkley and Elliott, 2016) and that AT_1R glycosylation enhances receptor stability and cell surface receptor expression (Jayadev *et al.*, 1999). Further studies will be needed to verify whether or not cell surface AT_1R expression levels in tumor cells are similar to non-tumoral cell lines such as CHO.

Kidneys are usually chosen as control organ for evaluating the AT_1R binding properties of new AT_1R radioligands due to the highly conserved AT_1R distribution in all adult mammals, including humans (Allen *et al.*, 2000). *In vivo* studies in healthy mice showed that both [^{18}F]FEtLos and [^{18}F]AMBF$_3$Los are specific for renal AT_1R binding with different profiles of kidney uptake. In particular, the higher activity concentration on kidney cortex instead of medulla, showed by [^{18}F]AMBF$_3$Los, was also visualized with other PET losartan derivatives evaluated in rats (Arksey *et al.*, 2014; Ismail *et al.*, 2015).

Rodents have two AT_1R isoforms: subtype A (AT_{1A}) and subtype B (AT_{1B}). In mouse kidney, $AT_{1A}R$ is the predominant form of AT_1R (Gonzalez-Villalobos *et al.*, 2010). According to literature, $AT_{1A}R$ expression was clearly evident in kidney, adrenal gland, liver, brain, ovary, testes, adipose tissue, lung, and heart of adult mice; while $AT_{1B}R$ was absent from most of these tissues and detectable in brain, testes, and adrenal gland (Burson *et al.*, 1994). Reports of immunohistochemistry studies showed AT_1R expression extensively throughout the kidneys from C57BL/6J mice on glomeruli and proximal tubules cells, interstitial cells and, more strongly, on blood vessels, distal tubules, and collecting ducts (Gonzalez-Villalobos *et al.*, 2010). Other reports revealed that mRNA $AT_{1A}R$ abundance on kidney tissues from wild-type mice was similar between the renal cortex and the medulla (Herrera *et al.*, 2013). Therefore, both kidneys profiles of [^{18}F]FEtLos and [^{18}F]AMBF$_3$Los may be acceptable since the mice models were not exactly the same.

In spite of the specific *in vivo* [^{18}F]AMBF$_3$Los tumor binding, evaluated 60 minutes after intratumoral injection, no tumor uptake was visualized at this time point when tracer injection was performed intravenously. Furthermore, [^{18}F]AMBF$_3$Los displayed a very quickly blood clearance with less than one minute half-life. Therefore, the very short time of [^{18}F]AMBF$_3$Los in the bloodstream may also account for the non-tumor uptake seen after i.v. injection. On the other hand, [^{18}F]FEtLos exhibited non-specific tumor AT_1R binding, possibly due to the lower AT_1R expression on tumors compared with kidneys, and the low AT_1R binding affinity; consequently, no further studies were performed with this derivative.

AT_1R blockers like losartan, valsartan and telmisartan have high protein binding (98.7, 95 and >99 %, respectively), and longer half-lives such as 2, 9 and 24 hours, respectively (Burnier e Brunner, 2000). Hence, the short blood circulation time of [^{18}F]AMBF$_3$Los may be due to poor plasma protein binding or water solubility. A ligand with high plasma protein may have longer circulation time and higher probability to reach the tumor tissue leading to the ligand - receptor binding if the free fraction is responsible for that. Moreover, poor water solubility may lead to drug elimination from the bloodstream before reaching the tumor tissue, because the reticulo-endothelial system recognizes hydrophobic materials as foreign (Tran *et al.*, 2017). Indeed, the negative log $D_{7.4}$ of [^{18}F]AMBF$_3$Los (-0.4) indicates it is hydrophilic, which would favor the circulation time and tumor uptake.

[^{18}F]AMBF$_3$-tracers targeting carbonic anhydrase IX, a transmembrane enzyme, displayed good tumor uptake at 1 h after tracer injection and a log $D_{7.4}$ varying from -1.9 to -2.5 (Lau *et al.*, 2015), which indicate that these tracers are more hydrophilic than [^{18}F]AMBF$_3$Los. Therefore, new analogs of AT_1R blockers should be designed to be more hydrophilic than [^{18}F]AMBF$_3$Los and then evaluated as tumor imaging PET tracers.

Despite the increasing *in vitro* and *in vivo* evidence exhibiting AT_1R as a promising cancer target, a recent analysis highlighted the opposite. These authors argued that (1) subpopulation overexpressing AT_1R represents a low incidence (<20% in breast cancer); (2) AT_1R activation follows a complex signaling and certainly possible not all of the actions of ANG II acting via AT_1R in tumors are harmful; (3) very high doses are used for the AT_1R blockade in tumor-bearing mice compared with the normal doses for adult patients (Vinson, 2017). Nonetheless, other authors reported that the positive expression rate of AT_1R in human breast cancer tissue was 48% (49/102), and was correlated with axillary lymph node metastasis (Chen *et al.*, 2013). Besides, immunohistochemical AT_1R expression in human ovarian tumor tissues showed that AT_1R was expressed in 85% (57/67) of invasive adenocarcinomas, and 55% of them were strongly positive (Suganuma *et al.*, 2005). In human samples from 152 surgically resected esophageal squamous cell carcinoma (ESCC) patients, AT_1R overexpression was univariately associated with inferior overall survival compared to disease-free survival; besides that, AT_1R has been considered an independent prognosticator in ESCC (Li *et al.*, 2016). Although these results are quite promising, several gaps between preclinical and clinical data need to be addressed such as: 1) No one knows for sure if enough levels of ARBs reach to the tumor microenvironment and exerts a direct anti-tumor effect; 2) Although the half-lives of ARBs vary from 2 (losartan) to 24 (telmisartan) hours, the great majority of the antitumoral preclinical data was obtained using losartan, whereas clinical studies do not provide specific information regarding which ARBs is being taken by the patients enrolled in the studies and; 3) The doses of losartan used in preclinical cancer models are 100-fold higher than the regular doses used for the treatment of hypertension in adult patients.

Since losartan has the shortest half-life among the ARBs (Abraham *et al.*, 2015), our apparent negative result led us to hypothesize that higher doses of losartan needed in preclinical cancer models in order to exert its antitumoral

effects are necessary due to its pharmacokinetic profile. As an example, the usual daily doses of losartan to control the blood pressure range from 20-100 mg per day/adult patient. Assuming that the average weight of a mouse is 25 grams, the usual doses of losartan used in preclinical cancer models range from 2000-2800 mg of losartan per day/mouse (Coulson *et al.*, 2017; Zhao *et al.*, 2019). In addition, and considering that ARBs have different half-lives, our data point out the importance of comparing the same ARBs used in *in vitro* and *in vivo* studies. It is quite common to associate the preclinical benefits of high doses of losartan with extended overall cancer survival in patients under treatment with ARBs, without specifying which ARBs they have been treated with (Zhao *et al.*, 2019). Nonetheless our results demonstrate that ^{18}F-ARBs derivatives could be suitable tracers to cancer imaging AT_1R-expressing tumor microenvironment, however, radiolabeled ARBs that possess better pharmacokinetics profile may be required.

7 CONCLUSIONS

1 The cold compounds FEtLos and $AMBF_3$Los were successfully synthesized and characterized by MS and NMR experiments confirming their chemical structures.

2 The manual radiosynthesis of [^{18}F]FEtOTs was optimized from a radiation safety point of view; then, [^{18}F]FEtLos was synthetized by the [^{18}F]fluoroethylation of two losartan precursors with low molar activity and high radiochemical purity. [^{18}F]FEtLos was found to be less lipophilic than parental losartan, stable in saline, and exhibited low AT_1R binding affinity.

3 [^{18}F]$AMBF_3$Los was synthetized by ^{18}F-^{19}F isotopic exchange reaction with high radiochemical purity, and molar activities ranging from 2 to 139 GBq/μmol. [^{18}F]$AMBF_3$Los was slightly hydrophilic, stable in mouse plasma and saline, and showed high AT_1R binding affinity.

4 The radioligand [^{18}F]$AMBF_3$Los bound specifically to AT_1R-expressing cells *in vitro* and displayed a high tissue uptake in the kidney cortex of mice.

5 When injected intratumorally, [^{18}F]$AMBF_3$Los was found to bind specifically to tumor xenograft and was competitively inhibited by cold losartan, while [^{18}F]FEtLos showed non-specific AT_1R binding. However, [^{18}F]$AMBF_3$Los was not able to reach the tumor site once injected intravenously probably because of its rapid metabolism and very fast clearance. Both radioligands were excreted by renal and hepatobiliary pathways.

6 ^{18}F-Angiotensin II receptor blockers derivatives could be suitable tracers to cancer imaging AT_1R-expressing tumor microenvironment, however, radiolabeled ARBs that possess better pharmacokinetics profile may be required.

8 BIBLIOGRAPHIC REFERENCES

ABRAHAM, H. M. A.; WHITE, C. M.; WHITE, W. B. The comparative efficacy and safety of the angiotensin receptor blockers in the management of hypertension and other cardiovascular diseases. ***Drug safety***, v. 38, n. 1, p. 33-54, 2015. Available in: <www.periodicos.capes.gov.br>. Accessed on Mai. 8, 2019.

AGER, E. I.; NEO, J.; CHRISTOPHI, C. The renin-angiotensin system and malignancy. ***Carcinogenesis*****,** v. 29, n. 9, p. 1675-84, 2008. Available in: <www.periodicos.capes.gov.br>. Accessed on Nov. 15, 2017.

ALLEN, A. M.; ZHUO, J.; MENDELSOHN, F. A. Localization and function of angiotensin AT1 receptors. ***American Journal of Hypertension***, v. 13, n. 1 Pt 2, p. 31S-38S, 2000. Available in: <www.periodicos.capes.gov.br>. Accessed on Dec. 8, 2018.

ANANDANADESAN, R.; GONG, Q.; CHIPITSYNA, G.; WITKIEWICZ, A.; YEO, C.J.; ARAFAT, H.A. Angiotensin II induces vascular endothelial growth factor in pancreatic cancer cells through an angiotensin II type 1 receptor and ERK1/2 signaling. ***Journal of Gastrointestinal Surgery*****,** v. 12, n. 1, p. 57-66, 2008. Available in: <www.periodicos.capes.gov.br>. Accessed on Nov. 2, 2018.

ARAFAT, H. A.; GONG, Q.; CHIPITSYNA, G.; RIZVI, A.; SAA, C.T.; YEO, C.J. Antihypertensives as novel antineoplastics: angiotensin-I-converting enzyme inhibitors and angiotensin II type 1 receptor blockers in pancreatic ductal adenocarcinoma. ***Journal of the American College of Surgeons*****,** v. 204, n. 5, p. 996-1005, 2007. Available in: <www.periodicos.capes.gov.br>. Accessed on Aug. 5, 2017.

ARKSEY, N.; HADIZAD, T.; ISMAIL, B.; HACHEM, M.; VALDIVIA, A.C.; BEANLANDS, R.S.; DE KEMP, R.A.; DA SILVA, J.N. Synthesis and evaluation of the novel 2-[^{18}F]fluoro-3-propoxy-triazole-pyridine-substituted losartan for imaging AT_1 receptors. ***Bioorganic & Medicinal Chemistry*****,** v. 22, n. 15, p. 3931-7, 2014. Available in: <www.periodicos.capes.gov.br>. Accessed on June 13, 2018.

ARRIETA, O.; GUEVARA, P.; ESCOBAR, E.; GARCÍA-NAVARRETE, R.; PINEDA, B.; SOTELO, J. Blockage of angiotensin II type I receptor decreases the synthesis of growth factors and induces apoptosis in C6 cultured cells and C6 rat glioma. ***British Journal of Cancer*****,** v. 92, n. 7, p. 1247-52, 2005. Available in: <www.periodicos.capes.gov.br>. Accessed on Nov. 2, 2018.

BERNARD-GAUTHIER, V.; ALIAGA, A.; ALIAGA, A.; BOUDJEMELINE, M.; HOPEWELL, R.; KOSTIKOV, A.; ROSA-NETO, P.; THIEL, A.; SCHIRRMACHER, R. Syntheses and evaluation of carbon-11- and fluorine-18-radiolabeled pan-tropomyosin receptor kinase (Trk) inhibitors: exploration of the 4-aza-2-oxindole scaffold as Trk PET imaging agents. ***ACS Chemical Neuroscience**,* v. 6, p. 260-276, 2015.

BLOCK, D.; COENEN, H. H.; STÖCKLIN, G. The NCA nucleophilic 18F-fluorination of 1, N-disubstituted alkanes as fluoroalkylation agents. ***Journal of Labelled Compounds and Radiopharmaceuticals***, v. 24, n. 9, p. 1029-1042, 1987.

BOSE, S. K.; GIBSON, W.; GIRI, S.; NATH, N.; DONALD, C.D. Angiotensin II up-regulates PAX2 oncogene expression and activity in prostate cancer via the angiotensin II type I receptor. ***Prostate*****,** v. 69, n. 12, p. 1334-42, 2009. Available in: <www.periodicos.capes.gov.br>. Accessed on Aug. 5, 2017.

BRESCHI, M. C. CALDERONE, V.; DIGIACOMO, M.; MARTELLI, A.; MARTINOTTI, E.; MINUTOLO, F.; RAPPOSELLI, S.; BALSAMO, A. NO-sartans: a new class of pharmacodynamic hybrids as cardiovascular drugs. ***Journal of Medicinal Chemistry*****,** v. 47, n. 23, p. 5597-600, 2004. Available in: <www.periodicos.capes.gov.br>. Accessed on March 31, 2019.

BURNIER, M.; BRUNNER, H. R. Angiotensin II receptor antagonists. ***Lancet***, v. 355, n. 9204, p. 637-45, 2000. Available in: <www.periodicos.capes.gov.br>. Accessed on Feb. 9, 2019.

BURSON, J. M.; AGUILERA, G.; GROSS, K. W.; SIGMUND, C. D. Differential expression of angiotensin receptor 1A and 1B in mouse. ***American Journal of Physiology***, v. 267, n. 2 Pt 1, p. E260-7,1994. Available in: <www.periodicos.capes.gov.br>. Accessed on Dec. 8, 2018.

CAI, L.; LU, S.; PIKE, V. W. Chemistry with [18F] fluoride ion. ***European Journal of Organic Chemistry*****,** v. 2008, n. 17, p. 2853-2873, 2008. Available in: <www.periodicos.capes.gov.br>. Accessed on Nov. 3, 2018.

CARINI, D. J.; DUNCIA, J.J.V.; ALDRICH, P.E.; CHIU, A.T.; JOHNSON, A.L.; PIERCE, M.E.; PRICE, W.A.; SANTELLA, J.B.; WELLS, G.J.; WEXLER, R.R.; WONG, P.C.; YOO, S-E.; TIMMERMANS, P.B.M.W.M. Nonpeptide angiotensin II receptor antagonists: the discovery of a series of N-(biphenylylmethyl) imidazoles as potent, orally active antihypertensives. ***Journal of medicinal chemistry*****,** v. 34, n. 8, p. 2525-2547,1991.

CARL-MCGRATH, S.; EBERT, M.P.; LENDECKEL, U.; RÖCKEN, C. Expression of the local angiotensin II system in gastric cancer may facilitate lymphatic invasion and nodal spread. ***Cancer Biology & Therapy*****,** v. 6, n. 8, p. 1218-26, 2007. Available in: <www.periodicos.capes.gov.br>. Accessed on Aug. 6, 2017.

CHATZIIOANNOU, A. F. Instrumentation for molecular imaging in preclinical research: Micro-PET and Micro-SPECT. ***Proceedings of the American Thoracic Society*****,** v. 2, n. 6, p. 533-6, 510-11, 2005. Available in: <www.periodicos.capes.gov.br>. Accessed on Jun. 13, 2018.

CHAUHAN, V. P.; MARTIN, J. D.; LIU, H.; LACORRE, D. A.; JAIN, S. R.; KOZIN, S. V.; STYLIANOPOULOS, T.; MOUSA, A. S.; HAN, X.; ADSTAMONGKONKUL, P.; POPOVIĆ, Z.; HUANG, P.; BAWENDI, M. G.; BOUCHER, Y.; JAIN, R. K. Angiotensin inhibition enhances drug delivery and potentiates chemotherapy by decompressing tumour blood vessels. ***Nature Communications*****,** v. 4, p. 2516, 2013. Available in: <www.periodicos.capes.gov.br>. Accessed on Nov. 2, 2018.

CHEN, C.-H. Angiotensin II type I receptor drives cancer progression through the FLJ10540/S100A9 pathway in oral cancer. ***Proceedings of the 107th Annual Meeting of the American Association for Cancer Research***, 2016, New Orleans, LA. Philadelphia (PA). Cancer research, 76(14 Supplement):5148-5148 [abstract].

CHEN, X.; HIRANO, M.; WERNER, R.A.; DECKER, M.; HIGUCHI, T. Novel 18F-labeled PET imaging agent FV45 targeting the renin - angiotensin system. ***ACS Omega*****,** v. 3, n. 9, p. 10460-10470, 2018. Available in: <www.periodicos.capes.gov.br>. Accessed on Nov. 2, 2018.

CHEN, X.; MENG, Q.; ZHAO, Y.; LIU, M.; LI, D.; YANG, Y.; SUN, L.; SUI, G.; CAI, L.; DONG, X. Angiotensin II type 1 receptor antagonists inhibit cell proliferation and angiogenesis in breast cancer. ***Cancer Letters*****,** v. 328, n. 2, p. 318-24, 2013. Available in: <www.periodicos.capes.gov.br>. Accessed on Aug. 5, 2017.

CLAYDEN, J.; GREEVES, N.; WARREN, S. ***Organic Chemistry***. United States: Oxford University Press Inc., New York, 2012a. Chapter. 17, elimination reactions. p.382-406.

CLAYDEN, J.; GREEVES, N.; WARREN, S. ***Organic Chemistry***. United States: Oxford University Press Inc., New York, 2012b. Chapter. 15, nucleophilic substitution at saturated carbon. p.328-359.

COENEN, H. H. ***PET Chemistry. The Driving Force in Molecular Imaging*****.** Ernst Schering Research Foundation Workshop 62. New York: Springer Berlin Heidelberg, 2007. Cap. 2, fluorine-18 labeling methods: features and possibilities of basic reactions. p.15-50.

COLE, E. L.; STEWART, M. N.; LITTICH, R.; HOAREAU, R.; SCOTT, P. J. Radiosyntheses using fluorine-18: the art and science of late stage fluorination. ***Current Topics in Medicinal Chemistry*****,** v. 14, n. 7, p. 875-900, 2014. Available in: <www.periodicos.capes.gov.br>. Accessed on Nov. 2, 2018.

CONTI, M.; ERIKSSON, L. Physics of pure and non-pure positron emitters for PET: a review and a discussion. ***EJNMMI Physics*****,** v. 3, n. 1, p. 8, 2016. Available in: <www.periodicos.capes.gov.br>. Accessed on Nov. 2, 2018.

COULSON, R.; LIEW, S. H.; CONNELLY, A. A.; YEE, N. S.; DEB, S.; KUMAR, B.; VARGAS, A. C.; O'TOOLE, S. A.; PARSLOW, A. C.; POH, A.; PUTOCZKI, T.; MORROW, R. J.; ALORRO, M.; LAZARUS, K. A.; YEAP, E. F. W.; WALTON, K. L.; HARRISON, C. A.; HANNAN, N. J.; GEORGE, A. J.; CLYNE, C. D.; ERNST, M.; ALLEN, A. M.; CHAND, A. L. The angiotensin receptor blocker, Losartan, inhibits mammary tumor development and progression to invasive carcinoma. ***Oncotarget***, v. 8, n. 12, p. 18640-18656, 2017. Avaliable in: <www.periodicos.capes.gov.br>. Accessed on Dec. 8, 2018.

CROWLEY, S. D.; COFFMAN, T. M. Recent advances involving the renin-angiotensin system. ***Experimental Cell Research*****,** v. 318, n. 9, p. 1049-56, 2012. Avaliable in: <www.periodicos.capes.gov.br>. Accessed on Nov.15, 2017.

DASGUPTA, C.; ZHANG, L. Angiotensin II receptors and drug discovery in cardiovascular disease. ***Drug Discovery Today*****,** v. 16, n. 1-2, p. 22-34, 2011. Available in: <www.periodicos.capes.gov.br>. Accessed on Nov. 15, 2017.

DE VRIES, E. F.; VROEGH, J.; ELSINGA, P. H.; VAALBURG, W. Evaluation of fluorine-18-labeled alkylating agents as potential synthons for the labeling of oligonucleotides. ***Applied Radiation and Isotopes***, v. 58, n. 4, p. 469-76, 2003. Available in: <www.periodicos.capes.gov.br>. Accessed on Aug. 6, 2017.

DIAS-PEIXOTO, M. F.; FERREIRA, A. J.; ALMEIDA, P. W.; BRAGA, V. B.; COUTINHO, D. C.; MELO, D. S.; GOMES FILHO, A.; MELO, M. B.; GRECO, L.; CAMPAGNOLE-SANTOS, M. J.; LIMA, R. F.; SANTOS, R. A.; GUATIMOSIM, S. The cardiac expression of Mas receptor is responsive to different physiological and pathological stimuli. ***Peptides***, v. 35, n. 2, p. 196-201, 2012. Available in: <www.periodicos.capes.gov.br>. Accessed on Feb. 8, 2019.

DOLLEY-HITZE, T.; JOUAN, F.; MARTIN, B.; MOTTIER, S.; EDELINE, J.; MORANNE, O.; LE POGAMP, P.; BELAUD-ROTUREAU, M. A.; PATARD, J. J.; RIOUX-LECLERCQ, N.;VIGNEAU, C. Angiotensin-2 receptors (AT1-R and AT2-R), new prognostic factors for renal clear-cell carcinoma?. ***British Journal of Cancer*****,** v. 103, n. 11, p. 1698-705, 2010. Available in: <www.periodicos.capes.gov.br>. Accessed on Aug. 6, 2017.

DOLLÉ, F. ***PET Chemistry. The Driving Force in Molecular Imaging*****.** Ernst Schering Research Foundation Workshop 62. New York: Springer Berlin Heidelberg, 2007. Cap. 5, [18F]Fluoropyridines: from conventional radiotracers to the labeling of macromolecules such as proteins and oligonucleotides. p.113-157.

DOMÍNGUEZ CATASÚS, J.; ORTEGA PIJEIRA, M.S.; MARTÍNEZ BÁEZ, E.; BORROTO PORTELA, J. I. Extracción del 99mTcO4-eluido del generador de 99Mo/99mTc empleando diferentes formulaciones de la mezcla TBF-TOA/ciclohexano como solvente. ***Nucleus***, n. 55, p. 01-06, 2014.

DU, N.; FENG, J.; HU, L. J.; SUN, X.; SUN, H. B.; ZHAO, Y.; YANG, Y. P.; REN, H. Angiotensin II receptor type 1 blockers suppress the cell proliferation effects of angiotensin II in breast cancer cells by inhibiting AT1R signaling. ***Oncology Reports*****,** v. 27, n. 6, p. 1893-903, 2012.

ELSINGA, P. H. Radiopharmaceutical chemistry for positron emission tomography. ***Methods*****,** v. 27, n. 3, p. 208-17, 2002. Available in: <www.periodicos.capes.gov.br>. Accessed on Jun. 16, 2018.

FAN, L.; FENG, Y.; WAN, H. Y.; NI, L.; QIAN, Y. R.; GUO, Y.; XIANG, Y.; LI, Q. Y. Hypoxia induces dysregulation of local renin-angiotensin system in mouse Lewis lung carcinoma cells. ***Genetics and Molecular Research***, v. 13, n. 4, p. 10562-73, 2014. Available in: <www.periodicos.capes.gov.br>. Accessed on Jun. 16, 2018.

FENG, Y. H.; NODA, K.; SAAD, Y.; LIU, X. P.; HUSAIN, A.; KARNIK, S. S. The docking of Arg2 of angiotensin II with Asp281 of AT1 receptor is essential for full agonism. ***Journal of Biological Chemistry*****,** v. 270, n. 21, p. 12846-50, 1995. Available in: <www.periodicos.capes.gov.br>. Accessed on Nov. 15, 2017.

FUKUDA, H.; KUBOTA, K.; MATSUZAWA, T. Pioneering and fundamental achievements on the development of positron emission tomography (PET) in oncology. ***The Tohoku journal of experimental medicine*****,** v. 230, n. 3, p. 155-169, 2013. Available in: <www.periodicos.capes.gov.br>. Accessed on Nov. 2, 2018.

FUKUSHIMA, K.; BRAVO, P. E.; HIGUCHI, T.; SCHULERI, K. H.; LIN, X.; ABRAHAM, M. R.; XIA, J.; MATHEWS, W. B.; DANNALS, R. F.; LARDO, A. C.; SZABO, Z.; BENGEL, F. M. Molecular hybrid positron emission tomography/computed tomography imaging of cardiac angiotensin II type 1 receptors. ***Journal of the American College of Cardiology*****,** v. 60, n. 24, p. 2527-34, 2012. Available in: <www.periodicos.capes.gov.br>. Accessed on Nov. 2, 2018.

GEORGE, A. J.; THOMAS, W. G.; HANNAN, R. D. The renin-angiotensin system and cancer: old dog, new tricks. ***Nature Reviews Cancer*****,** v. 10, n. 11, p. 745-59, 2010. Available in: <www.periodicos.capes.gov.br>. Accessed on Nov. 15, 2017.

GIESE, M. J.; SPETH, R. C. The ocular renin-angiotensin system: a therapeutic target for the treatment of ocular disease. ***Pharmacology & Therapeutics***, v. 142, n. 1, p. 11-32, 2014. Available in: <www.periodicos.capes.gov.br>. Accessed on Feb. 9, 2019.

GILLIS, E. P.; EASTMAN, K. J.; HILL, M. D.; DONNELLY, D. J.; MEANWELL, N. A. Applications of fluorine in medicinal chemistry. ***Journal of Medicinal Chemistry*****,** v. 58, n. 21, p. 8315-59, 2015. Available in: <www.periodicos.capes.gov.br>. Accessed on Nov. 3, 2018.

GLASER, M.; ROBINS, E. G. “Click labeling” in PET radiochemistry. ***Journal of Labelled Compounds and Radiopharmaceuticals*****,** v. 52, p. 407-414, 2009.

GONG, Q.; DAVIS, M.; CHIPITSYNA, G.; YEO, C. J.; ARAFAT, H. A. Blocking angiotensin II Type 1 receptor triggers apoptotic cell death in human pancreatic cancer cells. ***Pancreas*****,** v. 39, n. 5, p. 581-94, 2010. Available in: <www.periodicos.capes.gov.br>. Accessed on Nov. 5, 2017.

GONZALEZ-VILLALOBOS, R. A.; SATOU, R.; OHASHI, N.; SEMPRUN-PRIETO, L. C.; KATSURADA, A.; KIM, C.; UPCHURCH, G. M.; PRIETO, M. C.; KOBORI, H.; NAVAR, L. G. Intrarenal mouse renin-angiotensin system during ANG II-induced hypertension and ACE inhibition. ***American Journal of Physiology-Renal Physiology***, v. 298, n. 1, p. F150-7, 2010. Available in: <www.periodicos.capes.gov.br>. Accessed on Dec. 8, 2018.

GONÇALVES NUNES, P. S.; ZHANG, Z.; KUO, H.T.; ZHANG, C.; ROUSSEAU, J.; ROUSSEAU, E.; LAU, J.; KWON, D.; CARVALHO, I.; BÉNARD, F.; LIN, K. S. Synthesis and evaluation of an 18F-labeled trifluoroborate derivative of 2-nitroimidazole for imaging tumor hypoxia with positron emission tomography. ***Journal of Labelled Compounds and Radiopharmaceuticals***, v. 61, n. 4, p. 370-379, 2018. Available in: <www.periodicos.capes.gov.br>. Accessed on Jan. 11, 2019.

GUIMOND, M. O.; BATTISTA, M. C.; NIKJOUITAVABI, F.; CARMEL, M.; BARRES, V.; DOUEIK, A. A.; FAZLI, L.; GLEAVE, M.; SABBAGH, R.; GALLO-PAYET, N. Expression and role of the angiotensin II AT2 receptor in human prostate tissue: in search of a new therapeutic option for prostate cancer. ***Prostate*****,** v. 73, n. 10, p. 1057-68, 2013. Available in: <www.periodicos.capes.gov.br>. Accessed on Aug. 6, 2017.

GULALDI, N. C.; XIA, J.; FENG, T.; HONG, K.; MATHEWS, W. B.; RUBEN, D.; KAMEL, I. R.; TSUI, B. M.; SZABO, Z. Modeling of the renal kinetics of the AT1 receptor specific PET radioligand [11C]KR31173. ***BioMed Research International*****,** v. 2013, p. 835859, 2013. Available in: <www.periodicos.capes.gov.br>. Accessed on Nov. 2, 2018.

GUO, Y.; XIAO, P.; LEI, S.; DENG, F.; XIAO, G. G.; LIU, Y.; CHEN, X.; LI, L.; WU, S.; CHEN, Y.; JIANG, H.; TAN, L.; XIE, J.; ZHU, X.; LIANG, S.; DENG, H. How is mRNA expression predictive for protein expression? A correlation study on human circulating monocytes. ***Acta Biochimica et Biophysica Sinica (Shanghai)***, v. 40, n. 5, p. 426-36, 2008. Available in: <www.periodicos.capes.gov.br>. Accessed on Feb. 9, 2019.

HACHEM, M.; TIBERI, M.; ISMAIL, B.; HUNTER, C. R.; ARKSEY, N.; HADIZAD, T.; BEANLANDS, R. S.; DE KEMP, R. A.; DA SILVA, J. N.et al. Characterization of 18F-FPyKYNE-losartan for imaging AT1 Receptors. ***Journal of Nuclear Medicine*****,** v. 57, n. 10, p. 1612-1617, 2016.

HADIZAD, T.; COLLINS, J.; ANTOUN, R. E.; BEANLANDS, R. S; DA SILVA, J.N. [11C] Methyl-losartan as a potential ligand for PET imaging angiotensin II AT1 receptors. ***Journal of Labelled Compounds and Radiopharmaceuticals*****,** v. 54, n. 12, p. 754-757, 2011. Available in: <www.periodicos.capes.gov.br>. Accessed on Aug. 6, 2017.

HADIZAD, T.; KIRKPATRICK, S. A.; MASON, S.; BURNS, K.; BEANLANDS, R. S.; DASILVA, J. N. Novel O-[11C]methylated derivatives of candesartan as angiotensin II AT1 receptor imaging ligands: Radiosynthesis and ex vivo evaluation in rats. ***Bioorganic & medicinal chemistry*****,** v. 17, n. 23, p. 7971-7977, 2009. Available in: <www.periodicos.capes.gov.br>. Accessed on Nov. 2, 2018.

HAMILL, T. G.; BURNS, H. D.; DANNALS, R. F.; MATHEWS, W. B.; MUSACHIO, J. L.; RAVERT, H. T.; NAYLOR, E. M. Development of [11C] L-159,884: a radiolabelled, nonpeptide angiotensin II antagonist that is useful for angiotensin II, AT1 receptor imaging. ***Applied radiation and isotopes*****,** v. 47, n. 2, p. 211-218, 1996. Available in: <www.periodicos.capes.gov.br>. Accessed on Nov. 2, 2018.

HANAHAN, D.; WEINBERG, R. A. The Hallmarks of Cancer. ***Cell*****,** v. 100, n. 1, p. 57-70, 2000. Available in: <www.periodicos.capes.gov.br>. Accessed on Nov. 2, 2018.

HANAHAN, D.; WEINBERG, R. A. Hallmarks of cancer: the next generation. ***Cell*****,** v. 144, n. 5, p. 646-674, 2011. Available in: <www.periodicos.capes.gov.br>. Accessed on Nov. 2, 2018.

HERRERA, M.; SPARKS, M. A.; ALFONSO-PECCHIO, A. R.; HARRISON-BERNARD, L. M.; COFFMAN, T. M.. Lack of specificity of commercial antibodies leads to misidentification of angiotensin type 1 receptor protein. ***Hypertension***, v. 61, n. 1, p. 253-8, 2013. Available in: <www.periodicos.capes.gov.br>. Accessed on Dec. 8, 2018.

HOSHINO, K.; ISHIGURO, H.; TERANISHI, J.; YOSHIDA, S.; UMEMURA, S.; KUBOTA, Y.; UEMURA, H. Regulation of androgen receptor expression through angiotensin II type 1 receptor in prostate cancer cells. ***Prostate*****,** v. 71, n. 9, p. 964-75, 2011. Available in: <www.periodicos.capes.gov.br>. Accessed on Aug. 5, 2017.

HUANG, H.; LI, K.; LV, G.; LIU, G.; ZHAO, X.; LIU, Q.; WANG, S.; LI, X.; QIU, L.; LIN, J. One-Step 18F-Labeling of Estradiol Derivative for PET Imaging of Breast Cancer. ***Contrast Media & Molecular Imaging***, v. 2018, p. 5362329, 2018. Available in: <www.periodicos.capes.gov.br>. Accessed on Feb. 9, 2019.

HUANG, M. M.; GUO, A. B.; SUN, J. F.; CHEN, X. L.; YIN, Z. Y. Angiotensin II promotes the progression of human gastric cancer. ***Molecular Medicine Reports*****,** v. 9, n. 3, p. 1056-60, 2014. Available in: <www.periodicos.capes.gov.br>. Accessed on Aug. 6, 2017.

HUANG, W.; WU, Y-L.; ZHONG, J.; JIANG, F-X.; TIAN, X-I.; YU, L-F. Angiotensin II Type 1 Receptor Antagonist Suppress Angiogenesis and Growth of Gastric Cancer Xenografts. ***Digestive Diseases and Sciences*****,** v. 53, n. 5, p. 1206–1210, 2008. Available in: <www.periodicos.capes.gov.br>. Accessed on July 22, 2016.

IARC - INTERNATIONAL AGENCY FOR RESEARCH ON CANCER. **Global burden of cancer**. https://www.who.int/cancer/PRGlobocanFinal.pdf?ua=1. Accessed on March. 7, 2019.

IIMORI, H.; HASHIZUME, Y.; SASAKI, M.; KAJIWARA, Y.; SUGIMOTO, Y.; SUGIYAMA, Y.; WATANABE, Y.; SENDA, M. First automatic radiosynthesis of 11C labeled Telmisartan using a multipurpose synthesizer for clinical research use. ***Annals of Nuclear Medicine***, v. 25, n. 5, p. 333-7, 2011. Available in: <www.periodicos.capes.gov.br>. Accessed on Feb. 8, 2019.

INO, K.; SHIBATA, K.; YAMAMOTO, E.; KAJIYAMA, H.; NAWA, A.; MABUCHI, Y.; YAGI, S.; MINAMI, S. TANIZAKI, Y.; KOBAYASHI, A.; KIKKAWA, F. Role of the renin-angiotensin system in gynecologic cancers. ***Current Cancer Drug Targets*****,** v. 11, n. 4, p. 405-11, 2011. Available in: <www.periodicos.capes.gov.br>. Accessed on Nov. 15, 2017.

ISHIGURO, S.; YOSHIMURA, K.; TSUNEDOMI, R.; OKA, M.; TAKAO, S.; INUI, M.; KAWABATA, A.; WALL, T.; MAGAFA, V.; CORDOPATIS, P.; TZAKOS, A. G.; TAMURA, M. Involvement of angiotensin II type 2 receptor (AT2R) signaling in human pancreatic ductal adenocarcinoma (PDAC): a novel AT2R agonist effectively attenuates growth of PDAC grafts in mice. ***Cancer Biology & Therapy*****,** v. 16, n. 2, p. 307-16, 2015. Available in: <www.periodicos.capes.gov.br>. Accessed on Aug. 6, 2017.

ISMAIL, B.; HADIZAD, T.; ANTOUN, R.; LORTIE, M.; DEKEMP, R. A.; BEANLANDS, R. S.; DASILVA, J. N. Evaluation of [(11)C]methyl-losartan and [(11)C]methyl-EXP3174 for PET imaging of renal AT1receptor in rats. ***Nuclear Medicine and Biology*****,** v. 42, n. 11, p. 850-7, 2015. Available in: <www.periodicos.capes.gov.br>. Accessed on June 13, 2018.

JACOBSON, O.; KIESEWETTER, D. O.; CHEN, X. Fluorine-18 radiochemistry, labeling strategies and synthetic routes. ***Bioconjugate Chemistry*****,** v. 26, n. 1, p. 1-18, 2015. Available in: <www.periodicos.capes.gov.br>. Accessed on Aug. 6, 2017.

JAYADEV, S.; SMITH, R. D.; JAGADEESH, G.; BAUKAL, A. J.; HUNYADY, L.; CATT, K. J. N-linked glycosylation is required for optimal AT1a angiotensin receptor expression in COS-7 cells. ***Endocrinology***, v. 140, n. 5, p. 2010-2017, 1999. Available in: <www.periodicos.capes.gov.br>. Accessed on May 8, 2019.

JUILLERAT-JEANNERET, L.; CELERIER, J.; CHAPUIS BERNASCONI, C.; NGUYEN, G.; WOSTL, W.; MAERKI, H. P.; JANZER, R. C.; CORVOL, P.; GASC, J. M. Renin and angiotensinogen expression and functions in growth and apoptosis of human glioblastoma. ***British Journal of Cancer*****,** v. 90, n. 5, p. 1059-68, 2004. Available in: <www.periodicos.capes.gov.br>. Accessed on Aug. 6, 2017.

KALGUTKAR, A. S.; DANIELS, J. S. ***Metabolism, Pharmacokinetics and Toxicity of Functional Groups: Impact of Chemical Buildins Blocks on ADMET***. SMITH, D. A.: Royal Society of Chemistry, 2010. Chapter 3, carboxylic acids and their bioisosteres, p.99-167. Available in <https://books.google.com/?hl=es>. Accessed on Feb. 9, 2019.

KETTENBACH, K.; SCHIEFERSTEIN, H.; ROSS, T. L. 18F-labeling using click cycloadditions. ***BioMed Research International*****,** v. 2014, p. 361329, 2014. Available in: <www.periodicos.capes.gov.br>. Accessed on Nov. 3, 2018.

KHANAPUR, S.; PAUL, S.; SHAH, A.; VATAKUTI, S.; KOOLE, M.J.B.; ZIJLMA, R.; DIERCKX, R.A.J.O.; LUURTSEMA, G.; GARG, P.; WAARDE, A.V.; ELSINGA, P.H. Development of [18F]-labeled pyrazolo [4, 3-e]-1, 2, 4-triazolo [1, 5-c] pyrimidine (SCH442416) analogs for the imaging of cerebral adenosine A2A receptors with positron emission tomography. ***Journal of Medicinal Chemistry***, v. 57, n. 15, p. 6765-6780, 2014. Available in: <www.periodicos.capes.gov.br>. Accessed on Sep. 3, 2018.

KIM, S.; TOYOKAWA, H.; YAMAO, J.; SATOI, S.; YANAGIMOTO, H.; YAMAMOTO, T.; HIROOKA, S.; YAMAKI, S.; INOUE, K.; MATSUI, Y.; KWON, A. H. Antitumor effect of angiotensin II type 1 receptor blocker losartan for orthotopic rat pancreatic adenocarcinoma. ***Pancreas*****,** v. 43, n. 6, p. 886-90, 2014. Available in: <www.periodicos.capes.gov.br>. Accessed on Nov. 2, 2018.

KNIESS, T.; LAUBE, M.; BRUST, P.; STEINBACH, J. 2-[18 F] Fluoroethyl tosylate–a versatile tool for building 18 F-based radiotracers for positron emission tomography. ***MedChemComm*****,** v. 6, n. 10, p. 1714-1754, 2015. Available in: <www.periodicos.capes.gov.br>. Accessed on Aug. 6, 2017.

KOSAKA, T.; MIYAJIMA, A.; SHIROTAKE, S.; KIKUCHI, E.; HASEGAWA, M.; MIKAMI, S.; OYA, M. Ets-1 and hypoxia inducible factor-1alpha inhibition by angiotensin II type-1 receptor blockade in hormone-refractory prostate cancer. ***Prostate*****,** v. 70, n. 2, p. 162-9, 2010. Available in: <www.periodicos.capes.gov.br>. Accessed on Aug. 5, 2017.

KOSUGI, M.; MIYAJIMA, A.; KIKUCHI, E.; KOSAKA, T.; HORIGUCHI, Y.; MURAI, M. Effect of angiotensin II type 1 receptor antagonist on tumor growth and angiogenesis in a xenograft model of human bladder cancer. ***Human Cell*****,** v. 20, n. 1, p. 1-9, 2007. Available in: <www.periodicos.capes.gov.br>. Accessed on Aug. 6, 2017.

KROCK, B. L.; SKULI, N.; SIMON, M. C. Hypoxia-induced angiogenesis: good and evil. ***Genes Cancer***, v. 2, n. 12, p. 1117-33, 2011.

LASNE, M. C.; PERRIO, C.; ROUDEN, J.; BARRÉ, L.; ROEDA, D.; DOLLE, F.; CROUZEL, C. Chemistry of β^+-emitting compounds based on fluorine-18. ***Topics in Current Chemistry*****,** v. 222, p. 201-258, 2002.

LAU, J.; LIU, Z.; LIN, K. S.; PAN, J.; Zhang, Z.; VULLO, D.; SUPURAN, C. T.; PERRIN, D. M.; BÉNARD, F. Trimeric Radiofluorinated Sulfonamide Derivatives to Achieve In Vivo Selectivity for Carbonic Anhydrase IX-Targeted PET Imaging. ***Journal of Nuclear Medicine***, v. 56, n. 9, p. 1434-40, 2015. Available in: <www.periodicos.capes.gov.br>. Accessed on Jun. 13, 2018.

LAU, S. T.; LEUNG, P. S. Role of the RAS in pancreatic cancer. ***Current Cancer Drug Targets*****,** v. 11, n. 4, p. 412-20, 2011. Available in: <www.periodicos.capes.gov.br>. Accessed on Aug. 5, 2017.

LIESER, K. H. ***Nuclear and Radiochemistry: Fundamentals and Applications***. Second Edition. Federal Republic of Germany: WILEY-VCH Verlag GmbH, D-69469 Weinheim, 2001.

LI, S. H.; LU, H. I.; CHANG, A. Y.; HUANG, W. T.; LIN, W. C.; LEE, C. C.; TIEN, W. Y.; LAN, Y. C.; TSAI, H. T.; CHEN, C. H. Angiotensin II type I receptor (AT1R) is an independent prognosticator of esophageal squamous cell carcinoma and promotes cells proliferation via mTOR activation. ***Oncotarget***, v. 7, n. 41, p. 67150-67165, 2016. Available in: <www.periodicos.capes.gov.br>. Accessed on Feb. 9, 2019.

LIN, K.-S.; BENARD, F.; PERRIN, D. M. ***Fluorine in Life Sciences: Pharmaceuticals, Medicinal Diagnostics, and Agrochemicals***. In: INC., Elsevier.. (Ed.)., 2019. Chapter 14, organoboronates: captors of 18F-fluoride for one-step radiofluorination of biomolecules , p.519-549.

LIN, K. S.; PAN, J.; AMOUROUX, G.; TURASHVILI, G.; MESAK, F.; HUNDAL-JABAL, N.; POURGHIASIAN, M.; LAU, J.; JENNI, S.; APARICIO, S.; BÉNARD, F. In vivo radioimaging of bradykinin receptor b1, a widely overexpressed molecule in human cancer. ***Cancer Research***, v. 75, n. 2, p. 387-93, 2015. Available in: <www.periodicos.capes.gov.br>. Accessed on Feb. 13, 2018.

LIU, S. S.; WANG, H. Y.; TANG, J. M.; ZHOU, X. M. Hypoxia-induced collagen synthesis of human lung fibroblasts by activating the angiotensin system. ***International Journal of Molecular Sciences***, v. 14, n. 12, p. 24029-45, 2013. Available in: <www.periodicos.capes.gov.br>. Accessed on Feb. 9, 2019.

LIU, Z.; LIN, K. S.; BÉNARD, F.; POURGHIASIAN, M.; KIESEWETTER, D. O.; PERRIN, D. M.; CHEN, X. One-step (18)F labeling of biomolecules using organotrifluoroborates. ***Nature Protocols*****,** v. 10, n. 9, p. 1423-32, 2015. Available in: <www.periodicos.capes.gov.br>. Accessed on June 13, 2018.

LIU, Z.; POURGHIASIAN, M.; BÉNARD, F.; PAN, J.; LIN, K. S.; PERRIN, D.M. Preclinical evaluation of a high-affinity 18F-trifluoroborate octreotate derivative for somatostatin receptor imaging. ***Journal of Nuclear Medicine***, v. 55, n. 9, p. 1499-505, 2014. Available in: <www.periodicos.capes.gov.br>. Accessed on Feb. 9, 2019.

LIU, Z.; POURGHIASIAN, M.; RADTKE, M. A.; LAU, J.; PAN, J.; DIAS, G. M.; YAPP, D.; LIN, K. S.; BÉNARD, F.; PERRIN, D. M. An organotrifluoroborate for broadly applicable one-step 18F-labeling. ***Angewandte Chemie International Edition in English*****,** v. 53, n. 44, p. 11876-80, 2014. Available in: <www.periodicos.capes.gov.br>. Accessed on Nov. 3, 2018.

LIU, Z.; RADTKE, M. A.; WONG, M. Q.; LIN, K. S.; YAPP, D. T.; PERRIN, D. M. Dual mode fluorescent (18)F-PET tracers: efficient modular synthesis of rhodamine-[cRGD]2-[(18)F]-organotrifluoroborate, rapid, and high yielding one-step (18)F-labeling at high specific activity, and correlated in vivo PET imaging and ex vivo fluorescence. ***Bioconjugate Chemistry*****,** v. 25, n. 11, p. 1951-62, 2014. Available in: <www.periodicos.capes.gov.br>. Accessed on Nov. 3, 2018.

LORTIE, M.; DASILVA, J. N.; KIRKPATRICK, S. A.; HADIZAD, T.; ISMAIL, B. A.; BEANLANDS, R. S.; DEKEMP, R. A. Analysis of [11C]methyl-candesartan kinetics in the rat kidney for the assessment of angiotensin II type 1 receptor density in vivo with PET. ***Nuclear Medicine and Biology*****,** v. 40, n. 2, p. 252-61, 2013. Available in: <www.periodicos.capes.gov.br>. Accessed on Nov. 2, 2018.

MAIER, T.; GÜELL, M.; SERRANO, L. Correlation of mRNA and protein in complex biological samples. ***FEBS Letters***, v. 583, n. 24, p. 3966-73, 2009. Available in: <www.periodicos.capes.gov.br>. Accessed on Feb. 9, 2019.

MAJO, V. J.; MILAK, M. S.; PRABHAKARAN, J.; MALI, P.; SAVENKOVA, L.; SIMPSON, N. R.; MANN, J. J.; PARSEY, R. V.; KUMAR, J. S. Synthesis and in vivo evaluation of [(18)F]2-(4-(4-(2-(2-fluoroethoxy)phenyl)piperazin-1-yl)butyl)-4-methyl-1,2,4-triazine-3,5(2H,4H)-dione ([(18)F]FECUMI-101) as an imaging probe for 5-HT1A receptor agonist in nonhuman primates. ***Bioorganic & Medicinal Chemistry***, v. 21, n. 17, p. 5598-604, 2013. Available in: <www.periodicos.capes.gov.br>. Accessed on Sep. 3, 2018.

MATHEWS, W. B.; BURNS, H. D.; DANNALS, R. F.; RAVERT, H. T.; NAYLOR, E. M. Carbon-11 labeling of a potent, nonpeptide, AT1-selective angiotensin-II receptor antagonist: MK-996. ***Journal of Labelled Compounds and Radiopharmaceuticals*****,** v. 36, n. 8, p. 729-737, 1995.

MATHEWS, W. B.; SZABO, Z. Radioligands for the angiotensin II subtype 1 (AT1) receptor. ***Current Topics in Medicinal Chemistry*****,** v. 10, n. 16, p. 1585-99, 2010. Available in: <www.periodicos.capes.gov.br>. Accessed on Nov. 2, 2018.

MATHEWS, W. B.; YOO, S. E.; LEE, S. H.; SCHEFFEL, U.; RAUSEO, P. A.; ZOBER, T. G.; GOCCO, G.; SANDBERG, K.; RAVERT, H. T.; DANNALS, R. F.; SZABO, Z. A novel radioligand for imaging the AT1 angiotensin receptor with PET. ***Nuclear Medicine and Biology*****,** v. 31, n. 5, p. 571-4, 2004. Available in: <www.periodicos.capes.gov.br>. Accessed on Nov. 2, 2018.

MIURA, S.; KARNIK, S. S.; SAKU, K. Review: angiotensin II type 1 receptor blockers: class effects versus molecular effects. ***Journal of the Renin-Angiotensin-Aldosterone System*****,** v. 12, n. 1, p. 1-7, 2011. Available in: <www.periodicos.capes.gov.br>. Accessed on Nov. 15, 2017.

MUNKLEY, J. and ELLIOTT, D. Hallmarks of glycosylation in cancer. ***Oncotarget*****,** v. 7, n. 23, p. 35478-35489, 2016.

NODA, A.; FUSHIKI, H.; MURAKAMI, Y.; SASAKI, H.; MIYOSHI, S.; KAKUTA, H.; NISHIMURA, S. Brain penetration of telmisartan, a unique centrally acting angiotensin II type 1 receptor blocker, studied by PET in conscious rhesus macaques. ***Nuclear Medicine and Biology***, v. 39, n. 8, p. 1232-5, 2012. Available in: <www.periodicos.capes.gov.br>. Accessed on Feb. 8, 2019.

NODA, K.; SAAD, Y.; KARNIK, S. S. Interaction of Phe8 of angiotensin II with Lys199 and His256 of AT1 receptor in agonist activation. ***Journal of Biological Chemistry*****,** v. 270, n. 48, p. 28511-4, 1995. Available in: <www.periodicos.capes.gov.br>. Accessed on Nov. 15, 2017.

NODA, K.; SAAD, Y.; KINOSHITA, A.; BOYLE, T. P.; GRAHAM, R. M.; HUSAIN, A.; KARNIK, S. S. Tetrazole and carboxylate groups of angiotensin receptor antagonists bind to the same subsite by different mechanisms. ***Journal of Biological Chemistry*****,** v. 270, n. 5, p. 2284-9, 1995. Available in: <www.periodicos.capes.gov.br>. Accessed on Nov. 15, 2017.

OH, E.; KIM, J. Y.; CHO, Y.; AN, H.; LEE, N.; JO, H.; BAN, C.; SEO, J. H. Overexpression of angiotensin II type 1 receptor in breast cancer cells induces epithelial-mesenchymal transition and promotes tumor growth and angiogenesis. ***Biochimica et Biophysica Acta*****,** v. 1863, n. 6 Pt A, p. 1071-81, 2016. Available in: <www.periodicos.capes.gov.br>. Accessed on Nov. 2, 2018.

PAUL, M.; POYAN MEHR, A.; KREUTZ, R. Physiology of local renin-angiotensin systems. ***Physiological Reviews*****,** v. 86, n. 3, p. 747-803, 2006. Available in: <www.periodicos.capes.gov.br>. Accessed on Nov. 15, 2017.

PINHEIRO, S. V.; SIMÕES E SILVA, A. C. Angiotensin converting enzyme 2, Angiotensin-(1-7), and receptor MAS axis in the kidney. ***International Journal of Hypertension***, v. 2012, p. 414128, 2012. Available in: <www.periodicos.capes.gov.br>. Accessed on Feb. 8, 2019.

POURGHIASIAN, M.; LIU, Z.; PAN, J.; ZHANG, Z.; COLPO, N.; LIN, K. S.; PERRIN, D. M.; BÉNARD, F. (18)F-AmBF3-MJ9: a novel radiofluorinated bombesin derivative for prostate cancer imaging. ***Bioorganic & Medicinal Chemistry*****,** v. 23, n. 7, p. 1500-6, 2015. Available in: <www.periodicos.capes.gov.br>. Accessed on Jun. 13, 2018.

PRABHAKARAN, J.; ARANGO, V.; MAJO, V. J.; SIMPSON, N. R.; KASSIR, S. A.; UNDERWOOD, M. D.; POLAVARAPU, H.; BRUCE, J. N.; CANOLL, P.; MANN, J. J.; KUMAR, J. S. Synthesis and in vitro evaluation of [18F](R)-FEPAQ: a potential PET ligand for VEGFR2. ***Bioorganic & Medicinal Chemistry Letters***, v. 22, n. 15, p. 5104-7, 2012. Available in: <www.periodicos.capes.gov.br>. Accessed on Sep. 2, 2018.

PRETZE, M.; PIETZSCH, D.; MAMAT, C. Recent trends in bioorthogonal click-radiolabeling reactions using fluorine-18. ***Molecules*****,** v. 18, n. 7, p. 8618-65, 2013. Available in: <www.periodicos.capes.gov.br>. Accessed on Nov. 3, 2018.

RAHMIM, A.; ZAIDI, H. PET versus SPECT: strengths, limitations and challenges. ***Nuclear Medicine Communications*****,** v. 29, n. 3, p. 193-207, 2008.

RIVERA, E.; ARRIETA, O.; GUEVARA, P.; DUARTE-ROJO, A.; SOTELO, J. AT1 receptor is present in glioma cells; its blockage reduces the growth of rat glioma. ***British Journal of Cancer*****,** v. 85, n. 9, p. 1396-9, 2001. Available in: <www.periodicos.capes.gov.br>. Accessed on Nov. 2, 2018.

RODRIGUES-FERREIRA, S.; NAHMIAS, C. G-protein coupled receptors of the renin-angiotensin system: new targets against breast cancer?. ***Frontiers in Pharmacology*****,** v. 6, p. 24, 2015. Available in: <www.periodicos.capes.gov.br>. Accessed on Feb. 13, 2018.

ROSTOVTSEV, V. V.; GREEN, L. G.; FOKIN, V. V.; SHARPLESS, K. B. A stepwise huisgen cycloaddition process: copper (I)-catalyzed regioselective “ligation” of azides and terminal alkynes. ***Angewandte Chemie*****,** v. 114, n. 14, p. 2708-2711, 2002. Available in: <www.periodicos.capes.gov.br>. Accessed on Nov. 3, 2018.

RÖCKEN, C.; RÖHL, F. W.; DIEBLER, E.; LENDECKEL, U.; PROSS, M.; CARL-MCGRATH, S.; EBERT, M. P. The angiotensin II/angiotensin II receptor system correlates with nodal spread in intestinal type gastric cancer. ***Cancer Epidemiology, Biomarkers & Prevention*****,** v. 16, n. 6, p. 1206-12, 2007. Available in: <www.periodicos.capes.gov.br>. Accessed on Aug. 6, 2017.

SAITO, R. D. F.; LANA, M. V. G.; MEDRANO, R. F. V.; CHAMMAS, R. ***Fundamentos de Oncologia Molecular***. Brasil: Instituto do Cancer do Estado de São Paulo, Faculdade de Medicina da Universidade de São Paulo, 2015.

SCHIRRMACHER, R., WANGLER, C., & SCHIRRMACHER, E. Recent developments and trends in 18F-radiochemistry: syntheses and applications. ***Mini-Reviews in Organic Chemistry*****,** v. 4, n. 4, p. 317-329, 2007. Available in: <www.periodicos.capes.gov.br>. Accessed on Nov. 3, 2018.

SCHIRRMACHER, R.; WEBER, M.; SCHMITZ, A.; SHIUE, C.Y.; ALAVI, A.A.; FEILEN, P.; SCHNEIDER, S.; KANN, P.; RÖSCH, F. Radiosynthesis of 1-(4-(2-[18F]fluoroethoxy)benzenesulfonyl)-3-butyl urea: a potential β-cell imaging agent. ***Journal of Labelled Compounds and Radiopharmaceuticals***, v. 45, n. 9, p. 763-774, 2002. Available in: <www.periodicos.capes.gov.br>. Accessed on Sep. 2, 2018.

SCHOULTZ, B. W.; REED, B. J.; MARTON, J.; WILLOCH, F.; HENRIKSEN, G. A fully automated radiosynthesis of [18F]fluoroethyl-diprenorphine on a single module by use of SPE cartridges for preparation of high quality 2-[18F]fluoroethyl tosylate. ***Molecules*****,** v. 18, n. 6, p. 7271-8, 2013. Available in: <www.periodicos.capes.gov.br>. Accessed on Nov. 3, 2018.

SHAH, P.; WESTWELL, A. D. The role of fluorine in medicinal chemistry. ***Journal of Enzyme Inhibition and Medicinal Chemistry*****,** v. 22, n. 5, p. 527-40, 2007. Available in: <www.periodicos.capes.gov.br>. Accessed on Nov. 3, 2018.

SHIROTAKE, S.; MIYAJIMA, A.; KOSAKA, T.; TANAKA, N.; KIKUCHI, E.; MIKAMI, S.; OKADA, Y.; OYA, M. Regulation of monocyte chemoattractant protein-1 through angiotensin II type 1 receptor in prostate cancer. ***The American Journal of Pathology*****,** v. 180, n. 3, p. 1008-16, 2012. Available in: <www.periodicos.capes.gov.br>. Accessed on Nov. 2, 2018.

SUGANUMA, T.; INO, K.; SHIBATA, K.; KAJIYAMA, H.; NAGASAKA, T.; MIZUTANI, SH.; KIKKAWA, F. Functional expression of the angiotensin II type1 receptor in human ovarian carcinoma cells and its blockade therapy resulting in suppression of tumor invasion, angiogenesis, and peritoneal dissemination. ***Clinical Cancer Research*****,** v. 11, n. 7, p. 2686-2694, 2005. Available in: <www.periodicos.capes.gov.br>. Accessed on Aug. 6, 2017.

SUN, T.; TANG, G.; TIAN, H.; WANG, X.; CHEN, X.; CHEN, Z.; WANG, S. Radiosynthesis of 1-[18F]fluoroethyl-L-tryptophan as a novel potential amino acid PET tracer. ***Applied Radiation and Isotopes***, v. 70, n. 4, p. 676-80, 2012. Available in: <www.periodicos.capes.gov.br>. Accessed on Sep. 2, 2018.

SZABO, Z.; KAO, P. F.; BURNS, H. D.; GIBSON, R. E.; HAMILL, T. G.; RAVERT, H. T.; KIM, S. E.; MATHEWS, W. B.; MUSACHIO, J. L.; SCHEFFEL, U.; DANNALS , R. F. Investigation of angiotensin II/AT1 receptors with carbon-11-L-159,884: a selective AT1 antagonist. ***Journal of Nuclear Medicine*****,** v. 39, p. 1209-1213, 1998. Available in: <www.periodicos.capes.gov.br>. Accessed on Nov. 2, 2018.

SZABO, Z.; SPETH, R. C.; BROWN, P. R.; KERENYI, L.; KAO, P. F.; MATHEWS, W. B.; RAVERT, H. T.; HILTON, J.; RAUSEO, P.; DANNALS, R. F.; ZHENG, W.; LEE, S.; SANDBERG, K. Use of positron emission tomography to study AT1 receptor regulation in vivo. ***Journals of the American Society of Nephrology*****,** v. 12, n. 7, p. 1350-8, 2001. Available in: <www.periodicos.capes.gov.br>. Accessed on Nov. 2, 2018.

TAMURA, G.; SAKATA, K.; NISHIZUKA, S.; MAESAWA, C.; SUZUKI, Y.; IWAYA, T.; TERASHIMA, M.; SAITO, K.; SATODATE, R. Inactivation of the E-cadherin gene in primary gastric carcinomas and gastric carcinoma cell lines. ***Japanese journal of cancer research***, v. 87, n. 11, p. 1153-9, 1996. Available in: <www.periodicos.capes.gov.br>. Accessed on Feb. 9, 2019.

TANAKA, N.; MIYAJIMA, A.; KOSAKA, T.; MIYAZAQUI, Y.; SHIROTAKE, H.; KIKUCHI, E.; OYA, M. Acquired platinum resistance enhances tumour angiogenesis through angiotensin II type 1 receptor in bladder cancer. ***British Journal of Cancer*****,** v. 5, n. 9, p. 1331-1337, 2011. Available in: <www.periodicos.capes.gov.br>. Accessed on July 22, 2016.

TANAKA, N.; MIYAJIMA, A.; KOSAKA, T.; SHIROTAKE, S.; HASEGAWA, M.; KIKUCHI, E.; OYA, M. Cis-dichlorodiammineplatinum upregulates angiotensin II type 1 receptors through reactive oxygen species generation and enhances VEGF production in bladder cancer. ***Molecular Cancer Therapeutics*****,** v. 9, n. 11, p. 2982-92, 2010. Available in: <www.periodicos.capes.gov.br>. Accessed on Aug. 6, 2017.

THOMPSON, A. S.; GRABOWSKI, E., J. **Alcohol to azide SN2 conversion**. World Intellectual Property Organization and International Bureau, WO 95/01970, US, 1995.

THOMPSON, A. S.; HUMPHREY, G. R.; DEMARCO, A. M.; MATHRE, D. J.; GRABOWSKI, E. J. Direct Conversion of Activated Alcohols to Azides Using Diphenyl Phosphorazidate. A Practical Alternative to Mitsunobu Conditions. ***Journal of Organic Chemistry***, v. 58, p. 5886-5888, 1993.

TIETZE, R.; HOCKE, C.; LÖBER, S.; HÜBNER, H.; KUWERT, T.; GMEINER, P.; PRANTE, O. Syntheses and radiofluorination of two derivatives of 5-cyano-indole as selective ligands for the dopamine subtype-4 receptor. ***Journal of Labelled Compounds and Radiopharmaceuticals***, v. 49, n. 1, p. 55-70, 2006. Available in: <www.periodicos.capes.gov.br>. Accessed on Sep. 2, 2018.

TRAN, S.; DEGIOVANNI, P. J.; PIEL, B.; RAI, P. Cancer nanomedicine: a review of recent success in drug delivery. ***Clinical and Translational Medicine***, v. 6, n. 1, p. 44, 2017. Available in: <www.periodicos.capes.gov.br>. Accessed on Feb. 9, 2019.

TREGLIA, G.; SADEGHI, R.; DEL SOLE, A.; GIOVANELLA, L. Diagnostic performance of PET/CT with tracers other than F-18-FDG in oncology: an evidence-based review. ***Clinical and Translational Oncology*****,** v. 16, n. 9, p. 770-5, 2014. Available in: <www.periodicos.capes.gov.br>. Accessed on June 13, 2018.

UEHARA, Y.; MIURA, S.; YAHIRO, E.; SAKU, K. Non-ACE pathway-induced angiotensin II production. ***Current Pharmaceutical Design*****,** v. 19, n. 17, p. 3054-9, 2013. Available in: <www.periodicos.capes.gov.br>. Accessed on Nov. 15, 2017.

UEMURA, H.; HASUMI, H.; ISHIGURO, H.; TERANISHI, J.; MIYOSHI, Y.; KUBOTA, Y. Renin-angiotensin system is an important factor in hormone refractory prostate cancer. ***Prostate*****,** v. 66, n. 8, p. 822-30, 2006. Available in: <www.periodicos.capes.gov.br>. Accessed on Aug. 5, 2017.

UEMURA, H.; ISHIGURO, H.; NAKAIGAWA, N.; NAGASHIMA, Y.; MIYOSHI, Y.; FUJINAMI, K.; SAKAGUCHI, A.; KUBOTA, Y. Angiotensin II receptor blocker shows antiproliferative activity in prostate cancer cells: a possibility of tyrosine kinase inhibitor of growth factor. ***Molecular Cancer Therapeutics*****,** v. 2, n. 11, p. 1139-47, 2003. Available in: <www.periodicos.capes.gov.br>. Accessed on Aug. 5, 2017.

VAAJANEN, A.;KALESNYKAS, G.; VAPAATALO, H.; UUSITALO, H. The expression of Mas-receptor of the renin-angiotensin system in the human eye. ***Graefe's Archive for Clinical and Experimental Ophthalmology***, v. 253, n. 7, p. 1053-9, 2015. Available in: <www.periodicos.capes.gov.br>. Accessed on Feb. 8, 2019.

VAIDYANATHAN, S.; PATEL, C. N.; SCARSBROOK, A. F.; CHOWDHURY, F. U. FDG PET/CT in infection and inflammation--current and emerging clinical applications. ***Clinical Radiology***, v. 70, n. 7, p. 787-800, 2015. Available in: <www.periodicos.capes.gov.br>. Accessed on Nov. 19, 2018.

VALENTA, I.; SZABO, Z.; MATHEWS, W.; DANNALS, R.; POMPER, M.; ABRAHAM, T.; SCHINDLER, T. Abnormal regional increase of myocardial angiotensin II type 1 receptors in hypertrophic obstructive cardiomyopathy patients as determined with 11C-KR31173 and PET/CT. ***Journal of Nuclear Medicine***, v. 58, p. 439-439, 2017. Available in: <www.periodicos.capes.gov.br>. Accessed on Feb. 8, 2019.

VALLABHAJOSULA, S. 18F-Labeled Positron Emission Tomographic Radiopharmaceuticals in Oncology: An Overview of Radiochemistry and Mechanisms of Tumor Localization. ***Seminars in Nuclear Medicine,*** v. 37, n. 6, p. 400-419, 2007. Available in: <www.periodicos.capes.gov.br>. Accessed on Nov. 2, 2018.

VAUQUELIN, G.; FIERENS, F. L.; GÁBORIK, Z.; LE MINH, T.; DE BACKER, J. P.; HUNYADY, L. VANDERHEYDEN, P. M. Role of basic amino acids of the human angiotensin type 1 receptor in the binding of the non-peptide antagonist candesartan. ***Journal of Renin-Angiotensin-Aldosterone System***, v. 2, n. 1_suppl, p. S32-S36, 2001. Available in: <www.periodicos.capes.gov.br>. Accessed on Dec. 8, 2018.

VERJANS, J. W.; LOVHAUG, D.; NARULA, N.; PETROV, A. D.; INDREVOLL, B.; BJURGERT, E.; KRASIEVA, T. B.; PETERSEN, L. B.; KINDBERG, G. M.; SOLBAKKEN, M.; CUTHBERTSON, A.; VANNAN, M. A.; REUTELINGSPERGER, C. P.; TROMBERG, B. J.; HOFSTRA, L.; NARULA, J. Noninvasive imaging of angiotensin receptors after myocardial infarction. ***JACC: Cardiovascular Imaging*****,** v. 1, n. 3, p. 354-62, 2008. Available in: <www.periodicos.capes.gov.br>. Accessed on March 31, 2019.

VINSON, G. P. Why isn't the angiotensin type 1 receptor a target in cancer? ***Oncotarget***, v. 8, n. 12, p. 18618-18619, 2017.

WANG, M.; YUAN, Y.; LIANG, G. "Click Chemistry" for Molecular Imaging. ***Current Molecular Imaging*****,** v. 1, n. 1, p. 87-95, 2012.

WATANABE, Y.; SHIBATA, K.; KIKKAWA, F.; KAJIYAMA, H.; INO, K.; HATTORI, A.; TSUJIMOTO, M.; MIZUTANI, S. Adipocyte-derived leucine aminopeptidase suppresses angiogenesis in human endometrial carcinoma via renin-angiotensin system. ***Clinical Cancer Research*****,** v. 9, n. 17, p. 6497-503, 2003. Available in: <www.periodicos.capes.gov.br>. Accessed on Aug. 6, 2017.

WEGMAN-OSTROSKY, T.; SOTO-REYES, E.; VIDAL-MILLÁN, S.; SÁNCHEZ-CORONA, J. The renin-angiotensin system meets the hallmarks of cancer. ***Journal of the Renin-Angiotensin-Aldosterone System*****,** v. 16, n. 2, p. 227-33, 2015. Available in: <www.periodicos.capes.gov.br>. Accessed on Aug. 5, 2017.

WEISSLEDER, R.; PITTET, M. J. Imaging in the era of molecular oncology. ***Nature*****,** v. 452, n. 7187, p. 580-9, 2008. Available in: <www.periodicos.capes.gov.br>. Accessed on Nov. 2, 2018.

WHO - WORLD HEALTH ORGANIZATION. **Cancer**. http://www.who.int/news-room/fact-sheets/detail/cancer, 2018. Accessed on Nov. 2, 2018.

WORRELL, B. T.; MALIK, J. A.; FOKIN, V. V. Direct evidence of a dinuclear copper intermediate in Cu(I)-catalyzed azide-alkyne cycloadditions. ***Science***, v. 340, n. 6131, p. 457-60, 2013. Available in: <www.periodicos.capes.gov.br>. Accessed on Feb. 8, 2019.

XIE, G.; LIU, Y.; YAO, Q.; ZHENG, R.; ZHANG, L.; LIN, J.; GUO, Z.; DU, S.; REN, C.; YUAN, Q.; YUAN, Y. Hypoxia-induced angiotensin II by the lactate-chymase-dependent mechanism mediates radioresistance of hypoxic tumor cells. ***Scientific Reports*****,** v. 7, p. 42396, 2017. Available in: <www.periodicos.capes.gov.br>. Accessed on Nov. 15, 2017.

YASAR, U.; TYBRING, G.; HIDESTRAND, M.; OSCARSON, M.; INGELMAN-SUNDBERG, M.; DAHL, M. L.; ELIASSON, E. Role of CYP2C9 polymorphism in losartan oxidation. ***Drug Metabolism and Disposition*****,** v. 29, n. 7, p. 1051-6, 2001. Available in: <www.periodicos.capes.gov.br>. Accessed on Nov. 2, 2018.

YU, S. Review of 18F-FDG synthesis and quality control. ***Biomedical Imaging and Intervention Journal*****,** v. 2, n. 4, p. e57, 2006. Available in: <www.periodicos.capes.gov.br>. Accessed on Jul. 24, 2016.

ZHANG, H.; UNAL, H.; GATI, C.; HAN, G. W.; LIU, W.; ZATSEPIN, N. A.; JAMES, D.; WANG, D.; NELSON, G.; WEIERSTALL, U.; SAWAYA, M. R.; XU, Q.; MESSERSCHMIDT, M.; WILLIAMS, G. J.; BOUTET, S.; YEFANOV, O. M.; WHITE, T. A.; WANG, C.; ISHCHENKO, A.; TIRUPULA, K. C.; DESNOYER, R.; COE, J.; CONRAD, C. E.; FROMME, P.; STEVENS, R. C. KATRITCH, V.; KARNIK, S. S.; CHEREZOV, V. Structure of the Angiotensin receptor revealed by serial femtosecond crystallography. ***Cell*****,** v. 161, n. 4, p. 833-44, 2015. Available in: <www.periodicos.capes.gov.br>. Accessed on Aug. 6, 2017.

ZHAO, Y.; CAO, J.; MELAMED, A.; WORLEY, M.; GOCKLEY, A.; JONES, D.; NIA, H. T.; ZHANG, Y.; STYLIANOPOULOS, T.; KUMAR, A. S.; MPEKRIS, F.; DATTA, M.; SUN, Y.; WU, L.; GAO, X.; YEKU, O.; DEL CARMEN, M. G.; SPRIGGS, D. R.; JAIN, R. K.; XU, L. Losartan treatment enhances chemotherapy efficacy and reduces ascites in ovarian cancer models by normalizing the tumor stroma. ***Proceedings of the National Academy of Sciences of the United States of America***, v. 116, n. 6, p. 2210-2219, 2019. Avaliable in: <www.periodicos.capes.gov.br>. Accessed on April 4, 2019.

ZHAO, Y.; CHEN, X.; CAI, L.; YANG, Y.; SUI, G.; FU, S. Angiotensin II/angiotensin II type I receptor (AT1R) signaling promotes MCF-7 breast cancer cells survival via PI3-kinase/Akt pathway. ***Journal of Cellular Physiology*****,** v. 225, n. 1, p. 168-73, 2010. Available in: <www.periodicos.capes.gov.br>. Accessed on Aug. 5, 2017.

ZHAO, Y.; CHEN, X.; CAI, L.; YANG, Y.; SUI, G.; WU, J. Angiotensin II suppresses adriamycin-induced apoptosis through activation of phosphatidylinositol 3-kinase/Akt signaling in human breast cancer cells. ***Acta Biochimica et Biophysica Sinica (Shanghai)*****,** v. 40, n. 4, p. 304-10, 2008. Available in: <www.periodicos.capes.gov.br>. Accessed on Nov. 15, 2017.

ZHAO, Y.; WANG, H.; LI, X.; CAO, M.; LU, H.; MENG, Q.; PANG, H.; LI, H.; NADOLNY, C.; DONG, X.; CAI, L. Ang II-AT1R increases cell migration through PI3K/AKT and NF-κB pathways in breast cancer. ***Journal of Cellular Physiology*****,** v. 229, n. 11, p. 1855-62, 2014. Available in: <www.periodicos.capes.gov.br>. Accessed on Aug. 5, 2017.

ZHANG, C.; ZHANG, Z.; LIN, K.S.; PAN, J.; DUDE, I.; HUNDAL-JABAL, N.; COLPO, N.; BÉNARD, F. Preclinical melanoma imaging with 68Ga-labeled α-melanocyte-stimulating hormone derivatives using PET. ***Theranostics***, v. 7, n. 4, p. 805-8013, 2017. Available in: <www.periodicos.capes.gov.br>. Accessed on Jun 13, 2018.

ZHENG, M.Q.; YIN, D.Z.; QIAO, J.P.; ZHANG, L.; WANG, Y.X. Syntheses and evaluation of fluorinated benzothiazole anilines as potential tracers for β-amyloid plaques in Alzheimer's disease. ***Journal of Fluorine Chemistry***, v. 129, n. 3, p. 210-216, 2008. Available in: <www.periodicos.capes.gov.br>. Accessed on Sep. 2, 2018.

ZHOU, L.; LUO, Y.; SATO, S.; TANABE, E.; KITAYOSHI, M.; FUJIWARA, R.; SASAKI, T.; FUJII, K.; OHMORI, H.; KUNIYASU, H. Role of two types of angiotensin II receptors in colorectal carcinoma progression. ***Pathobiology*****,** v. 81, n. 4, p. 169-75, 2014. Available in: <www.periodicos.capes.gov.br>. Accessed on Aug. 6, 2017.

ZOBER, T. G.; FABUCCI, M. E.; ZHENG, W.; BROWN, P. R.; SECKIN, E.; MATHEWS, W. B.; SANDBERG, K.; SZABO, Z. Chronic ACE inhibitor treatment increases angiotensin type 1 receptor binding in vivo in the dog kidney. ***European Journal of Nuclear Medicine and Molecular Imaging*****,** v. 35, n. 6, p. 1109-16, 2008. Available in: <www.periodicos.capes.gov.br>. Accessed on Nov. 2, 2018.

ZOBER, T. G.; MATHEWS, W. B.; SECKIN, E.; YOO, S. E.; HILTON, J.; XIA, J.; SANDBERG, K.; RAVERT, H. T.; DANNALS, R. F.; SZABO, Z. PET Imaging of the AT1 receptor with [11C]KR31173. ***Nuclear Medicine and Biology*****,** v. 33, n. 1, p. 5-13, 2006. Available in: <www.periodicos.capes.gov.br>. Accessed on Nov. 2, 2018.

9 APPENDIX A – (^{1}H,^{13}C)-HMBC spectra of FEtLos in $CDCl_3$

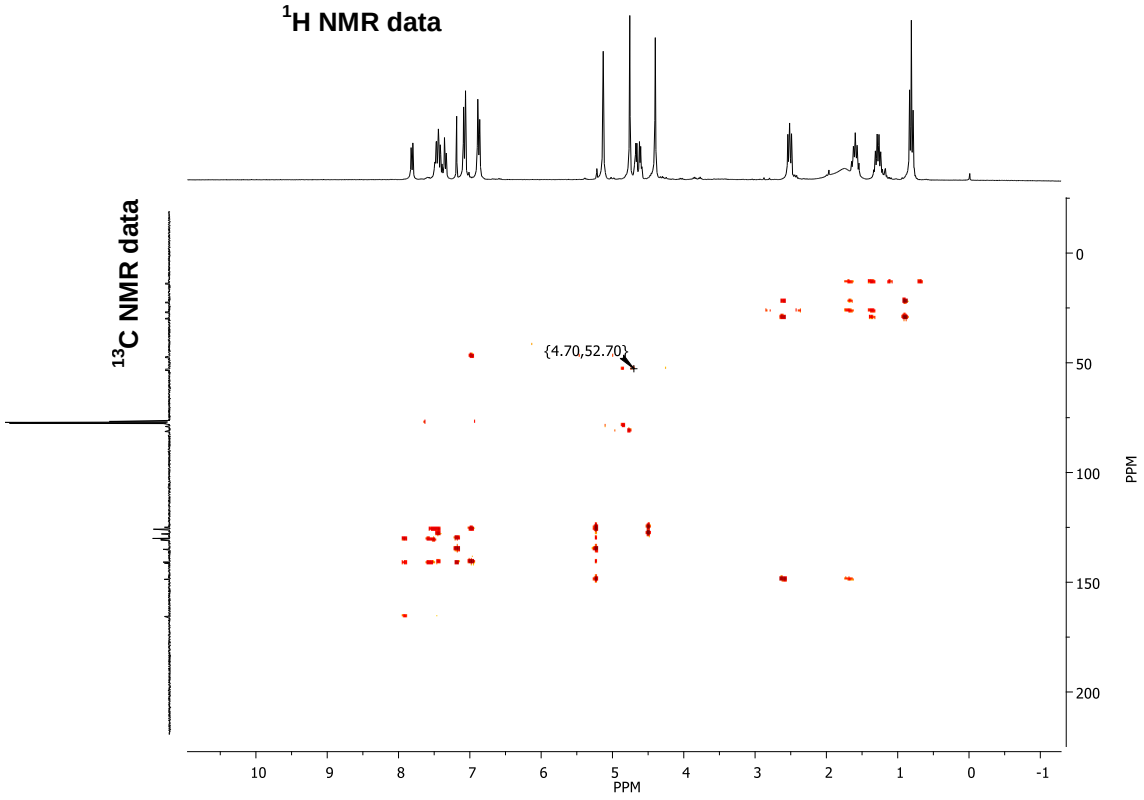

10 APPENDIX B – HRMS (ES$^+$) of FEtLos

Generic Display Report

Faculdade de Ciencias Farmaceuticas de Ribeirao Preto-USP

Analysis Info

Analysis Name	D:\Data\Profa IVONE_QF\LOS_C_POS.d	Acquisition Date	9/24/2014 2:22:51 PM
Method	Tune_Low_Tomaz_Pos_1300u_NOVO.m	Operator	BDAL@DE
Sample Name	LOS_C_POS	Instrument	micrOTOF-Q II
Comment			

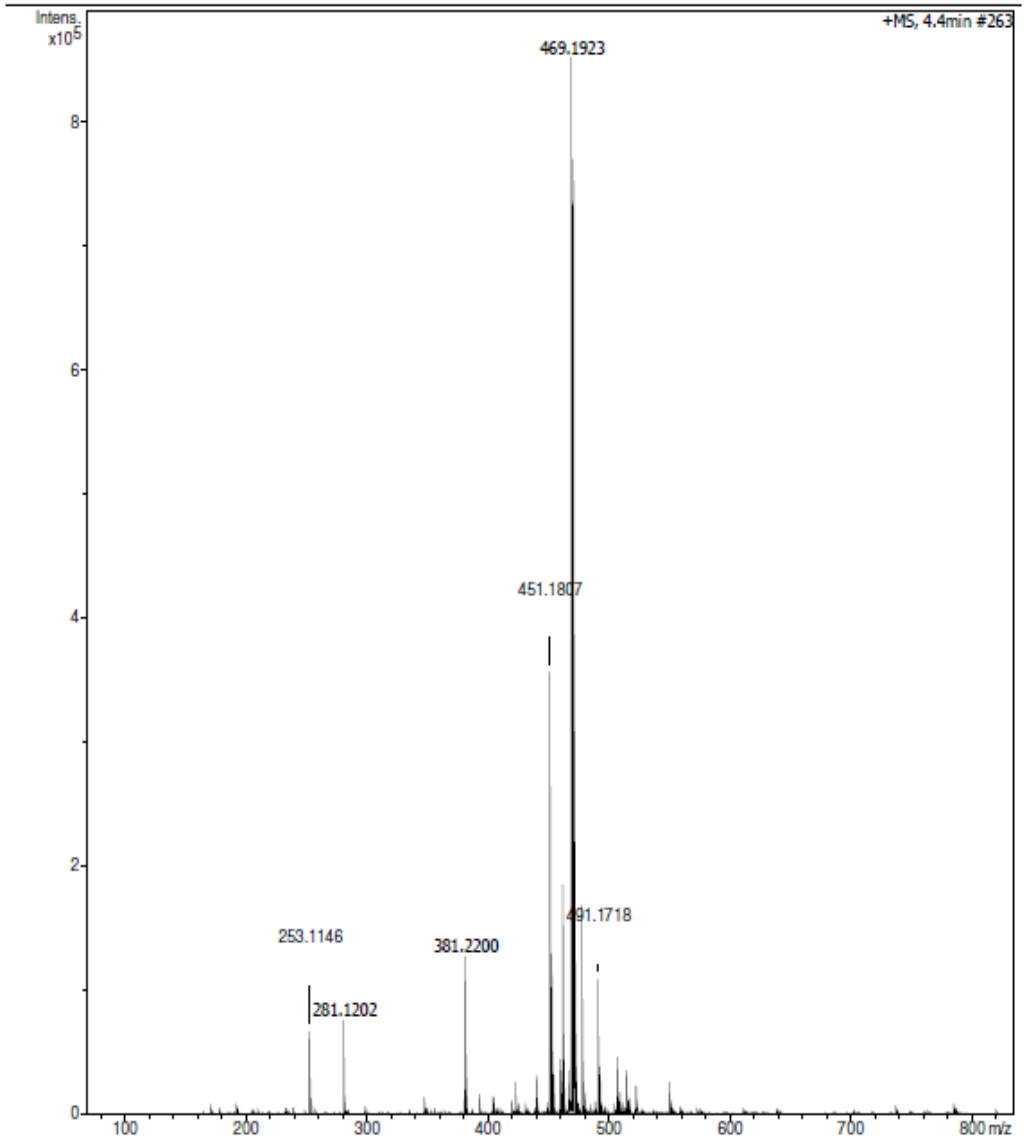

11 APPENDIX C – (^{1}H,^{13}C)-HMBC spectra of AMBF$_3$Los in CD$_3$CN

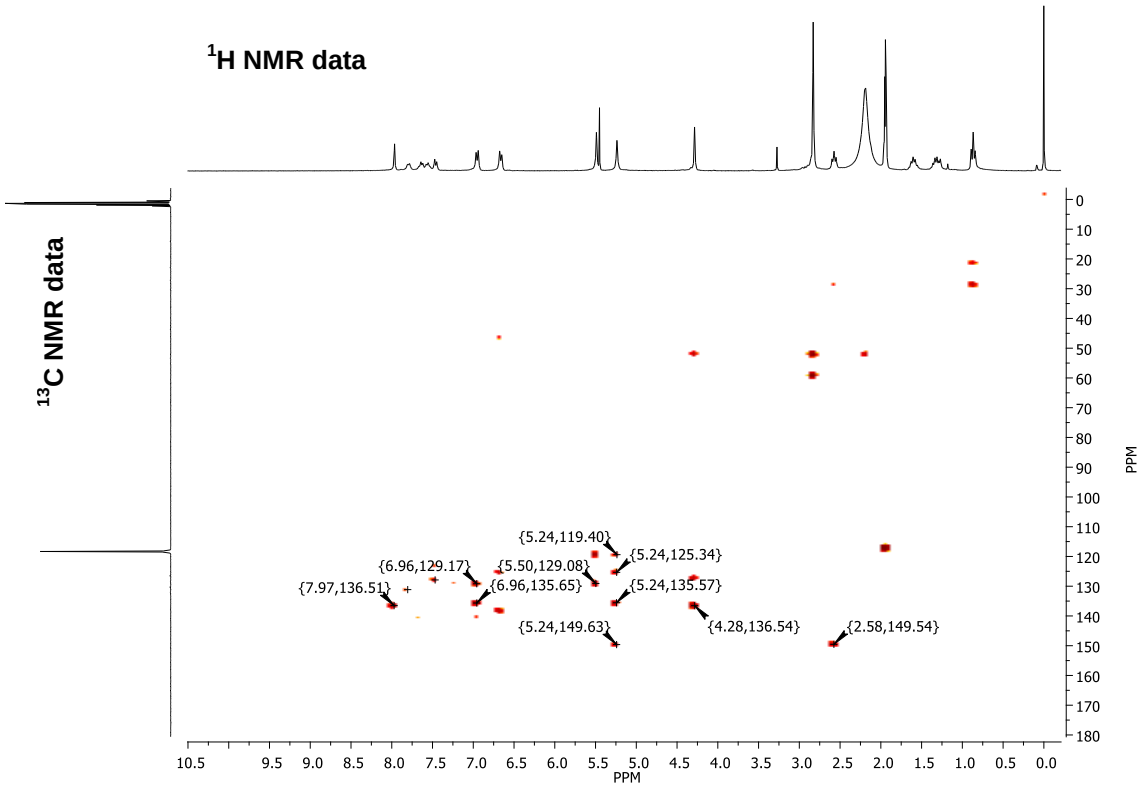

12 APPENDIX D – HRMS (ES^+) of $AMBF_3Los$

Generic Display Report

Analysis Info

Analysis Name	D:\Data\PROF. IVONE\BF 3_Los_POSITIVO.d	Acquisition Date	12/3/2018 8:48:54 AM
Method	Tune_Low_Tomaz_Pos_1300u_Willian 1.m	Operator	TOMAZ
Sample Name	BF 3_Los_POSITIVO	Instrument	micrOTOF-Q
Comment			

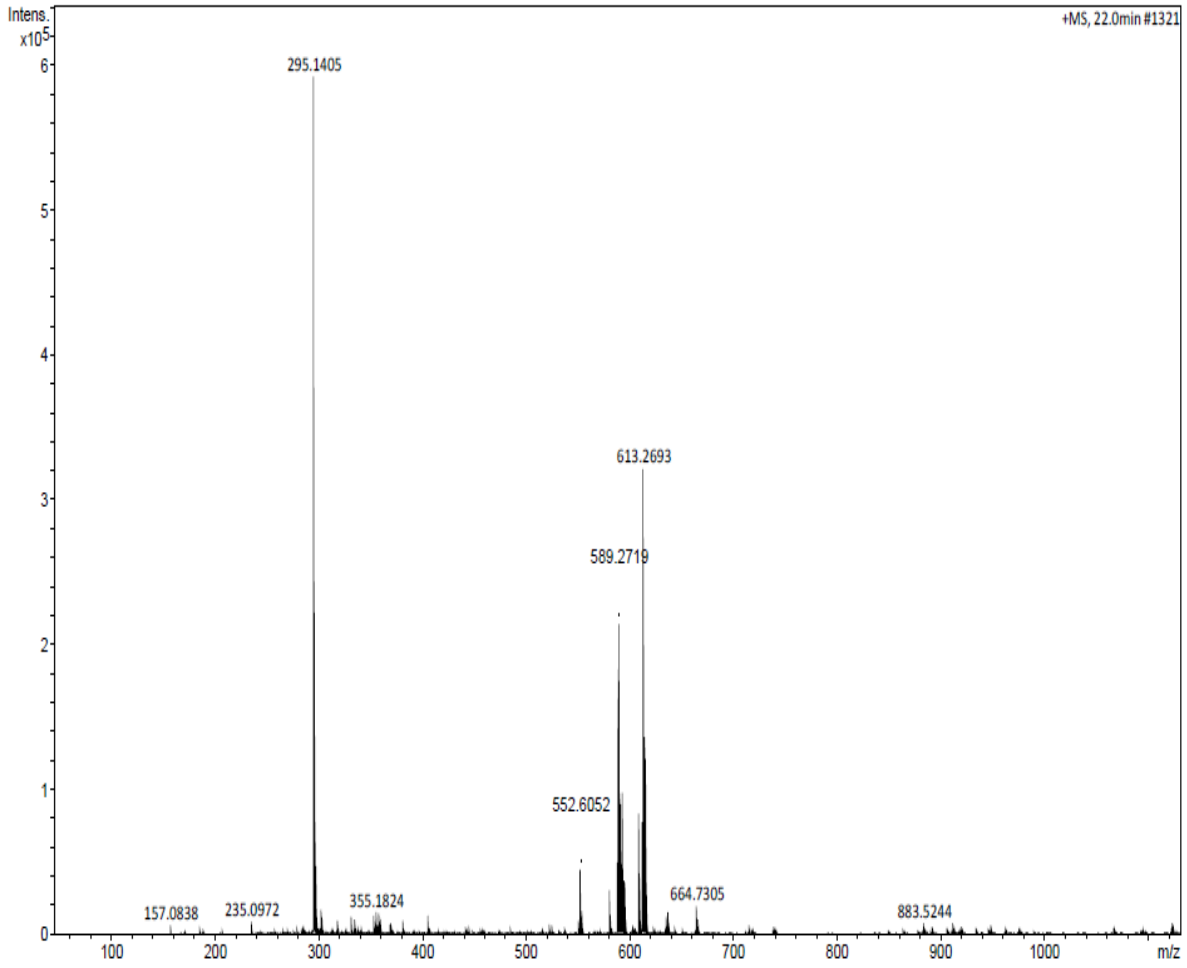

Bruker Compass DataAnalysis 4.3 printed: 12/5/2018 11:02:44 AM by: TOMAZ Page 1 of 1

INSTITUTO DE PESQUISAS ENERGÉTICAS E NUCLEARES
Diretoria de Pesquisa, Desenvolvimento e Ensino
Av. Prof. Lineu Prestes, 2242 – Cidade Universitária CEP: 05508-000
Fone/Fax(0XX11) 3133-8908
SÃO PAULO – São Paulo – Brasil
http://www.ipen.br

O IPEN é uma Autaquia vinculada à Secretaria de Desenvolvimento, associada à Universiade de São Paulo e gerida técnica e administrativamente pela Comissão Nacional de Energia Nuclear, órgão do Ministério da Ciência, Tecnologia e Inovação.